NTNU

Norwegian University of
Science and Technology

Experimental Investigation of Nanoparticle Adsorption and Pore Blockage in Intermediate Wet Berea Sandstone

Tore Sebastian Damgaard

Petroleum Geoscience and Engineering
Submission date: July 2017
Supervisor: Ole Torsæter, IGP

Norwegian University of Science and Technology
Department of Geoscience and Petroleum

Abstract

The global demand of energy is increasing with the growing population, and an increased consumption of available resources is therefore required. Even though there has been more focus on renewable energy over the last years, oil is still the main source of energy worldwide (IEA and OECD, 2016). Thus, continued oil extraction is necessary to satisfy the growing energy demand until it can be replaced by renewable alternatives. Since oil is non-renewable, the production must be maintained by either discovering new hydrocarbon reservoirs, or by improving the oil recovery in the reservoirs. Conventional production methods are seldom capable of producing more than 40 % of the reservoir oil (Schlumberger, 1998d), which means that there is a large potential for enhanced the oil recovery (EOR).

The use of nanotechnology is beneficial in a range of fields, and its applications have also been suggested for the upstream sector of the petroleum industry (Lau et al., 2016). Silica (SiO_2) nanoparticles have proved to be efficient for EOR in a range of laboratory core floods (Hendraningrat et al., 2012; Li et al., 2013; Ogolo et al., 2012; El-Diasty, 2015), and a combination of rock wettability alteration and reduction of interfacial tension (IFT) between oil and water are believed to be the main oil displacement mechanisms. Since silica nanoparticles consist of 99.8% SiO_2 (Evonik, 2015), which is the main mineral in sandstone, they are are also considered environmentally friendly. This solves the legality issues related to field injection of EOR formulations in countries with a strong environmental policy. However, silica nanoparticles are easily destabilized when they are dispersed in saltwater and exposed to high temperature, which are regular sub-surface conditions.

In this master's thesis, I have looked at the EOR potential of nanofluids and the technical feasibility of field implementations. Laboratory experiments have been conducted to investigate the propagation of silica nanoparticles at various conditions, as this is important for the feasibility of field implementations. The nanoparticles were injected in *intermediate wet* Berea sandstone cores, since these were believed to represent many of the

world's oil saturated sandstone reservoirs (Cosentino, 2001). Nanoparticle retention during transportation through the cores was studied, and a simple stabilizer was demonstrated to counter spontaneous nanoparticle aggregation at reservoir conditions. The results from the laboratory experiments showed that the formation damage from regular nanofluid injection is severe and almost makes the rocks impermeable. The formation damage was reduced when stabilizer was added to the nanofluids, but the improvement was too small for a field implementation of the EOR method. In order to study nanoparticle propagation at reservoir conditions, the flow rate was lowered and the temperature was elevated. This resulted in increased nanoparticle retention, and complete pore blockage after only 2 PVs of injection. This emphasizes the need for methods to stabilize nanosilica suspensions at reservoir conditions.

Sammendrag

Det globale energibehovet øker i takt med befolkningsvekst, noe som krever økt bruk av tilgjengelige energiressurser. Selv om det i de senere årene har vært mer fokus på fornybar energi, så er olje fortsatt hovedkilden til energi på verdensbasis (IEA and OECD, 2016). Økt oljeproduksjon er derfor nødvendig inntil det finnes fornybare alternativer som kan dekke det økende energibehovet. Oljeproduksjonen kan opprettholdes enten ved å utforske nye petroleumsreservoarer, eller ved å øke utvinningsgraden fra hvert enkelt reservoar. De vanlige produksjonsmetodene som blir brukt i dag klarer sjeldent å produsere mer enn 40 % av oljen i reservoaret (Schlumberger, 1998a), og det er derfor et stort potensiale for økt oljeutvinning.

Bruken av nanoteknologi har vist seg å være fordelaktig i en rekke bransjer, og ifølge Lau et al. (2016) kan nanoteknologi også bli brukt i oppstrømssektoren i petroleumsbransjen. Nanopartikler av silikat (SiO_2) har hatt en bevist effekt på oljeutvinning i en rekke flømmingsforsøk med kjerneprøver (Hendraningrat et al., 2012; Li et al., 2013; Ogolo et al., 2012; El-Diasty, 2015), og en kombinasjon av fuktendring i kjerneprøven og senkning av overflatespenningen mellom olje og vann er trolig mekanismene som står bak den økte produksjonen. Silikat-nanopartikler er ansett for å være miljøvennlige ettersom de består av 99.8 % SiO_2 (Evonik, 2015), som rent kjemisk er det samme som kvarts. Dette løser de miljørelaterte problemene og forbudene mot reservoar-injeksjon i en rekke land med fokus på miljøpolitikk. Dessverre har silikat-nanopartiklene en tendens til å være ustabile i saltvann, og når de er utsatt for typiske reservoarbetingelser som høy temperatur.

I denne masteroppgaven har jeg studert nanofluiders potensiale til å øke oljeutvinningen og hvorvidt feltinjeksjoner er gjennomførbare. Laboratorieeksperimenter har blitt utført for å undersøke transporten av silkat-nanopartikler i ulike situasjoner. Nanopartiklene ble injisert i *mellomfuktede* kjerneprøver av Berea sandstein, ettersom disse trolig representerer mange av verdens oljemettede sandsteinsreservoarer (Cosentino, 2001). Tilbakeholdningen av nanopartikler i sandsteinsprøvene under transport ble undersøkt, og en enkel stabilisator ble demonstrert for å redusere aggregeringen av nanopartikler under

reservoarbetingeleser. Resultatene viste at injisering av ubehandlet nanofluid fører til stor formasjonsskade som nesten gjør kjerneprøvene impermeable. Formasjonsskaden ble redusert når stabilisatoren ble introdusert, men forbedringen var for liten til at en feltinjeksjon kan gjennomføres. For å undersøke transporten av nanopartikler under reservoarbetingelser ble flømmingsraten redusert og omgivelsestemperaturen økt. Dette resulterte i økt formasjonsskade og total poreblokkering etter kun 2 porevolumer med injeksjon. Dette understreker behovet for å kunne stabilisere nanofluider av silikat under reservoarbetingelser.

Acknowledgements

This Master's thesis was carried out in collaboration with the Institute of Chemical & Engineering Sciences (ICES) under the Agency for Science, Technology and Research (A*STAR). I would like to thank my supervisor at the Norwegian University of Science and Technology, Professor Ole Torsæter, for the guidance throughout the process and his initiative to let me work with ICES for the experimental part of the thesis. My deepest appreciation goes to my supervisor at ICES, Dr. Ludger Paul Stubbs, for his constructive feedback and for making the collaboration possible.

Dr. Nanji Hadia and Dr. Shidong Li contributed with theoretical insight, experience and fruitful suggestions throughout the experimental process. A great thanks goes to them for their technical assistance and valuable discussions. I would also like to thank the engineers, Don Lim Chen Chuan and Andrew Ng Qi Hua, for their patience and technical support in times of stress and when I felt like giving up. The experiments would not have been possible without their effect and expertise.

This thesis was made independently and in accordance with the rules of the Examination Regulations made by the Norwegian University of Science and Technology.

Table of Contents

List of Tables

List of Figures

Abbreviations

ASG	=	Alkaline-Surfactant-Gas
CDG	=	Colloidal Dispersion Gel
CSS	=	Cyclic Steam Stimulation
CSC	=	Critical Salt Concentration
DC	=	Dimensionless Concentration
DLS	=	Dynamic Light Scattering
EDL	=	Electrical Double Layer
E&P	=	Exploration and Production
EOR	=	Enhanced Oil Recovery
IFT	=	Interfacial Tension
MMP	=	Minimum Miscibility Pressure
MNP	=	Magnetic Nanoparticle
NSP	=	Nanostructured particles
NP	=	Nanoparticle
OOIP	=	Original Oil in Place
PSD	=	Particle Size Distribution
PV	=	Pore Volume
SAG	=	Surfactant-Alternating-Gas
SAGD	=	Steam Assisted Gravity Drainage
SEM	=	Scanning Electron Microscope
SSW	=	Synthetic Seawater
TDS	=	Total Dissolved Solids
ULP	=	Ultrasonic Liquid Processor
WAG	=	Water-Alternating-Gas
WI	=	Wettability Index

1 Introduction

Nanotechnology is a science regarding materials in the size range of 1 to 100 nanometers, where 1 nanometer is one billionth (10^{-9}) of a meter. Thus *nanomaterials* are bigger than simple molecules, but a lot smaller than e.g. blood cells. The Royal Society & The Royal Academy of Engineering (2004) defines nanotechnology as "the design, characterization, production, and application of structures, devices, and systems by controlling shape and size on the nano scale". This control distinguishes nanotechnology from chemistry, as it allows the manufacturing of small size materials that are chemically similar, but behaviorally different from the larger size materials.

Nanomaterials can be produced from a range of polymers, ceramics and metals, and may come in morphologies such as spheres, flakes, platelets, rods and tubes (Pitkethly, 2004). The definition of a nanomaterial requires at least one of its dimensions, either internal or external, to be within the nanoscale (SCCP, 2007). Thus, nanomaterials are classified into nanostructures by the number of dimensions **not** confined to the nanoscale. The zero-dimensional (0-D) structures represent simple nanoparticles and clusters of various sphericities, while the 1-D and 2-D structures include nanosized tubes/rods and flakes/platelets respectively. 3-D structures are not nanomaterials since non of the dimensions are confined to the nanoscale. Figure 1.1 illustrates the various morphologies of nanostructures and their corresponding classes.

Dimensionality and size both affect the properties of nanomaterials (Kestell and DeLorey, 2010), and make their properties different from their bulk counterparts. Horikoshi and Serpone (2013) list some of the common properties which are seen in nanomaterials:

- Mechanical strength: Nanomaterials are mechanically stronger than their bulk counterparts. Thus, the mechanical strength of a material can be enhanced by introducing nanoparticles in the making.

- Specific magnetization: The attractive forces of magnetic metals increase with a decreasing metallic particle size, making it possible to control the magnetization of some materials.
- Thermal function: Due to the small size, nanomaterials and their bulk counterparts have different thermal functions. The melting point of nanoparticles is low, making them suitable for electrical wiring.
- Electrical conductivity: Nanomaterials can be used to construct superconductors, as the small size will limit the increasing resistance from a rising transition temperature.
- Optical property: Materials of different size may express different colors, due to different light absorbency properties.

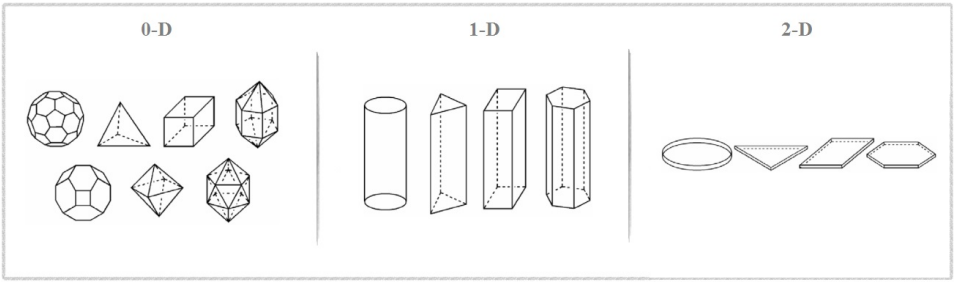

Figure 1.1: Classification of nanoparticles (adapted from Kestell and DeLorey, 2010)

Favorable properties of nanomaterials have made them applicable in many fields and industries such as the electronic industry, the medical industry (Horikoshi and Serpone, 2013) and lately; the petroleum industry (Krishnamoorti, 2006).

1.1 Nanotechnology in the Petroleum Industry

There is a large potential for nanomaterials in the upstream (E&P) sector, in areas such as exploration, drilling/completion and EOR. Involvement of nanotechnology in oilfield projects could mean real-time mapping of reservoirs and the possibility of monitoring depletion and displacement fronts (Friedheim et al., 2012). Due to regulations and short history of nanotechnology in petroleum engineering, most of the technical applications are still at a research state and need further development before they can outperform commercial methods. However, some single-well applications of nanotechnologies are already in

use for completion of horizontal wells and for the enhancement of drilling fluids (Jacobs, 2017).

1.1.1 Drilling and Completion

Bentonite is a clay which has commonly been used in drilling mud for decades in order to control mud filtration and viscosity (Schlumberger, 1998a). As some components of the clay are smaller than 100 nanometers (Jessen and Mungan, 1959), a drilling mud containing bentonite is by definiton nano-based since nano-sized particles will be liberated. Thus, drilling with nanofluids is not a new, but the design and control of modern nanotechnology makes the development of particles specially made for the improvement of drilling fluids possible. Introduction of such particles can provide effective bit cooling (Kong and Ohadi, 2010), wellbore stability, fluid loss control and may overcome some of the challenges met during oil drilling (Friedheim et al., 2012).

Traditional water-based or oil-based mud may produce a poorly dispersed, thick and porous mud cake. Since a poor quality mud cake is unable to prevent the invasion of colloids and cutting debris into the borehole wall, severe formation damage may occur due to blockage of pore throats. Designing drilling fluids which do not damage the formation should be emphasized, as the aim of oil drilling is to maximize the the production of the reservoir's hydrocarbons. A solution to these challenges is to introduce nanoparticles to the drilling fluids. The nano-based drilling fluids can produce thin mud cakes which are tightly packed and well dispersed (Amanullah et al., 2011).

Low wellbore strength is a problematic part of oil drilling as it can lead to mud loss and make the whole drilling process more inconvenient. There have been several applications of well stability enhancement in high permeable formations such as sandstone, but the limited field success of shale stability enhancement calls for a new approach. Contreras et al. (2014) conducted laboratory experiments which concluded that nanoparticles in combination with graphite can be used to enhance the stability of shale cores, despite a very low permeability. The firm *nFluids* are developing nano additives which can be used in all types of drilling fluids. Results from several pilot well tests conducted by the firm, confirmes that the additive is capable of increasing the wellbore strength by 60%, reducing fluid losses by 90% and drilling friction by 50% (Jacobs et al., 2016).

1.1.2 Reservoir Characterization and Imaging

Traditional methods of reservoir characterization rely on the drilling of exploration wells in fields with promising lithology, followed by petrophysical measurements during logging in the well bore. Many of these measurements could benefit from improvement of accuracy as they are either unreliable in high temperature and pressure, or unable to penetrate deep into the formation while maintaining a high resolution. In addition, the high cost of well drilling in the North Sea often requires field development decisions to be made based on the information of just a few exploration/appraisal wells. The data retrieved is interpolate to estimate reservoir heterogeneity, but the simplification often leads to poor predictions of fluid flow (Damsleth and Holden, 1994). Such reservoir uncertainties also makes ideal well positioning difficult, which leads to poor sweep in reservoirs with few wells.

Magnetic nanoparticles (MNPs) propose a solution by making fluid front monitoring possible during the displacement process. By using MNPs in a pilot test, additional wells can later be drilled in zones where water does not enter. Magnetic nanoparticles can also improve reservoir imaging near the well, as they are not impaired by the steel casing in the wellbore like conventional tools (Wilt et al., 1996). EM tomography allows estimation of rock porosity, permeability and fluid content, by measuring the electrical conductivity of the reservoir rock (Torres-Verdin and Tarek, 1993). This method can characterize the formation tens of meters from the borehole, but the propagation of the EM waves will unfortunately be impaired by the presence of steel casings in the wellbore (Wilt et al., 1996). Since magnetic nanoparticles are detectable at low frequencies, these provide a solution for reservoir imaging near the well. Furthermore, magnetic nanoparticles alter the magnetic permeability along the flow path which make them favorable for real-time fluid front localization (Rahmani et al., 2015).

Nanosensors are currently being developed with the aim to solve some of these problems. Saudi Aramco have already developed nanoparticles called *A-dots*, capable of travelling through reservoirs of high temperature and salinity. A pilot test in the Ghawar field showed that 86% of the injected A-dots were recovered, after the well had been shut-in for 2 days (Kosynkin and Kanj, 2011). This proves that nanoparticles can be designed to have a long lasting stability, with limited particle precipitation, agglomeration and adsorption onto the rock. With further development, the A-dots can probably be used for fluid/reservoir typing and EOR mechanisms in the future.

1.1.3 EOR applications

Oil is conventionally produced from petroleum reservoirs by *primary* and *secondary* recovery mechanisms. Primary recovery is achieved through gravity drainage, gasdrive and waterdrive, which are all natural production mechanisms in the reservoir. Secondary recovery is achieved by injecting water or gas into the reservoir, which will lead to increased reservoir pressure and displacement of oil (Schlumberger, 1998c; Schlumberger, 1998d). The total recovery achieved after conventional production will seldom exceed 40%, which means that there is a huge potential for improvement in terms of *enhanced oil recovery* (EOR). It is expected that the demand for EOR will increase in the future, as it will be the the only way to maintain high production when new hydrocarbon reservoirs are no longer discovered.

Nanoparticles can be used for EOR when injected into the formation in a liquid suspension (e.g. with brine, ethanol or distilled water). Ogolo et al. (2012) have investigated various metallic nanoparticles as potential candidates of EOR, and found that aluminum oxide (Al_2O_3), nickel oxide (Ni_2O_3) and silicon oxide (SiO_2) were able to increase oil recovery when injected in a brine suspension. Nanoparticles are more flexible than traditional chemical EOR methods, as they can be designed to withstand harsh reservoir conditions and thereby propagate far into the reservoir. Some nanoparticles have the tendency to alter the wettability of reservoir rocks towards a more water-wet state, which will increase oil production through the release of oil droplets from pore's walls. Other nanoparticles may create a more favorable mobility ratio between the oil and the injected liquid, by reducing or increasing the oil and injected liquid viscosity respectively. Enhanced mobility ratio results in a more piston-like displacement which efficiently pushes oil out of the pores, and better propagation in heterogeneous reservoirs.

Suspensions of SiO_2 nanoparticles are regarded as environmentally friendly (Agrawal et al., 2016), which gives a promising solution for EOR in countries where the environmental policy rejects reservoir injections of any hazardous chemicals (e.g. surfactants and polymers). However, commercial use of nanoparticles in EOR is currently not economically feasible due to the high particle production price in combination with low oil prices. The high production costs can be overcome with a larger and standardized nanoparticle production, which is believed to happen once oil companies dare to apply the technology and when the technology matures to a certain level (Bennetzen and Mogensen, 2014).

2 Reservoir Properties

Petroleum reservoirs are rock formations which contain hydrocarbon fluids. The interaction between the formation and the fluids is complex, and requires fundamental knowledge of reservoir properties to understand the dynamics within the reservoir during oil and gas production. The relevant properties can be determined in a laboratory by performing experiments on reservoir core samples.

2.1 Porosity

Porosity determines a reservoir's capacity to store fluids. It is defined as the ratio of a rock's porous volume to the bulk volume (the rock volume enclosed by its surface), and is seen in equation 2.1. The porosity of a rock consisting of uniform grains is independent of grain size, but will be affected by grain sphericity and packing. Rock porosity has a maximum value of 48% when spherical grains are packed cubically, but it decreases to 26% with rhombohedral packing, which is more representative for a reservoir.

$$\phi = \frac{PV}{V_{bulk}} = \frac{V_{bulk} - V_{grain}}{V_{bulk}} \tag{2.1}$$

The absolute porosity of a rock is different from the effective porosity, as the effective porosity only considers the *interconnected* pores within the rock. Only the interconnected pores in porous media contain fluids which can be transmitted and produced. There is usually not a large difference between the absolute and effective porosity in granular rocks, but variations may occur in shales, highly cemented rocks and rocks prone to dissolution (e.g. limestone) (Torsæter and Abtahi, 2003).

Nomenclature of equation 2.1:
ϕ: porosity, PV: pore volume, V_{bulk}: bulk volume, V_{grain}: grain volume.

2.2 Permeability

Permeability is a property which determines the ability of porous media to transmit fluids. The property was discovered by Henry Darcy in 1856, when he found that the velocity of water through an unconsolidated sand pack was always proportional to the differential pressure between the inlet and outlet of the sand pack (Dake, 1998). This finding resulted in Darcy's law, seen in equation 2.2 for horizontal flow, which can be used to measure the absolute permeability of a single-phase saturated rock.

$$\frac{Q}{A} = \overline{u} = \frac{k}{\mu}\frac{\Delta P}{L} \tag{2.2}$$

Some rock formations, such as sandstones, are often high permeable due to mostly large pores which are well-connected. Formations such as shales and siltstones have heterogeneous smaller pores with less interconnection, which makes these rocks low permeable or even *impermeable* (Schlumberger, 1998b). Unlike small core sample, the permeability of real reservoirs is often heterogeneous and can have a pronounced variation with respect to position (Torsæter and Abtahi, 2003). Thus, a modification to equation 2.2 which considers three-dimensional variations in pressure response is necessary for a more accurate reservoir model. The modification is seen in equation 2.3, where the differential pressure has been substituted by a pressure gradient.

$$\overline{u} = \frac{\overline{\overline{k}}}{\mu}\nabla P(x, y, z) \tag{2.3}$$

Nomenclature of equation 2.2 and 2.3:
Q: flow rate, A: cross-sectional area, $\overline{u}$: superficial velocity, $\overline{\overline{k}}$: permeability tensor, μ: fluid viscosity, ΔP: differential pressure, L: Length of rock/core sample, ∇P: pressure gradient.

2.3 Wettability

Wettability is a rock property which defines a fluid's ability to spread across the rock surface, in presence of another fluid (Torsæter and Abtahi, 2003). Petroleum reservoirs can be wetted by the oil or the water, and are therefore defined as either oil-wet or water-wet respectively. Petroleum reservoirs may also be intermediate wet, i.e. the rock surface is not strongly wetted by neither oil or water. In a water-wet reservoir most of the oil will reside in the larger pores, while the water is found in the smaller pores. Thus, the oil will be more mobile during production, as opposed to an oil-wet system where the oil is trapped in the smaller pores. As a result, the final oil recovery from water-wet reservoirs will usually be higher than for intermediate wet or oil-wet reservoirs (Donaldson and Alam, 2008).

The wettability of a 3-phase system, consisting of rock, water and oil, can be determined by measuring the contact angle between the rock surface and the contacting water droplet in a system that is submerged in oil. An illustration of a 3-phase system with a measurable contact angle is seen in Figure 2.1. If the droplet expands over the core surface, the contact angle between the rock and the droplet will be $\theta = 0^\circ$ and the system is considered water-wet. If the droplet becomes spherical in contact with the rock surface, $\theta = 180^\circ$ and the system is oil-wet. If $\theta = 90^\circ$ the system is neutral-wet. A rock's wettability can also be determined by the Amott test, which measures a core sample's capability of producing oil and water through spontaneous and forced imbibition of water and oil respectively. The production data is inserted in equation 2.4, which calculates the *wettability-index (WI)*. The wettability-index ranges from -1<WI<1, where -1 corresponds to an oil-wet core and 1 to a water-wet core (Torsæter and Abtahi, 2003). If the oil production when surrounded by water is higher than the water production when surrounded by oil the core sample is considered water-wet, while the opposite applies for an oil-wet core. If the produced volumes of both oil and water are very low, the core sample (rock) will be close to neutral-wet since the wettability-index will be close to WI=0.

$$WI = \frac{V_{o1}}{V_{o1} + V_{o2}} - \frac{V_{w1}}{V_{w1} - V_{w2}} \tag{2.4}$$

Nomenclature of equation 2.4:
WI: wettability-index, V_{o1}: Oil produced during water imbibition, V_{o2}: Oil produced during waterflooding, V_{w1}: Water produced during oil "imbibition", V_{w2}: Water produced during oil flooding.

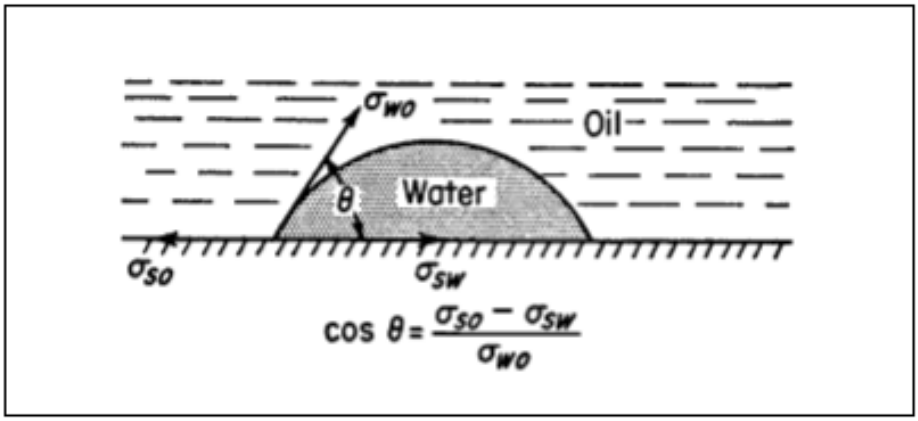

Figure 2.1: Contact angle between a droplet and rock surface (Torsæter and Abtahi, 2003)

2.4 Saturation

Evaluation of fluid saturation is an important aspect of reservoir engineering, as it can be used to estimate oil recovery and predict flow behavior in multi-phase flow. The fluid saturation of a rock is defined as the relative amount of pore volume which is occupied by the given fluid. The relevant fluids in a petroleum reservoir are oil, gas and water, and the fluid saturation of component *i* within the reservoir may be expressed as in equation 2.5

$$S_{i=o,g,w} = \frac{V_i}{V_p} \tag{2.5}$$

As the only fluids present within the pores of a reservoir are oil, gas and water, the formation is completely saturated by a combination of these fluids. This conclusion leads to the saturation balance which is seen in equation 2.6 (Torsæter and Abtahi, 2003).

$$S_{fluid} = S_o + S_g + S_w = 1 \tag{2.6}$$

Nomenclature of equation 2.5 and 2.6:
S_i: Saturation of fluid *i*, V_i: occupied pore volume of fluid *i*, V_p: pore volume, S_fluid: total fluid saturation.

In a petroleum reservoir where gas, oil and water are all present, the fluids will be distributed vertically according to their specific gravity as seen in Figure 2.2. The fluid in

the upper section of the reservoir is highly gas saturated, with a saturation of $S_g = 100\%$ above the gas-oil-contact (GOC). Below the GOC, the amount of gas dissolved in the oil decreases with an increasing depth. The oil is also partially water saturated in the oil section, and the water saturation increases with depth until it reaches 100% below the *free water level* (FWL).

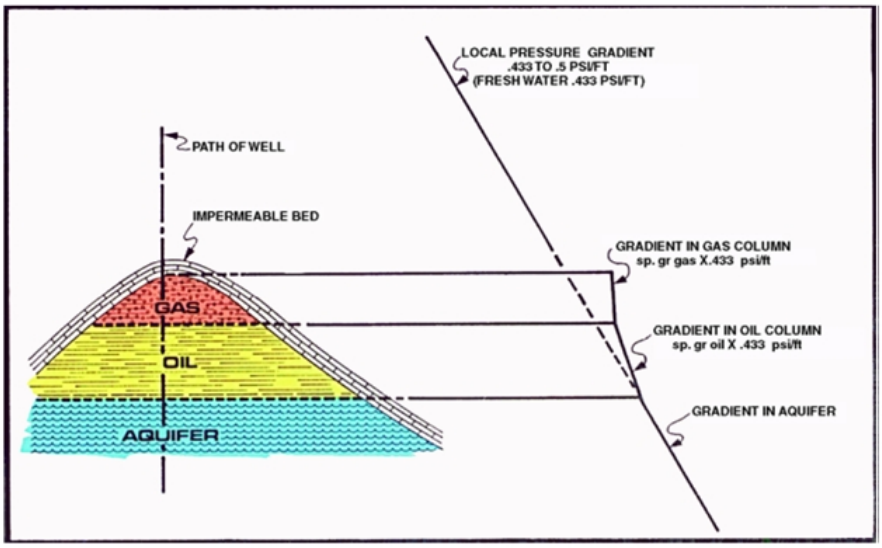

Figure 2.2: Fluid distribution and pressure gradients in petroleum reservoirs (Meehan, 2011)

2.5 Viscosity

Viscosity is a property which associates with the ability of a fluid to flow freely. The idea of a proportional relationship between viscosity and flow time has been accepted in the petroleum industry, as the experimental results can be reproduced for highly viscous liquids such as oil. The fundamentals of viscosity shows that it will determine the rate of deformation for a fluid which is subjected to stress. For *newtonian* fluids such as water, gas and oil, the relationship between stress and deformation rate is linear and can be expressed as in equation 2.7. If the functional relationship in equation 2.7 is not linear, the fluid is defined as non-newtonian. A shear-thinning or shear-thickening behavior is seen for such fluids, depending on whether the *slope* for the rate of deformation increases or decreases with an increasing shear stress (White, 1991). Viscous behaviors for various fluids are

seen in Figure 2.3.

$$\tau = \mu \frac{du_x(y)}{dy} \tag{2.7}$$

Nomenclature of equation 2.7:
τ: shear rate, μ: fluid viscosity, $\frac{du_x(y)}{dy}$: rate of deformation, u: fluid velocity.

Shear-thinning or pseudo plastic fluids appear to be newtonian at low shear rates, but show a plastic behavior when a critical value of shear rate is reached. For polymeric fluid solutions, the shear-thinning behavior will be affected by the colloidal concentration of the suspension and the solution's characteristics. **Shear-thickening** or dilatant fluids are not as well-understood, as they show an increasing resistance to deformation as the shear rate is increased. Moderate to high concentrated solutions of surfactants, polymers, proteins and protoplasm may exhibit this viscosity behavior for concetrations below 1 wt% (Savins, 1969).

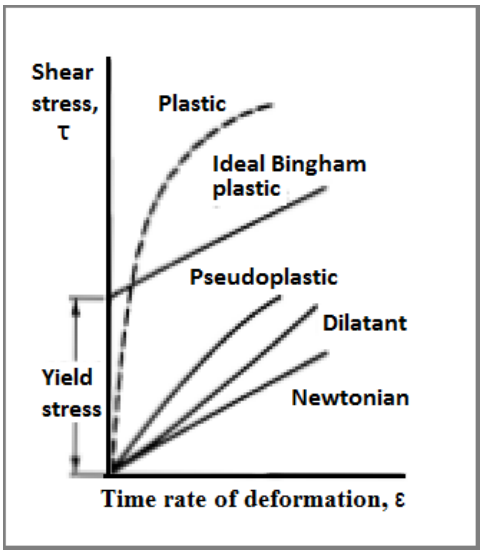

Figure 2.3: Viscous behavior of various fluids (adapted from White, 1991)

3 Enhanced Oil Recovery

Many techniques for *enhanced oil recovery* (EOR) have been investigated over the years, with some proving to have great potential before and after conventional waterflooding. Alkaline-Surfactant-Gas (ASG) flooding has been one of the most efficient chemical EOR methods, with a reported tertiary oil recovery of 96% in sand packs (Li et al., 2008). Foam, which is made by alternating surfactant and gas, improves the conformance control of the driving fluid drastically in heterogeneous reservoirs, indicating that ASG flooding could be an efficient recovery method in oil fields (Srivastava et al., 2009). However, the high costs of surfactants often require high oil prices in order to justify the EOR projects. Thus cheaper approaches which yield substantial recovery at field scale are needed in order to increase and maintain future production.

The various EOR approaches are normally be classified into four groups: chemical, thermal, miscible and microbial methods. The chemical methods include polymer, surfactant/micellar and alkaline injection, which respectively affect the interaction between the injected fluid and oil by enhancing fluid mobility ratio, reducing interfacial tension (IFT) and indirectly reducing IFT through in-situ soap generation. If polymer, surfactant and alkaline are all injected in combination, a synergic effect on oil recovery is seen (Srivastava et al., 2009).

The thermal methods include steam injection, steam assisted gravity drainage (SAGD) and in-situ combustion. Injection of steam will lower the oil viscosity, and has proved to be effective if it is injected in cycles, known as Cyclic Steam Stimulation (CSS). In-situ combustion is another traditional EOR method, and it is conducted by igniting the reservoir down-hole. 5-10% of the oil is burned off to provide heat to rock and fluids, which will increase reservoir pressure and improve oil quality by generating a light oil bank through condensation of light components from the newly vaporized oil (Turta, 2013). SAGD is an efficient recovery method for heavy oils (such as bitumen), which utilizes two parallel

wells for continuous steam injection and collection of the mobilized oil respectively. The reservoir and the well used for steam injection is typically located above the collection well, so that gravity can assist the drainage of mobilized oil towards the collection well (Shen, 2013).

Miscible flooding is conducted by injecting hydrocarbon or non-hydrocarbon gases into oil reservoirs which are left with a residual oil saturation from waterflooding. The injected gases may be mixtures of hydrocarbons from methane to propane ($C_1 - C_3$), nitrogen (N_2) or carbon dioxide (CO_2). The residual oil is primarily recovered by an increased mass transfer between the flowing gas and oil phase, due to increased miscibility. Since gas dissolution in oil will also reduce the oil viscosity, the enhanced mobility control is regarded as an additional recovery mechanism (Johns and Dindoruk, 2013). The super-critical pressure and temperature of CO_2, respectively $P_{crit} = 75\ atm$ and $T_{crit} = 31^oC$, makes it applicable for EOR purposes since most reservoirs have pressures and temperatures that exceed these values. When these are surpassed, the CO_2-gas becomes denser and more viscous which will enhance displacement and limit viscous fingering (see Figure 3.2) (Lee and Kam, 2013).

In addition to the traditional EOR methods there are novel methods such as smart water flooding and nanofluid flooding. Smart water is water with an adjusted or optimized ion composition which can change the equilibrium between the crude oil, brine and rock, and alter rock wettability. A wettability alteration towards a more water-wet state will influence capillary pressure and relative permeability positively, which leads to an increase of oil recovery (Austad, 2013). As stated in the introduction, some nanoparticles are able to alter rock wettability as well as reducing IFT and increasing the dispersant's viscosity. They are cheap alternatives to traditional EOR agents such as surfactants, and are flexible in terms of modification and customization for a specific task.

3.1 Recovery Efficiency

Incremental oil recovery can prolong oil production and will increase the total oil recovery from petroleum reservoirs. As seen in Figure 3.1, incremental oil recovery refers to the additionally recovered oil from a project where an EOR process is applied, compared to a more standard project where it is not applied. For tertiary recovery processes, incremental oil recovery is often represented as the ratio of additional production and original oil in

place (OOIP), but may sometimes be represented as a produced fraction of the residual oil after waterflooding (Sheng, 2011).

Lake (1989) defines the recovery efficiency of an EOR process as the product of displacement efficiency (E_D) and volumetric sweep efficiency (E_V), as expressed in equation 3.1. Displacement efficiency measures the fractional amount of oil displaced after being in contact with the displacing agent, i.e. how efficiently the oil is displaced by the displacing fluid. This factor regards one-dimensional recovery in the direction of flow, and is the most important recovery factor in core flooding experiments on homogeneous and isotropic core samples.

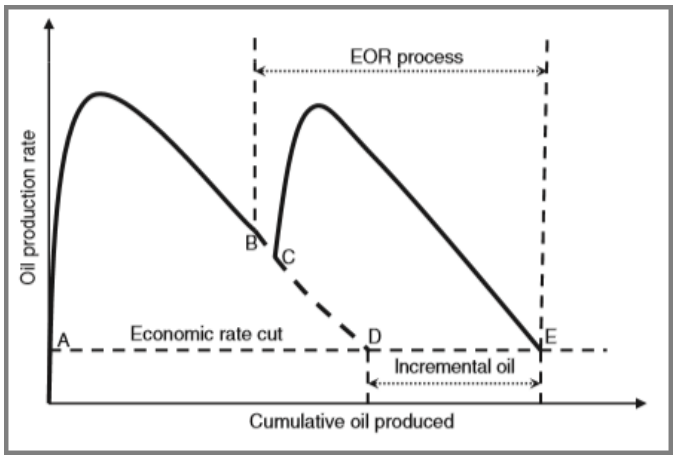

Figure 3.1: Incremental oil recovery from an EOR process (Sheng, 2011)

$$E_R = E_D \cdot E_V = \frac{\text{Amount of oil displaced}}{\text{Volumes of original oil in place}} \tag{3.1}$$

The volumetric sweep efficiency may be expressed as a product of vertical (E_I) and areal (E_A) sweep efficiency, as shown in equation 3.2. The vertical and areal sweep are both defined as planar flows, with on depending on the other due to one common dimension. The sweep efficiency will have a significant effect on the recovery efficiency in field scale reservoirs, as the contact between the displacing agent and the oil in the reservoir will be lower than in a one-dimensional case (Lake, 1989).

$$E_V = E_I \cdot E_A = \frac{\text{Volumes of oil contacted by displacing agent}}{\text{Volumes of original oil in place}} \tag{3.2}$$

The various chemical, miscible and thermal EOR methods will increase the recovery efficiency by increasing E_D, E_V or a combination of both. Injection of surfactant is a well documented method to increase the displacement efficiency (E_D), as it facilitates the production of trapped oil in pore throats through the reduction of IFT (Hirasaki et al., 2011; Gilliland and Conley, 1975; Healy and Reed, 1974). Injection of polymer and steam is effective at increasing displacement efficiency and volumetric sweep efficiency, because they enhance the mobility ratio of the displacing agent and oil by increasing the viscosity of displacing fluid or decreasing the viscosity of oil respectively. As seen in Figure 3.2, this will enhance the propagation of the displacing fluid in the reservoir (E_V) and prevent viscous fingering (E_D) since it makes the displacing fluid flow more slowly than the oil. Since some nanoparticles affect fluid interactions in the same way as surfactants (Patel et al., 2017) and polymers (Habibi et al., 2010), they may become popular alternatives with further development considering material cost and applicability.

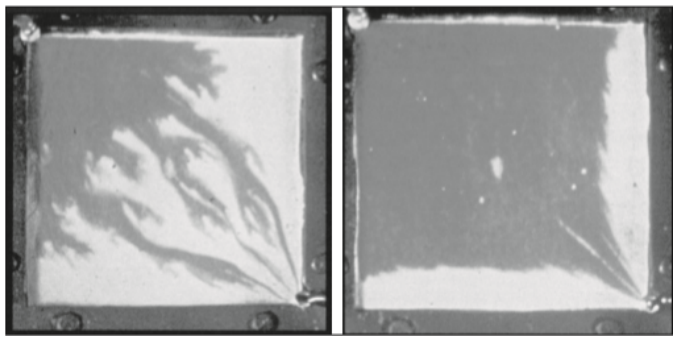

Figure 3.2: Comparison of sweep efficiency from waterflooding (left) and polymer flooding (right). The unsteady displacement on the left is known as viscous fingering (Sheng, 2011)

3.2 Field Applications of EOR Methods

Field applications of chemical, thermal and miscible EOR methods have been conducted over the years, only some have turned out to be economically successful. These are mostly projects where thermal and miscible methods such as steam flooding, hot-water flooding or gas injection have been applied. Some chemical EOR projects with surfactant or polymer flooding have been technically successful, but economically unsuccessful due to the high price of chemicals. So far, the EOR projects with the largest economical success have used fluids which can be injected in several barrels per barrel of produced oil (Taber, 1990).

The EOR project in Wilmington, California in 1984 demonstrates some of the challenges that can be met when applying EOR methods at field scale. After 21 years of production with waterflooding the water cut had reached 94%, and injection of CO_2 was considered as a means to increase oil production. A mixture of CO_2 and N_2 was injected in a water-alternating-gas (WAG) procedure, but it did not produce a substantial amount of incremental oil. It was concluded that only 1% of the injected gas was able to propagate from the high permeability layer to the less permeable layers in the reservoir, and that the displacement was not miscible at down-hole conditions due to a high minimum miscibility pressure (MMP) of the gas mixture. As an attempt to increase the sweep efficiency (propagation from high to low permeable layers), the injection of foam created by surfactant-alternating-gas (SAG) was proposed. After a two days of flow the foam treatment was able to increase the flow in the low permeability layers to 43%, making it a successful EOR project.

Even though though gas and foam injection have proved to be among the most economically feasible EOR methods, they require careful investigations of foaming properties and propagation rates at reservoir conditions. In addition there are some issues related to foam injection, such as thermal degradation of chemicals, wettability effects on stability and interaction with crude oil (Lee and Kam, 2013).

The steam flooding project in the Indonesia's Duri field was the largest steam EOR project in the world, with a production of 200.000 barrels of oil per day from steam flooding. The EOR project was unique considering the management of existing steam flooding areas and development and design of new steam flooding areas to maximize oil recovery and optimize production. The Duri oil had a viscosity and gravity of $\mu_o = 150\ cP$ and $\gamma_o = 22^o API$ respectively (Pearce and Megginson, 1991), which are ideal properties for steam flooding EOR. Nevertheless, steam flooding is not an ideal EOR method for all reservoirs as it is susceptible to heat loss during injection, and requires a lot of water which needs to be treated to reduce hardness (Sheng, 2013b).

An ASP flood was conducted as a secondary recovery mechanism in the Cambridge Minnelusa Field in Wyoming in 1993, one month after the waterflooding was initiated. Only 0.252 PV of ASP was injected before being displaced by a 0.244 PV polymer slug in 1996. When the displacing water was injected in the year 2000, the water cut was reduced by 36% and the residual oil after production was reduced to $S_{or} = 18.6\%$ (Sheng, 2013a). ASP flooding is recognized as one of the most efficient EOR methods, but its use is in

many cases restricted by the high chemical costs.

Nanotechnology for EOR is a rather new concept, and has not yet been extensively tested in large fields. However, some field tests with injections of colloidal dispersion gels (CGD) with a particle size of 50-150 nm (Skauge et al., 2010) have been successful in the Daqing field of China, with increased sweep efficiency as the main recovery mechanism (Chang et al., 2004). Field tests of nanoparticle suspensions which are capable of altering wettability and reducing IFT have not yet been conducted, probably due to today's low oil prices and uncertainties in terms of particle propagation and suspension stability at reservoir conditions.

4 Nanoparticles in Porous Media

The interaction between nanoparticles, crude oil, brine and reservoir rock is not completely understood, and more research is needed to optimize and control the desired effects when introduced to a petroleum reservoir. The innumerable unique nanoparticles that can be made by combining materials with various chemical compositions and sizes will lead to unique physical behaviors, which provide potential applications in various fields. This chapter will explain the fundamentals of nanoparticles and their suspensions, known as nanofluids.

4.1 Nanoparticles

Kestell and DeLorey (2010) define nanoparticles as zero-dimensional nanostructures, i.e. each spatial dimension is in the size range of 1-100 nm. The specific surface area of 1 gram of 7 nm SiO_2-nanoparticles (Aerosil® 300) is 300 m^2, which is approximately 1000 times bigger than the surface area of microparticles. The large specific area creates a large surface energy, which changes the particle's interatomic spacings and leads to some of the unusual properties seen in nanoparticles (Brydson and Hammond, 2005). It also makes them very reactive when surrounded by other materials (Lau et al., 2016), which explains their ability to easily adsorb on solid surfaces or on the IFT between immiscible fluids. As seen in Figure 4.1, the specific surface area increases with a decreasing nanoparticle size. The particle size is also responsible for some the special properties of nanoparticles, as it lies between the wavelength of quantum effects (1-250 nm) for atoms, molecules and bulk materials (Pitkethly, 2004). This will damage periodic boundary conditions, which cause dramatic changes to properties such as optical absorption, thermal resistance, catalysis, chemical activity and internal pressure (Kong and Ohadi, 2010).

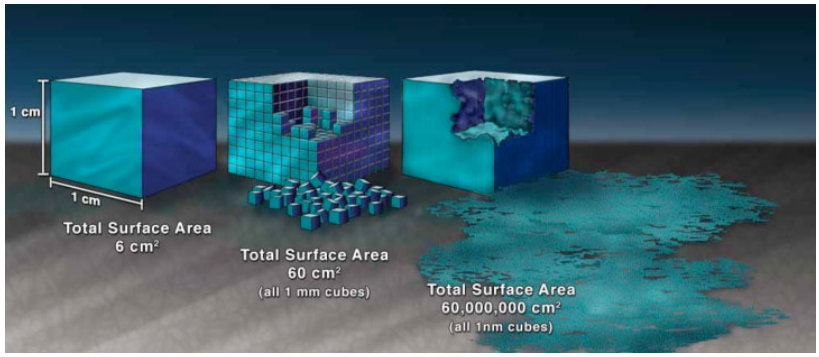

Figure 4.1: The effect of the increased surface area provided by nanostructured materials (U.S. National Nanotechnology Initiative, 2010)

4.1.1 Fabrication of nanoparticles

Nanoparticles can be made by assembling atoms or by removing and reforming atoms from a particle to achieve the desired structure. These methods are respectively known as the "bottom-up" and "top-down" processes. Atoms, molecules and even small-sized nanoparticles can be used to build nanoparticles in the "bottom-up" approach. By having control over the size, chemistry, organization and assembly of the building blocks, it is possible to engineer desired functionality and overall design of the nanoparticles through controlled chemical synthesis. Some examples of industrial "bottom-up" processes are *vapor phase deposition, liquid phase and colloidal methods*. The vapor phase deposition technique uses chemical and physical methods to convert the solid building blocks into gaseous phases, before they are cooled and re-deposited on a substrate. The liquid phase method synthesizes precursors into nanoparticles chemically by making them react or naturally self-assemble in an aqueous or non-aqueous solvent. The colloidal methods disperse nanoparticles in solvents by applying sufficient work/energy to surpass their surface energy. After some time the particles will aggregate to reduce their surface energy, which results in the making of larger nanoparticles (Kelsall et al., 2005).

The "top-down" approach is simpler, as it aims to remove material from the nanoparticle or simply break it into smaller particles. *High-energy ball milling* is a low cost fabrication technique with large industrial importance, as can be operated at a large scale. The method uses rotating drums of hard steel to mechanically crush nanoparticles in the form of powder into smaller sized particles. Other "top-down" methods include hammering and rolling (Ramsden, 2011).

4.2 Nanofluids

Nanofluids are suspensions of nanoparticles in liquid mediums. Thus, a nanofluid is a two-phase system with a solid (nanoparticle) phase in a liquid phase. The liquid mediums can either be polar or non-polar, depending on the hydrophilicity/hydrophobicity of the nanoparticle surface. The polarity of the liquids will influence solubility, stability and growth control of the nanoparticles (Sastry, 2003).

The sedimentation velocity of nanoparticles in liquid suspensions is determined by Stokes law, which is expressed in equation 4.1. Discrete nanoparticles may withstand sedimentation if the gravitational force on the small particles is balanced by the diffusive forces of Brownian motion (Ghadimi et al., 2011). However, nanoparticles tend to aggregate in order to reduce the surface energy, as described in the colloidal method of the "bottom-up" nanoparticle fabrication process.

$$v = \frac{2R^2}{9\mu}(\rho_p - \rho_l) \cdot g \tag{4.1}$$

Nomenclature of equation 4.1:
v: sedimentation velocity, μ: fluid viscosity, R: particle radius, ρ_p: particle density, ρ_l: liquid density, g: gravitational acceleration.

4.2.1 Stability Evaluation and Mechanisms

Nanofluid stability should be emphasized, as the agglomeration of nanoparticles will block micro channels in porous media and affect the desired properties of the nanoparticles. Suspension stability can be investigated with several methods, e.g. *spectral absorbency analysis, zeta potential analysis* and *sedimentation methods*. The spectral absorbency analysis utilizes a linear relationship between the absorbency intensity and the nanoparticle concentration in the suspension. Thus, evaluation of stability can be done by measuring the absorbency intensity of a nanofluid after a certain amount of time, and comparing the apparent concentration to the initial concentration of nanofluid (Hwang et al., 2007). A decrease in concentration would suggests particle sedimentation.

Zeta potential measures the electric potential difference between the dispersing medium and the fluid attached to the nanoparticle surface. The zeta potential of a nanofluid can be related to its stability, and fluids with an absolute value of ZP $\geq$ 40 mV are expected to show good stability.

The simplest method for stability analysis, is a visual test of nanoparticle sedimentation

in test tubes. A more quantitative analysis measures the weight or volume of nanoparticle sedimentation after an external force field has been applied to the nanofluid (Yu and Xie, 2012).

The traditional Derjaguin-Landau-Verwey-Overbeek (DLVO) theory of colloidal stability describes particle-particle and particle-surface interactions which control deposition and aggregation in aquatic environments. According to this theory, the stability of nanoparticles in an aqueous suspension can be determined by the sum of van der Waals (VDW) and electrical double layer interactions (EDL). The interaction energies of VDW attraction and EDL repulsion between two particles are expressed by in equation 4.2 and 4.3, respectively (Petosa et al., 2010). Nanofluid stability can be improved with non-DLVO interactions such as steric repulsion, which is an elastic repulsion between particles that are covered with an *elastic film*. By adding a polymer such as polyvinylpyrrolidone (PVP) to the nanofluid, the nanoparticles will get covered with the polymer and remain discrete in the suspension (Folttmann and Quadir, 2008; Hendraningrat and Torsæter, 2014). Equation 4.4 expresses the steric force between particles that are covered with a polymer, and Figure 4.2 shows the steric and electrostatic (DLVO) stabilization of nanoparticles. As seen

$$V_{VDW} = -\frac{A_{121}a_1a_2}{6h(a_1+a_2)(1+14h/\lambda)} \tag{4.2}$$

$$V_{EDL} = 64\pi\epsilon_0\epsilon_r\frac{a_1a_2}{a_1+a_2}\left(\frac{k_BT}{ze}\right)^2\Gamma_1\Gamma_2e^{-\kappa h} \tag{4.3}$$

$$F_{ST}(h) = 2\pi\left(\frac{a_1a_2}{a_1+a_2}\right)\left(\frac{k_BT}{s^3}\right)\left(\frac{8l}{5}\left[\frac{2l}{h}^{\frac{5}{4}}-1\right]+\frac{8l}{7}\left[\frac{h}{2l}^{\frac{7}{4}}-1\right]\right) \tag{4.4}$$

Nomenclature of equation 4.2, 4.3 and 4.4:
A_{121}: Hamaker constant, a_i: particle radius, h: separation distance, λ: characteristic wavelength, ϵ_0: dielectric permittivity in vacuum, ϵ_r: relative dielctric permittivity of solution, k_B: Boltzmann constant, T: absolute temperature, z: counterion valence, e: electron charge, Γ_i: dimensionless surface potential for particle, κ: inverse Debye length, l: polymer film thickness, s: distance between polymer chains on a surface.

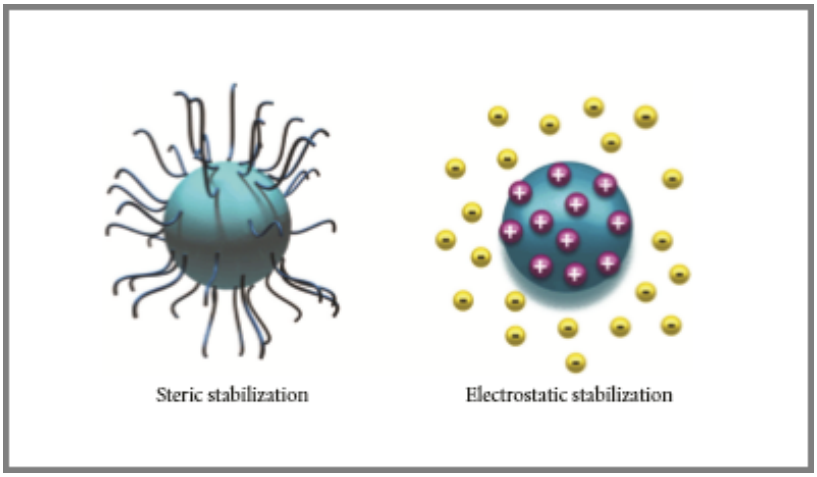

Figure 4.2: Colloidal stabilization of nanoparticles (Yu and Xie, 2012)

4.3 Silica-Based Nanofluids

Fumed silica (SiO_2) nanoparticles have gained much interest over the last years as they are relatively cheap to produce and have many applications. Silica nanoparticles consist of more than 99% SiO_2 (main mineral in sandstone), which makes the particles more environmentally friendly than many other potential candidates for EOR. It has been shown that silica nanoparticles are able to mobilize trapped oil, which makes them suitable for EOR applications (Hendraningrat et al., 2012; El-Diasty, 2015).

In most studies conducted on silica nanoparticles for EOR, the nanoparticles have been dispersed in solutions of NaCl. Silica nanoparticles are stable in low salinity NaCl-solutions and will first start to aggregate when the salinity reaches 1.5 wt%, known as the critical salt concentration (CSC). If the synthetic seawater (SSW) contains small amounts of divalent ions such as Mg^{2+} and Ca^{2+} the CSC is lowered, which leads to increased aggregation and sedimentation of particles at an earlier stage. A similar effect on the CSC is observed in saline nanofluids at elevated temperatures (Metin et al., 2011; Abdelfatah et al., 2017). In order to counter the destabilizing effects of the cations, Ortega et al. (2016) added small amounts of hydrochloric acid (HCl) to SiO_2 nanoparticles dispersed in real seawater from the Hebron field. The nanofluids were successfully stabilized for reservoir conditions (T = 62^{o}C and P = 190 bar) by adding 46, 138 and 230 ppm HCl to suspensions with nanoparticle concentrations of 0.01, 0.03 and 0.05 wt%, respectively.

4.3.1 EOR mechanisms

Silica nanofluids may improve oil recovery by reducing the IFT between oil and water, increasing the suspension viscosity and make reservoir rocks more water-wet. Li et al. (2013) demonstrated that the IFT of oil and water can be reduced to half of initial value with a concentration of only 0.01 wt%. This alone is not enough to mobilize capillary trapped oil (Xu et al., 2011), but it may act as an assisting displacement mechanism. Addition of nanosilica to the displacement liquid will increase its viscosity and improve the macroscopic displacement in reservoirs. According to Bazazi et al. (2017), the viscosity of a 4 wt% nanofluid with 30 nm nanosilica is 13 % higher than in normal brine.

Oil displacement due to wettability alteration is a more complex process. When silica nanoparticles are introduced to a rock-oil-water system, the particles will order into microstructures, known as *wedge-films*, between the oil droplets and the rock surface. This happens spontaneously, since it will increase the entropy of the overall colloidal dispersion. The tight ordering of nanoparticles in the wedge-film will exert an excess pressure to the oil droplet's surface, called the *structural disjoining pressure*, which eventually separates the oil from the rock surface. As the size of the wedge-film increases, the film thickness decreases due to Brownian motion of the particles (Wasan et al., 2011; Nikolov et al., 2010). In addition to diffusion (Brownian motion), electrostatic repulsion between the particles is an assisting drive mechanism of the structural disjoining pressure. Although the applied pressure from one nanoparticle is weak, the pressure exerted by a wedge-film at the vertex of the oil-rock interface can be up to 0.5 bar (McElfresh et al., 2012).

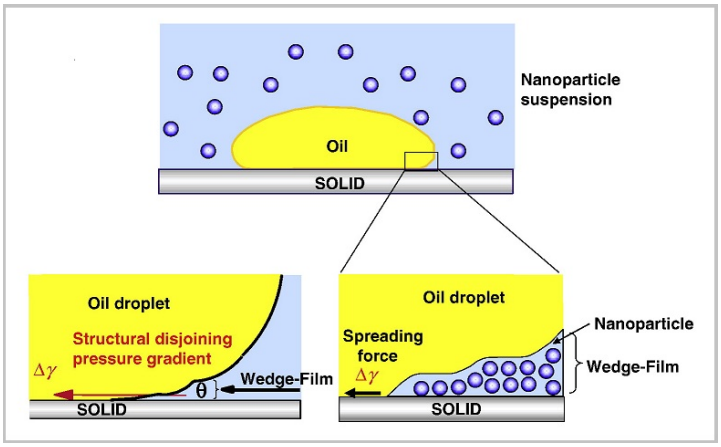

Figure 4.3: Disjoining pressure exerted by nanoparticles on an oil film (Wasan et al., 2011)

In order to successfully alter the rock wettability with silica nanoparticles, some particles must be retained on the pore surfaces of the rock. By assuming that nanoparticle adsorption will first form a single layer of particles on pore surfaces, the surface area of nanoparticles in porous media (with various compositions *i*) can be estimated with equation 4.5. After a rock has been injected with nanoparticles, it is possible to evaluate their surface coverage by comparing the surface area to the specific area of the injected rock. If the injected rock is a sandstone core, the specific area can be estimated by the empirical correlation in equation 4.6. An ideal wettability alteration requires all pore surfaces in the reservoir to be adequately but not excessively covered with nanoparticles ($S \approx S_v$), since continuity of deposition will just lead to reduction of porosity and permeability (Ju et al., 2002).

$$S = \beta \sum_{i=1}^{n} S_i = \beta \sum_{i=1}^{n} (V_i + V_i^*) \frac{6}{d_i} \tag{4.5}$$

$$S_v = 7000\phi \sqrt{\frac{\phi}{K}} \tag{4.6}$$

Nomenclature of equation 4.5 and 4.6:
S: total surface area of nanoparticles, β: surface area coefficient, S_i: surface area of nanoparticles with composition *i*, V_i: volume of adsorbed nanoparticles with composition *i*, V_i^*: volume of entrapped nanoparticles with composition *i*, d_i: diameter of nanoparticles with composition *i*, ϕ: porosity, K: permeability.

4.3.2 Transport and Retention in Porous Media

The small size of silica nanoparticles (5 - 50nm) allows them to easily pass through micro-sized reservoir pores, but physicochemical interactions such as agglomeration and adhesion to pore surfaces may lead to significant retention. The adsorption of nanosilica may be reversible and irreversible (i.e. particles desorb), and the irreversible adsorption will increase if the nanoparticle concentration increases, the flowrate decreases or the specific surface area of the porous media decreases. The specific surface area of sandstone depends on the clay content, which suggests that reversible adsorption (desorption) increases with an increase in clay content (Zhang et al., 2013).

Hendraningrat et al. (2013a) investigated the porosity and permeability impairment in Berea sandstone due to retention of nanostructured silica particles (NSP). The nanofluid consisted of lipophobic-hydrophilic particles with an average size of 7 nm and a specific surface area of 300m^2/g, dispersed in 3 wt% NaCl solution. Data from the core flooding experiments showed a reduction in rock permeability after nanofluid injection, with 90% reduction as the maximum impairment. It was found that the retention increased with both concentration *and* injection rate, which is slightly different from what Zhang et al. (2013) observed with their **surface coated** nanosilica.

As illustrated in Figure 4.4, nanoparticles are normally retained in porous media due to four entrapment mechanisms: adsorption, size exclusion/mechanical entrapment, gravity settling and bridging/log-jamming. Adsorption of nanoparticles onto rock surfaces occurs because of particle diffusion and electrostatic interaction between the flowing particles and the pore surfaces. Size exclusion happens when the particle size is bigger than the pore size. This is a phenomenon which relates mostly to large particles (micron-sized), but it may also occur during nanofluid flooding with poor stability since some particles will form micron-sized agglomerate. Gravity settling of particles is a result of a dominating gravitational force due to a large particle size, as discussed for Stokes law in equation 4.1. Bridging or log-jamming may happen when multiple nanoparticles invade a pore throat at the same time, as particles can get jammed when the flux area suddenly decreases. Adsorption is the main entrapment mechanism for nanoparticles, while size exclusion is the main mechanism for particles larger than the pore neck (Gao, 2007).

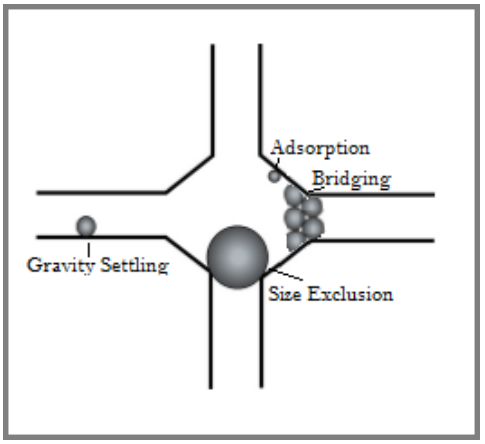

Figure 4.4: Entrapment mechanisms of nanoparticles (Gao, 2007)

Formation damage from nanoparticle retention can be evaluated in terms of porosity and permeability reduction. Liu and Civan (1993) presented predictions of porosity and permeability reduction due to external particle invasion and formation fines migration, as expressed in equation 4.7 and 4.8 respectively.

$$\phi = \phi_0 - \sum \Delta\phi = \phi_0 - (V_i + V_i^*)\frac{1}{V_b} \tag{4.7}$$

$$\frac{K}{K_0} = \left[(1-f)k_f + f\frac{\phi}{\phi_0}\right]^3 \tag{4.8}$$

Bridging and plugging of pore throats is stochastic and will inhibit flow in some of the pore throats. This will decrease the flow efficiency factor, *f*, in equation 4.8, which is defined as the fraction of original flux area that is still open for flow. Ju et al. (2002) simplified the flow efficiency factor to a linear function of entrapped nanoparticles by plugging or bridging, as seen in equation 4.9.

$$f = 1 - \alpha_{fe} V_i^* \tag{4.9}$$

Nomenclature of equation 4.7, 4.8 and 4.9:
ϕ: instantaneous porosity, ϕ_0: initial porosity, V_i: volume of adsorbed nanoparticles with composition *i*, V_i^*: volume of entrapped nanoparticles with composition *i*, V_b: bulk volume of rock, K: instantaneous permeability, K_0: initial permeability, f: flow efficiency factor, k_f: fluid seepage constant, α_{fe}: flow efficiency rate constant.

If future field applications of nanosilica for EOR are to be realized, the issues of nanofluid instability need to be addressed. A potential field project requires robust nanoparticle suspensions which are capable of maintaining colloidal stability and functionality at reservoir conditions. Rahmani et al. (2015) proposed a method to stabilize silica nanoparticle suspensions at high temperature and salinity by using a polymer coating with both positive and negative ionic groups, which induces steric repulsion between the particles. A cheaper and simpler approach is to add acid to the suspension, as demonstrated for Hebron reservoir conditions by Ortega et al. (2016).

5 Materials and Methods

This chapter introduces the reader to the materials and methods used for the experimental part of this thesis. Transport of silica nanoparticles in Berea sandstone was studied for single-phase flow in core samples, and the retention of nanoparticles was measured. The use of hydrochloric acid (HCl) as a nanofluid stabilizer was investigated as an attempt to limit pore blockage and excessive adsorption of nanoparticles during the transportation in porous media. The wettability of the sandstone core samples was altered from strongly water-wet to intermediate wet for the core flooding experiments, since reservoirs with this wettability condition probably are the most common worldwide (Cosentino, 2001), and because these are good candidates for nanofluid EOR.

5.1 Materials

The materials used in the experimental nanofluid injection procedure included sandstone core samples, Aerosil® 300 nanoparticles, HCl and synthetic seawater (SSW). Sodium iodide (NaI), SurfaSil^{TM}, n-pentane and n-decane were used for preparations prior to the injection sequence, to establish adsorption calibration curves, alter the rock wettability and to evaluate wettability alteration, respectively.

5.1.1 Core samples

Twenty Berea sandstone core samples were used in the experimental study, of which eleven cores were high permeable and nine cores were low permeable. The dimensions of the core samples were measured with a digital caliper in order to calculate their bulk volumes, which would be used for the determination of porosity later on. The bulk volume

was calculated by equation 5.1, which expresses the volume of a cylinder.

$$V_b = \pi \frac{D^2}{4} L \tag{5.1}$$

Nomenclature:
V_b: bulk volume of core sample, L: length of core sample, D: diameter of core sample.

The core samples that were used in the experimental procedure had recently been drilled out, and therefore needed to be cleaned before proceeding with the experiments. The cores were first scrubbed in a saltwater bath to clean out any residing dirt, before they were submerged in methanol over night to clean out the salts. The cores were collected after 24 hours and put inside an oven of T = 60^{o}C for another 24 hours to evaporate the methanol. The core samples were then collected from the oven and weighed, before being put in clean and sealed beakers to prevent contamination.

5.1.2 Aerosil® 300

Aerosil 300 (A300) are hydrophilic silica (SiO_2) particles produced by Evonik Industries, with an average particle size and surface area of 7 nm and 300 $\pm$ 30 m^2/g, respectively. Since A300 consists of more than 99.8 % SiO_2, which is the main mineral in sandstone, they are regarded as environmentally friendly, which should make the injection juridically feasible in petroleum reservoirs all over the world. The A300 nanoparticles are known as fumed silica, due to their creation by *flame hydrolysis*. The nanoparticles are nanostructured (NSP), i.e. they easily aggregate to form chain-like/branced agglomerate in aqueous suspensions. This particle aggregation is responsible for making the colloidal suspensions unstable when dispersed in seawater. The pH of the particles in powder form ranges from pH = 3.7 - 4.5 (Evonik, 2015).

5.1.3 Synthectic Seawater

The synthetic seawater (SSW) used for the experiments had a salt concentration of 3.8 wt% TDS (total dissolved solids), and had a more complex composition than ordinary brine. The complex SSW was made to imitate real saltwater, since the presence of divalent ions was believed to affect the transport mechanisms of the A300 nanoparticles significantly. For the mixing of SSW, mono- and divalent salts were weighed into deionized (DI) water on a laboratory scale while mixing with a magnetic stirrer. The complete composition of

the SSW is presented in table 5.1.

SYNTHETIC SEAWATER (SSW)		
Salts	Concentration (g/L)	CAS No.
CaCl2. 2H2O	1,76	10035-04-8
MgCl2. 6H2O	11,23	7791-18-6
Na2SO4	4,81	7757-82-6
NaCl	27,03	7647-14-5
Ions	PPM	
Na+	12188	
Ca2+	480	
Mg2+	1342	
SO4 2-	3250	
Cl-	21157	
Total TDS	38417	

Table 5.1: Salt composition of SSW

5.1.4 SurfaSil^{TM} Solution

A chemical solution of SurfaSil and n-pentane was used to change the wettability of the sandstone core samples from strongly water-wet to intermediate wet. SurfaSil is a clear short-chained polymeric silicone liquid which primarily consists of dichloroocta-methyl-tetrasiloxane ($C_8H_{24}Si_4O_3Cl_2$). The chemical adheres to glass (SiO_2) surfaces easily, which makes it suitable for surface coverage in sandstone core samples as well.

The SurfaSil was dispersed in n-pentane, as it is a highly volatile oil which does not affect quartz wettability. A solution of 10 vol% SurfaSil and 90 vol% n-pentane was made for the wettability alteration process, as this blend is capable of making the rock surfaces intermediate wet (Afrapoli et al., 2009). Since SurfaSil is highly flammable, corrosive and probably toxic to breathe, the solution was carried out under a fume hood.

5.1.5 Tracer Solution

A tracer solution was made by mixing small amounts of NaI in liquid form with SSW. A 100 ppm solution was initially made on the laboratory scale for acceptable accuracy, and was then diluted to a 20 ppm solution for the injection process. The use of NaI as a tracer is beneficial because it is easily detected by the UV-Vis apparatus (see section 5.2.4), which makes the measurement of the effluent concentration a convenient process.

5.2 Methods

The laboratory experiments were conducted as follows: 1) Core samples were aged in surfaSil/n-pentane solution, 2) Core samples were then saturated with brine in vacuum to determine porosity, 3) Injection fluids were prepared, 4) Core samples were flooded with SSW/tracer/nanofluid, 5) The light absorbency of effluents was measured to estimate adsorption.

5.2.1 Aging of Core Samples

Two of the high permeable core samples (T1 and T2) were first aged in the SurfaSil solution as a trial of wettability alteration. The core samples were saturated in the vacuum saturation setup seen in Figure 5.1 for three days, followed by three days of drying in the oven to evaporate any liquid that did not adsorb on the rock surface. For the saturation process, cores T1 and T2 were put in a small bucket and inserted into the exicator. The flask in the stand was then filled with SurfaSil/n-pentane solution, which was contained with a valve in the bottom of the flask. The vacuum pump was turned on, and the air exited the system through the gray tube seen on the left in Figure 5.1. The pump was allowed to run for three hours to make sure that complete vacuum was achieved, before the SurfaSil/n-pentane solution was let into the bucket with core samples by opening the valve beneath the flask.

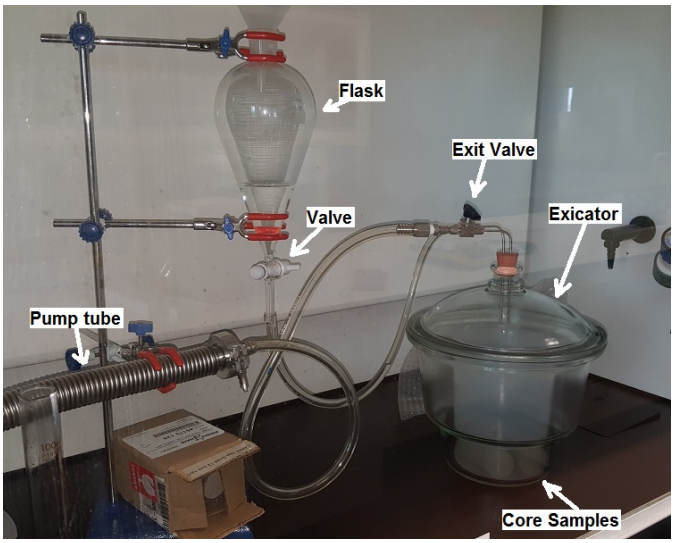

Figure 5.1: Vacuum saturation setup

After the saturation process was completed, the core samples were dried in the oven, followed by weighing. The adsorbed amount of SurfaSil was determined by mass balance before and after aging, as seen from the data in Appendix A.1. The wettability alteration due to SurfaSil adsorption was investigated by saturating T1 and T2 with 3.8 wt% SSW and n-decane, respectively, followed by insertion in amott cells with opposite liquids. The amott experiment on T1 and T2 is seen in Figure 5.2. The spontaneous production of water and oil from T1 and T2 due to imbibition/drainage was used to determine the new wettability of the cores by using equation 2.4. Since only small amounts of oil (and no water) was produced, the wettability of T1/T2 was concluded to be intermediate wet.

The remaining eighteen core samples were aged in the same manner as the two test cores after concluding successful wettability alteration, but the time duration of the aging process was shortened to 4 hours due to time constraint.

Figure 5.2: Amott experiment on cores T1 and T2

5.2.2 Porosity Measurement

After the wettability of the eighteen core samples had been altered, the core samples were saturated with 3.8 % SSW in the same setup as seen in Figure 5.1. The core samples were saturated in two batches, separated by permeability. The same procedure for vacuum saturation as in section 5.2.1 was used for the SSW saturation. Mass balance was used to determine the mass of SSW inside the core samples after saturation. A digital densimeter (seen in Appendix B.1) was used to measure the density of SSW, to convert the determined SSW mass into liquid volume. Due to vacuum saturation, the volume of SSW in the core

samples was assumed to occupy the interconnected pores completely ($V_P = V_{SSW}$), hence the effective porosity of the core samples was calculated with equation 2.1 in chapter 2.

5.2.3 Permeability Measurement

Twelve intermediate wet core samples (six high permeable, six low permeable) were chosen for the core flooding experiments. The *liquid* permeability was determined by core flooding with SSW at a constant flow rate, with the setup seen in Figure 5.3. The same core flooding setup was used for injection of nanofluid and tracer, which were held by accumulators B and C, respectively. Only accumulator A was used during the liquid permeability experiment as it contained SSW. Darcy's law was rearranged for the calculation, and is seen in equation 5.2. The required SSW viscosity in equation 5.2 was determined by a digital viscometer.

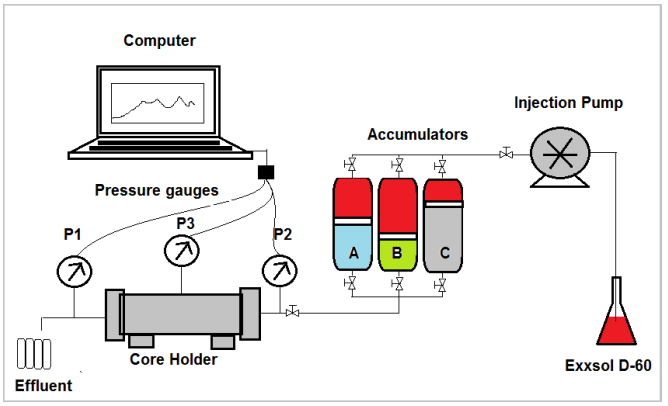

Figure 5.3: Core flooding setup. A: SSW, B: nanofluid, C: tracer solution

Each core was first inserted into the core holder and a sleeve pressure of $P_{sleeve} \approx 20$ bar was applied around the core during flooding. This was done to make sure that the core sample was kept in place and that the flow of SSW remained uniaxial. Injection accumulator A was filled with SSW, and all the tubes in the setup were filled with fluids and connected. All valves between the core holder, accumulator A and the injection pump were opened for flow, and the injection pump was started. The pump injected Exxsol D-60 into an accumulator, which pushed a piston that injected SSW into the core holder. The pressures at the inlet and outlet of the core holder were recorded continuously during flow with Control Center Series 30 (software) as a function of time. An average value of the

differential pressure was used for the permeability estimation.

$$k_L = \mu \frac{Q}{A} \frac{L}{\Delta P} \tag{5.2}$$

The resulting instantaneous permeability due to nanofluid injection was also calculated with equation 5.2, and the permeability impairment was determined by the ratio of instantaneous and initial permeability. For the core flooding experiments regarding tracer/nanofluid injection, the valves of accumulator A were closed while the valves of accumulators B or C were opened when tracer or nanofluid injection was initiated, respectively. Before each flooding, the injection fluids were degassed with an ultra-sonication device to restrict the presence of air bubbles in the system. The device and a beaker with fluid under sonication is seen in Figure 5.4.

Figure 5.4: Ultra-sonication of SSW in sonicatior bath

5.2.4 Preparation of Nanofluids

Nanofluids were made in fume hoods by mixing A300 nanoparticles with SSW, followed by magnetic stirring and ultra-sonication for 10-15 minutes. Several batches of nanofluids in the concentration regime of C_{NP} = [0.05, 0.1, 0.15, 0.2] wt% were prepared, and HCl and CH_3COOH were respectively added as stabilizers to some of the batches in order to investigate their effect on colloidal stability with a varying nanoparticle (NP) concentration. HCl and CH_3COOH were weighed into the NP suspensions on a fine scale to yield solution acid concentrations of C_{HCl} = C_{CH_3COOH} = [0.01, 0.05, 0.1, 0.5] wt%. The four acid concentrations were tested in each of the four nanofluids with various NP concentration, yielding a total of sixteen unique samples of both A300+HCl nanofluids and A300+CH_3COOH nanofluids (32 in total). The colloidal stability of the various nanoflu-

ids was visually analyzed over four weeks, by comparing the sedimentation volume at the bottom of the test tubes.

5.2.5 pH Measurement

The pH of the different solutions was measured with pH-paper as a preliminary indication, in order to find approximate values of the maximum acceptable acid concentrations for the core flooding experiments. It was assumed that the tubes in the flooding equipment could handle a minimum pH_{min} of 3.5, hence this was determined to be the lowest acceptable pH of the solutions. More accurate pH measurements were made with the Mettler Toledo SevenCompact pH meter (seen in Appendix B.1), which was able to detect small pH variations due to altering NP and acid concentrations. The pH meter was first calibrated with three reference liquids, before measurements were conducted on nanofluids with seemingly acceptable acid concentrations. All measurements were conducted twice for consistency purposes, and to ensure that the solutions were not too acidic for the core flooding experiments.

5.2.6 Particle Size Distribution

Particle size distribution (PSD) measurements in nanofluids are used for characterization, and can provide information of suspension stability by detecting large particles in the solution. The Malvern Zetasizer was used for PSD measurement in the nanofluids, by giving the silica's refractive index (RI) and the dispersant (SSW) viscosity as inputs. The zetasizer uses dynamic light scattering (DLS) to measure nanoparticle size, which is a consequence of the interaction between light and the electric field of a small particle. The DLS measures the velocity of particles undergoing Brownian motion, and relates it to the hydrodynamic particle diameter for constant and predetermined dispersant viscosity and temperature. The Stokes-Einstein equation which relates velocity of Brownian motion (determined by the particles' diffusion coefficient) to nanoparticle diameter is seen in equation 5.3 (Shaw, 2016).

$$d_H = \frac{kT}{3\pi\mu D} \tag{5.3}$$

Nomenclature:
d_H: hydrodynamic diameter, k: Boltzmann's constant, T: temperature, μ: viscosity, D: translational diffusion coefficient.

5.2.7 Adsorption Measurement

The adsorption of tracer or nanoparticles in core samples was determined by concentration balance of the injected fluid and the produced effluent from the core sample. Adsorption is correlated to the dimensionless concentration (DC) of a chemical, which is expressed in equation 5.4 by Sheng (2011). The equation is simplified when the initial concentration of the chemical in the core sample is C_0 = 0. If the DC is 100 % it suggests that 0 % tracer/nanoparticles are adsorbed, and vice versa.

$$DC_{T/NP} = \frac{C_{eff} - C_0}{C_{inj} - C_0} = \frac{C_{eff}}{C_0}, C_0 = 0 \tag{5.4}$$

Nomenclature of equation 5.4:
$DC_{T/NP}$: dimensionless concentration of tracer/nanoparticles, C_{eff}: tracer/nanoparticle concentration in the effluent, C_{inj}: injection concentration of tracer/nanoparticle, C_0: initial concentration of tracer/nanoparticle.

In order to calculate the DC of fluid sample, the effluent concentration had to be known, as seen from equation 5.4. The UV-Vis apparatus is capable of determining the concentration of a certain chemical in liquid solution indirectly, by comparing the light absorbency of a fluid sample to a reference sample without the desired chemical. Calibration curves were established for the studied chemical (tracer of nanoparticle) to back-calculate the measured light absorbency to chemical concentration, which was done by measuring the light absorbency of liquid solutions with known concentrations of tracer/nanoparticle. Since every ¼ PV of effluent was collected in sample tubes, the calculated $DC_{T/NP}$ could be plotted against injected PVs of tracer/nanofluid with acceptable resolution (4 data points per PV). An image of the UV-Vis apparatus is seen in Figure B.7 of Appendix A.3.

5.3 Scanning Electron Microscopy

A scanning electron microscope (SEM) was used to visually investigate the presence of nanoparticles on the rock surfaces. The SEM creates a highly magnified image by scanning a focused electron beam over a surface. When the electrons come in contact with the atoms on the scanned surface, they produce signals with information about the surface composition (Nanoscience Instruments, 2017). The SEM-analysis was carried out by Dr. Shidong Li at ICES.

6 Results

The presented results correspond to the experimental methods discussed in chapter 5 - Materials and Methods. A total of twenty Berea sandstone core samples were used in the experimental procedure, with almost uniform dimensions of: L = 99.64 mm, D = 38.1 mm. Thus, the bulk volumes of the cores could be estimated by equation 5.1, yielding an average bulk volume of V_b = 114 cc. Two of the high permeable cores were used to evaluate wettability change after the aging process. The remaining eighteen cores were saturated with 3.8 wt% SSW, and twelve of these cores (six high permeable, six low permeable) were flooded with silica nanofluids to investigate permeability impairment and adsorption of particles. Details of experimental results and calculations are found in Appendix A, while the laboratory equipment is shown in Appendix B.

6.1 Aging of Core Samples

After two weeks of spontaneous imbibition/drainage in the amott cells, only the oil saturated core (T2) showed any production. This could indicate water-wet condition, but since the produced oil volume was only V_{o1} = 1 ml the cores were concluded to be intermediate wet. Since no forced imbibition/drainage experiment was conducted, the WI could not be determined. However, according to equation 2.4, less than 2 ml of oil must be produced from forced imbibition in core T2 if the cores are to be determined as water-wet. This is because the WI ranges from -0.34 to 0.34 for intermediate wet cores, as explained by Torsæter and Abtahi (2003). Such a small production from forced imbibition is very unlikely for high permeable cores with an average pore volume of PV = 23.9 ml (as seen in Appendix A.2), and the cores were therefore concluded to be intermediate wet. The adsorbed mass is presented for all cores in Figure 6.1. As seen from Figure 6.1, the adsorption in low permeable core samples is much lower than in high permeable core samples.

The wettability of the low permeable cores was not investigated with amott experiments, and the wettability alteration could therefore not be validated.

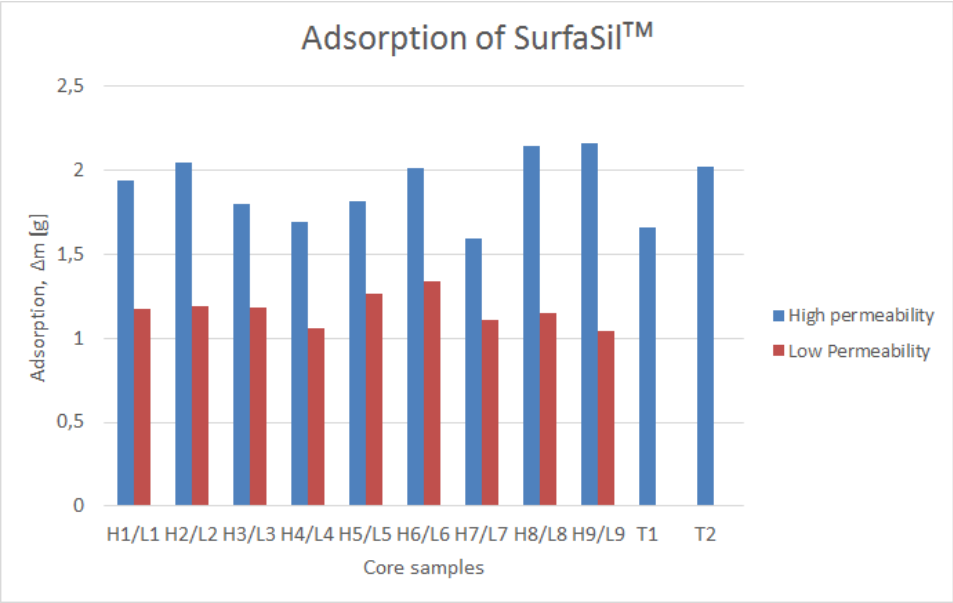

Figure 6.1: Adsorption of *SurfaSil* ™ on core samples

6.2 Porosity Measurement

The porosity of the high permeable core samples ranged from ϕ = 15.5 to 22.1%, with an average value of $\bar{\phi}$ = 21.0%. The mass of brine in the pores was determined by mass balance, and the liquid volume was determined by conversion with SSW density. The density was estimated to $\rho_w \approx$ 1.02 g/cc at T = 25^oC with the digital densimeter shown in Appendix B.1. The slow invasion of SSW (brine) in the core samples during vacuum saturation resulted in a reduced water level, which left the uppermost cores (H8 and H9) inadequately submerged in SSW (brine). After the saturation, core sample H8 was flooded with brine at high pressure as an attempt to achieve full saturation. After the flooding, the mass of core sample H8 had increased to a consistent value and complete water saturation was concluded. The porosity of the low permeable core samples ranged from ϕ = 18.5 to 19.2%, with an average value of $\bar{\phi}$ = 18.9%. Since there were no issues with the saturation of these cores, the results were more consistent than for the high permeable cores. The porosity of the low permeable core samples is normally lower than for high permeable core samples due to a less uniform grain size, which will also lead to a lower permeability. The porosity of the cores can be seen in Figure 6.2, and the relevant calculations are seen in Appedix A.2.

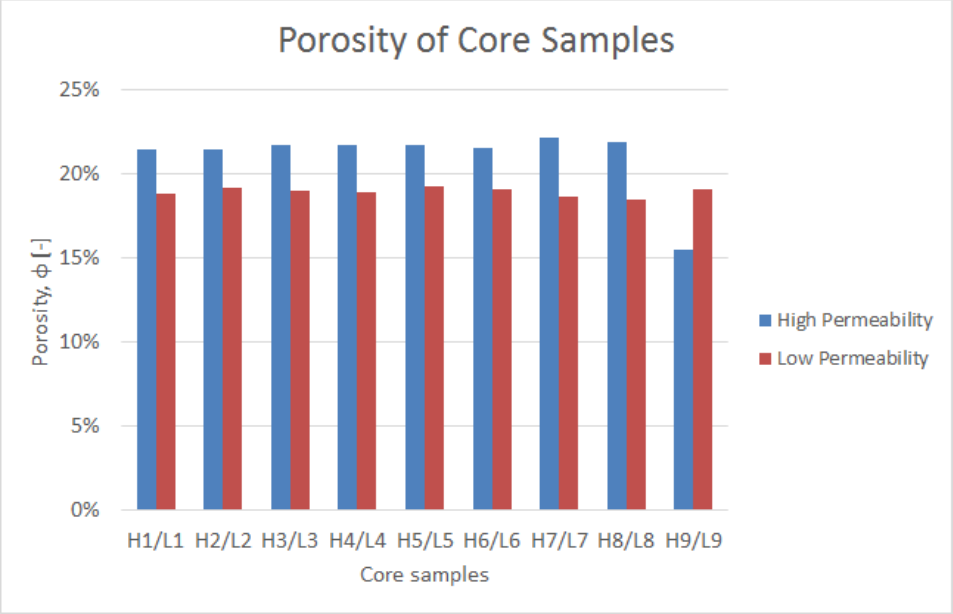

Figure 6.2: Porosity of high permeable and low permeable core samples

6.3 Permeability Measurement

The *liquid permeability* of twelve intermediate wet cores (six high permeable, six low permeable) is presented in Figure 6.3, and all the relevant data for the calculations are presented in Appendix A.3. The core permeabilies were estimated with the rearranged Darcy's law (equation 5.2), by measuring the pressure drop across the core sample during SSW injection at a constant flow rate of q = 1 - 3 ml/min, depending on the core sample. The dynamic viscosity of the injected SSW was measured to μ_{SSW} = 1.00 cP in T = 25°C with the digital viscometer. The high permeable core samples had a permeability range of k_H = 243 - 364 mD, with an average value of $\bar{k_H}$ = 323 mD. The low permeable cores had a permeability range of k_L = 118 - 182 mD, with $\bar{k_L}$ = 153 mD as the average permeability. The deviation

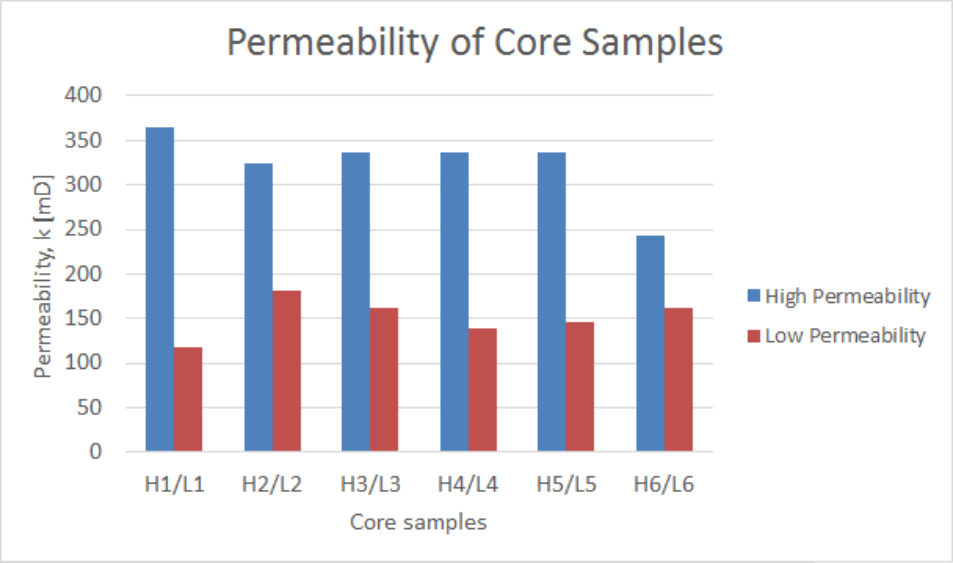

Figure 6.3: Permeability of high permeable and low permeable core samples

6.4 Preparation and Stabilization of Nanofluids

Sonication of the Aerosil 300 (A300) nanofluids enhanced suspensions stability immediately, which was seen by the increased transparency of the suspensions. The destabilization time of the silica nanoparticles was relatively short in 3.8 wt% SSW suspension, with the fastest destabilization of t = 4 days for the 0.20 wt% A300 nanofluid. The suspension with the lowest concentration NP concentration (C_{A300} = 0.05 wt%) showed signs of sedimentation after 7 days, which is consistent with the phase behavior observations presented by Metin et al. (2011).

The destabilization time of the A300 nanofluids increased when small amounts of stabilizers (HCl and CH_3COOH) were added, and the end-point sedimentation volume became significantly decreased. All combinations of acid and NP concentrations were used in the stability analysis, which together with the reference nanofluids (no acid) gave a total of 36 unique solutions. All solutions showed improved stability, and low concentrations of acid seemed to be almost as effective in reducing sedimentation volume as some of the higher concentrations. The largest sedimentation volumes were in fact seen in the 0.20 wt% A300 nanofluids with 0.5 wt% of HCl and CH_3COOH added, respectively. This suggests that there is a non-linear relation between stability and acid concentration, and that there could be an optimal acid concentration for maximum stability of silica nanofluids in SSW. Figure 6.4 shows the suspension stability of 0.20 wt% nanofluids with and without stabilizers at an early stage. An increased transparency is seen in the center and right-standing bottle compared to the left-standing bottle, which indicates increased suspension stability in the center and right-standing bottles.

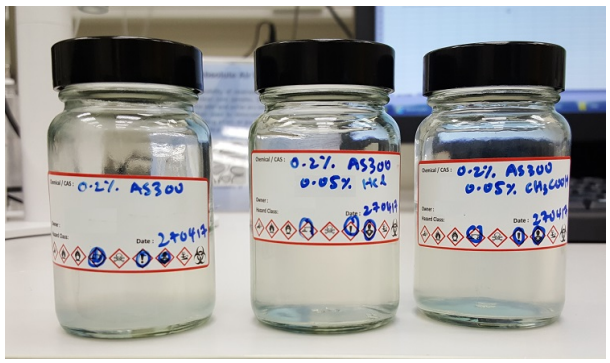

Figure 6.4: Stability analysis of 0.20 wt% A300 nanofluids. Left: No stabilizer, center: 0.05 wt% HCl, right: 0.05 wt% CH_3COOH

6.4.1 pH Measurements

The pH estimations of nanofluids with acid were made with pH indicators to find the maximum acceptable acid concentrations. The pH indicators used in A300+HCl are seen together with the pH indication chart in Figure 6.5. Each set of pH papers in Figure 6.5a have an increasing NP concentration from left (C_{A300} = 0.05 wt%) to right (C_{A300} = 0.20 wt%). The approximate pH values for all combinations of nanofluid and acid are listed in Appendix A.4. According to the estimations, even the lowest acid concentrations of C_{HCl} = $C_C H_3 COOH$ = 0.01 wt% showed solution pH values that were below the criterion for the core flooding equipment. Thus, the acid concentrations of HCl and CH_3COOH were diluted to C_{HCl} = 0.001 wt% and C_{CH_3COOH} = 0.005 wt% respectively, which yielded pH values of pH > 3.5 > pH_{min} for all NP concentration except one which was believed to be anomalous.

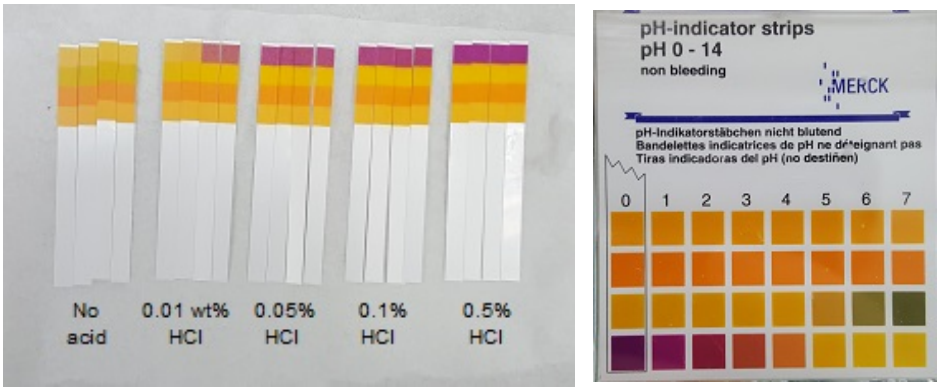

(a) pH vs. acid concentrations

(b) pH indicaton chart

Figure 6.5: pH of 0.05 wt% A300 nanofluid with varying acid concentrations

The pH of nanofluids with and without stabilizers were more accurately measured with a pH meter, and plotted against NP concentration as seen in Figure 6.6. The relationship between pH and NP concentration appears to be almost linear in all cases, with an apparent steeper slope for the nanofluid without stabilizer. The overall deviation of the measurements was small, with the largest margin of error being 7% for nanofluids with HCl. The maximum margin of error was considered acceptable, hence nanofluids with the given acid concentrations were approved for use in the core flooding setup. All pH data and standard deviations are presented in tables A.4 and A.5 in Appendix A.4.

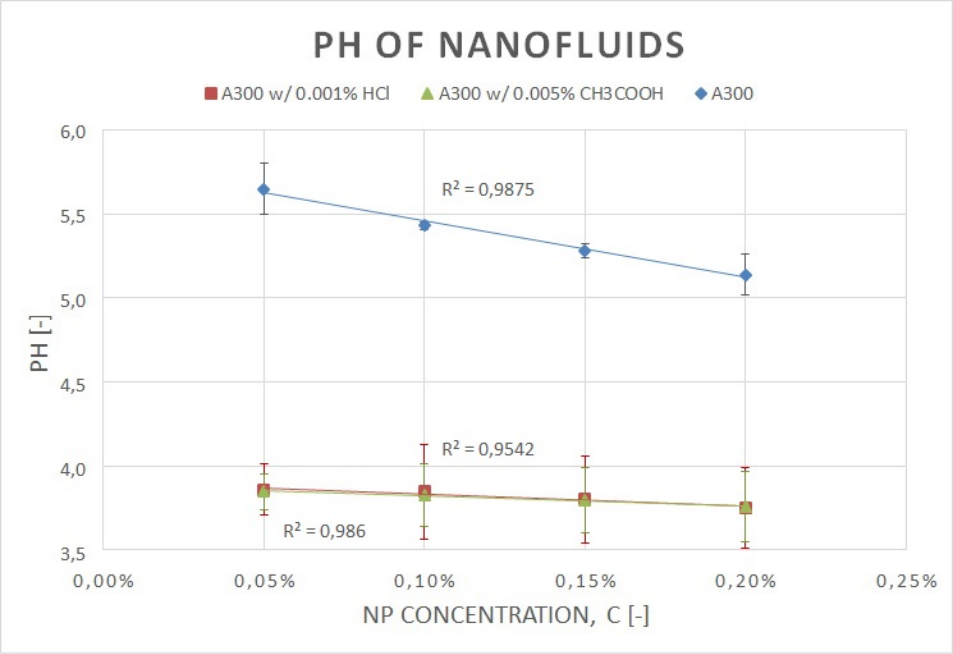

Figure 6.6: pH measurement of various nanofluids

The nanofluids with NP concentrations of 0.05 and 0.15 wt% were chosen for further experiments, since they showed the best stability response when adding acid to the solution. Additionally, silica nanofluid with an NP concentration of 0.05 wt% has proved to be especially effective at producing incremental oil (Hendraningrat et al., 2013b), which makes it a relevant fluid to optimize. HCl was chosen as stabilizer due to its low concentration requirement, and because it outperformed CH_3COOH in certain long-term stability tests. The stability of the chosen nanofluids was analyzed over a period of 28 days, with the first occurrence of sedimentation observed 7 days after the nanofluid was made. The resulting end-point sedimentation volumes were considerably reduced when HCl was added as a stabilizer. As seen in Figure 6.7, the sedimentation volume of the 0.05 wt% suspension with HCl was almost non-existent after 28 days. The 0.15 wt% suspension with HCl yielded a sedimentation volume which was approximately $^1/_3{}^{rd}$ of the sedimentation volume for the case without any stabilizer.

A visual stability analysis of 0.05 wt% and 0.15 wt% A300 nanofluids with 0.005 wt% of CH_3COOH was conducted before the stabilizer was discarded. The results are presented in Figure A.1 found in Appendix A.4.

(a) Left: 0.05% A300. Right:0.05% A300 + HCl, t=7 days

(b) Left: 0.15% A300. Right:0.15% A300 + HCl, t=7 days

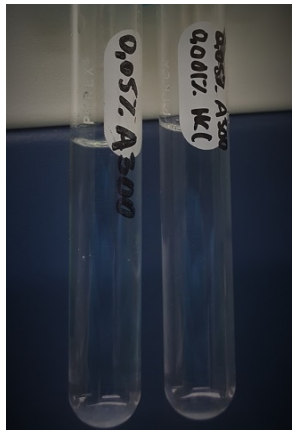

(c) Left: 0.05% A300. Right:0.05% A300 + HCl, t=28 days

(d) Left: 0.15% A300. Right:0.15% A300 + HCl, t=28 days

Figure 6.7: Stability analysis of nanofluids

6.4.2 Particle Size Distribution

The PSD was measured to investigate particle growth (agglomeration) in the suspensions, and the curves for nanofluids with and without stabilizer at T = 25^oC is seen in Figure 6.8. Even though the silica nanoparticles have an initial size of 7 nm, they will aggregate to larger sizes once dispersed in aqueous environments. The average particle size in aqueous suspension is about $Z_{avg} \approx 200$ nm. It is seen from Figure 6.8a that the average particle

size is slightly larger when the stabilizer is added, which would suggest that HCl decreases suspension stability and causes the nanofluids to form agglomerate. However, Metin et al. (2011) reported that the effective particle size of nanosilica could increase by a factor of 1.36 when the pH decreased from 10 to 2, but that the increase was **not** caused by aggregation.

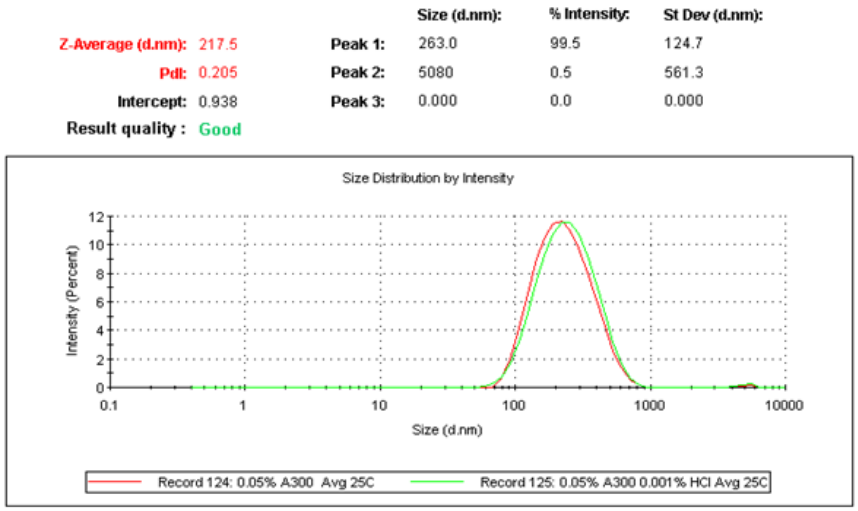

(a) Red: 0.05 wt% A300. Green: 0.05 wt% A300 + 0.001 wt% HCl

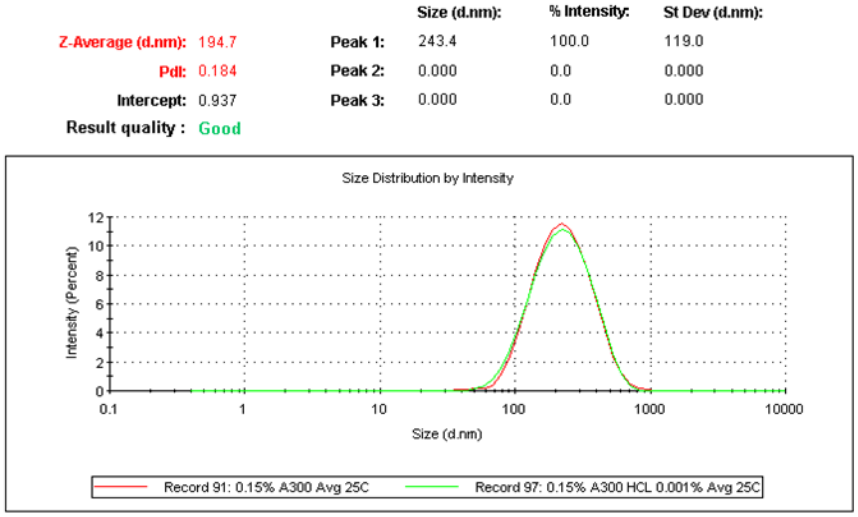

(b) Red: 0.15 wt% A300. Green: 0.15 wt% A300 + 0.001 wt% HCl

Figure 6.8: PSD of nanofluids at T=25^{o}C

A small secondary peak is seen on the micron-scale of the 0.05 wt% nanofluid without stabilizer in Figure 6.8a, which indicates that micron sized particles are present in the solution. In the same figure, no secondary peak is present on the PSD of the 0.05 wt% nanofluid with HCl. The PSDs of the nanofluids in Figure 6.8b have a three times higher NP concentration than those in Figure 6.8a, but show no presence of micron sized particles as seen from the absence of secondary low intensity peaks.

In order to analyze the suspension stability at typical sub-surface conditions, the temperature was elevated to T = 70^{o}C in all four nanofluid samples. The particle sizes remained well distributed in all cases, as seen by the smooth curves in Figure 6.9. An increase of the secondary peak's intensity is seen when comparing the PSDs of nanofluids without stabilizer in Figure 6.9a to 6.8a, suggesting that more micron sized particles are present in the high temperature solution. The PSDs in Figure 6.9b did not show any signs of micron-sized agglomeration in elevated temperature, as seen from a peak intensity of 100%.

PSD measurements were also conducted for 0.15 wt% nanofluids with CH_3COOH as the stabilizing agent. As seen in Figure 6.10, the Zetasizer detected micron-sized particles in the solutions with CH_3COOH at both low and high temperature, but no secondary peaks were detected for the other nanofluids. The presence of micron sized particles in solutions with CH_3COOH was surprising, since the visual analysis in Figure 6.4 suggested that it would enhance the suspension stability. The suspension stability of the three nanofluids with two stabilizers was compared with visual tests and can be seen in Appendix A.4.

The PSD curve for each nanofluid was created from an average of three DLS readings, with a 120 seconds break between each reading. This reduces the error of the measurement, but it does not exclude small variations of NP or HCl concentration in each fluid sample.

The zeta-potential was also measured for some nanofluids with and without stabilizer, to evaluate whether the improved stability was caused by increased electrostatic repulsion. The zeta potential of nanofluids without acid ranged from -2 to -3.5 mV, while the addition of acid made the zeta-potential increase to values between -1 and 0.5 mV. This means that the electrostatic repulsion between the particles is actually lowered, and that the improved stability must be caused by some other mechanism.

		Size (d.nm):	% Intensity:	St Dev (d.nm):
Z-Average (d.nm): 108.6	Peak 1:	132.6	99.6	62.10
PdI: 0.182	Peak 2:	4897	0.3	670.7
Intercept: 0.938	Peak 3:	19.73	0.1	2.770
Result quality : Good				

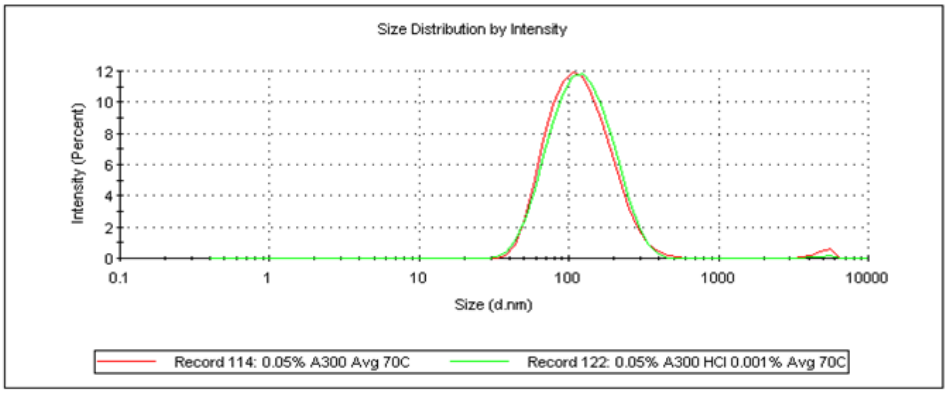

(a) Red: 0.05 wt% A300. Green: 0.05 wt% A300 + 0.001 wt% HCl

		Size (d.nm):	% Intensity:	St Dev (d.nm):
Z-Average (d.nm): 97.99	Peak 1:	119.7	100.0	58.78
PdI: 0.168	Peak 2:	0.000	0.0	0.000
Intercept: 0.929	Peak 3:	0.000	0.0	0.000
Result quality : Good				

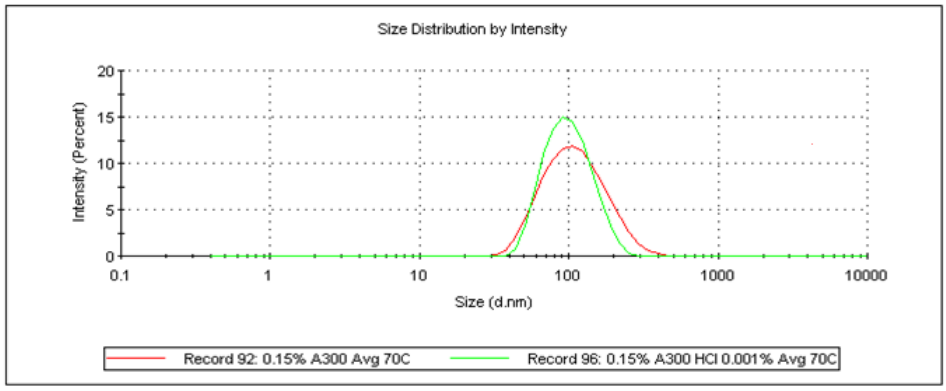

(b) Red: 0.15 wt% A300. Green: 0.15 wt% A300 + 0.001 wt% HCl

Figure 6.9: PSD of nanofluids at T=70^{o}C

		Size (d.nm):	% Intensity:	St Dev (d.nm):
Z-Average (d.nm): 194.7	Peak 1:	243.4	100.0	119.0
PdI: 0.184	Peak 2:	0.000	0.0	0.000
Intercept: 0.937	Peak 3:	0.000	0.0	0.000
Result quality : Good				

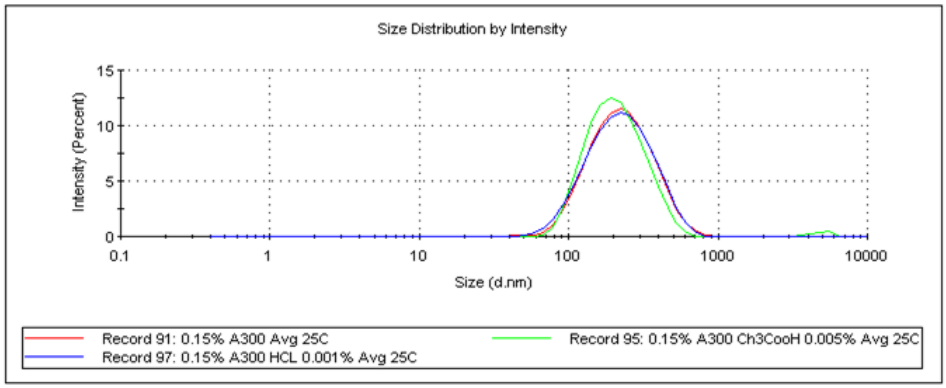

(a) Red: 0.15 wt% A300. Green: 0.15 wt% A300 + 0.005 wt% CH_3COOH. Blue: 0.15 wt% A300 + 0.001 wt% HCl

		Size (d.nm):	% Intensity:	St Dev (d.nm):
Z-Average (d.nm): 95.23	Peak 1:	103.8	98.3	37.60
PdI: 0.165	Peak 2:	4808	1.7	732.8
Intercept: 0.929	Peak 3:	0.000	0.0	0.000
Result quality : Good				

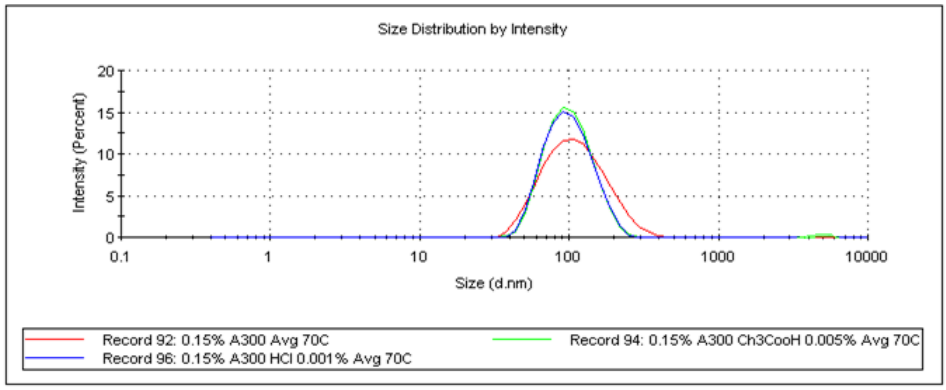

(b) Red: 0.15 wt% A300. Green: 0.15 wt% A300 + 0.005 wt% CH_3COOH. Blue: 0.15 wt% A300 + 0.001 wt% HCl

Figure 6.10: PSD of nanofluids at T = 25^{o}C and T = 70^{o}C

6.5 Core Flooding Process

As mentioned in the introduction of this chapter, twelve Berea sandstone cores (six high permeable and six low permeable) were chosen for the core flooding process. All the intermediate wet core samples were completely saturated with brine prior to the flooding experiments, making the flow single-phase. In order to minimize the presence of air bubbles in the system, all air bubbles in the lines of the flooding setup were removed by liquid displacement. One variable was changed with respect to the base case in the flooding experiments in order to investigate the influence of various factors on nanoparticle transport in sandstone. Ten of the core floods were performed with a unique set of variables, while two of the experiments were repeated for quality control. The transport of silica nanofluids with and without stabilizer was investigated in two permeabilities (high and low) and for two NP concentrations (0.05 wt% and 0.15 wt%). The details of each core flood is seen in Figure 6.11. The flooding procedure for each core sample had 3 stages:

- Pre-flush: 3-4 PVs of 3.8 % SSW injection to clean out any dirt/salts in the pores.
- Nanofluid injection: 4 PVs of nanofluid injection at a rate of q = 2 ml/min.
- Post-flush: 4-6 PVs of 3.8 % SSW injection to recover nanoparticles in the pores.

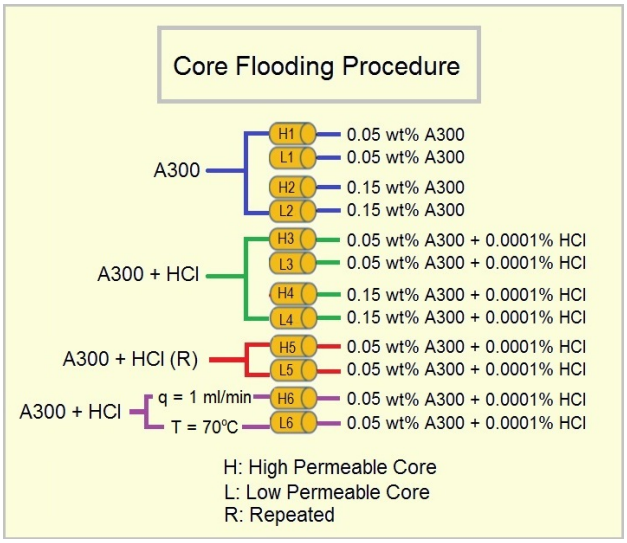

Figure 6.11: Core Flooding Procedure

6.5.1 Tracer Flooding

In order to estimate adsorption and desorption of nanofluids in core samples, ideal adsorption curves had to be established for reference. Adsorption curves in porous media correlate the *dimensionless concentration* (DC) of an injected substance to the number of injected PVs. The DC of a substance can be calculated with equation 5.4.

It is assumed that tracers have ideal adsorption curves inside core samples of sandstone, hence *20 ppm* solution of sodium iodide in SSW was used as tracer. Before the tracer could be injected into the core samples, a calibration curve had to be made between the light absorbency and the concentration of the tracer solution. A similar calibration curve was made for various concentrations of NP in SSW. The calibration curves for tracer and nanofluid are seen in Figure 6.12 and 6.13 respectively. Calibration data and absorbency readings are found in Appendix A.5. The tracer injection procedure followed the same steps as

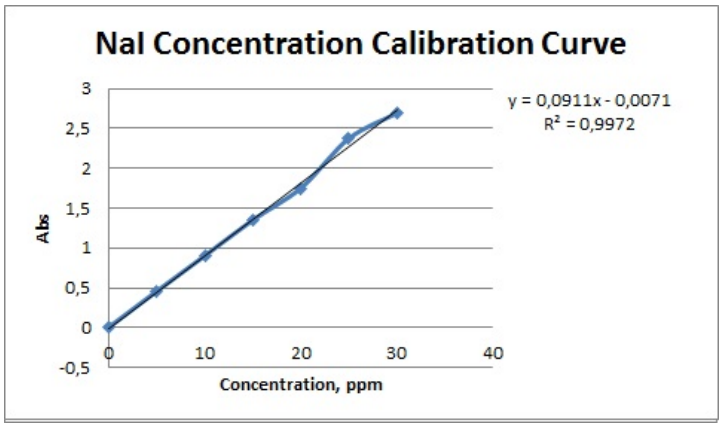

Figure 6.12: Tracer (NaI) concentration calibration curve

the nanofluid injection procedure, with pre-flush, injection and post-flush. Effluents were collected fore every ¼ PV, and the flow rate was kept constant at q = 2 ml/min during the whole flooding process. Due to time constraint, the adsorption curve was measured in four core samples, two high permeable and two low permeable respectively. The light absorbency was converted to effluent concentration with the calibration curve in Figure 6.12, before the DC was calculated with equation 5.4. The adsorption data was very consistent for all core samples, only showing a slight leftward shift in the low permeability adsorption curves. An average tracer curve was used as reference for the core flooding experiments with nanofluid injection. The tracer adsorption curves are seen in Figure 6.14, and the light absorbency data are found in Appendix A.5.

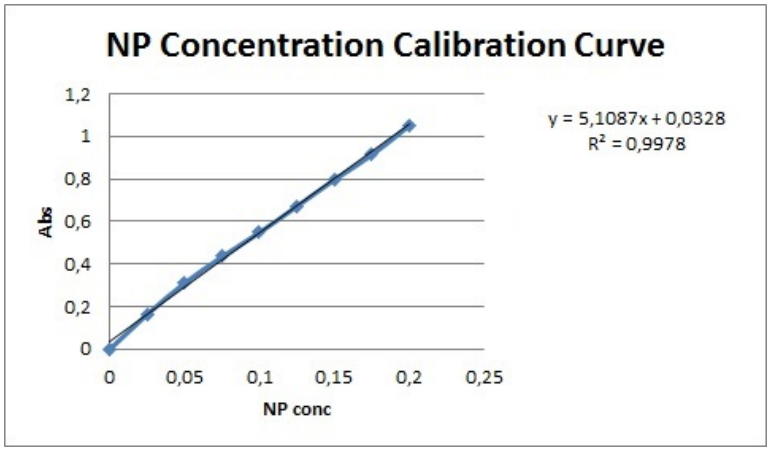

Figure 6.13: NP concentration calibration curve

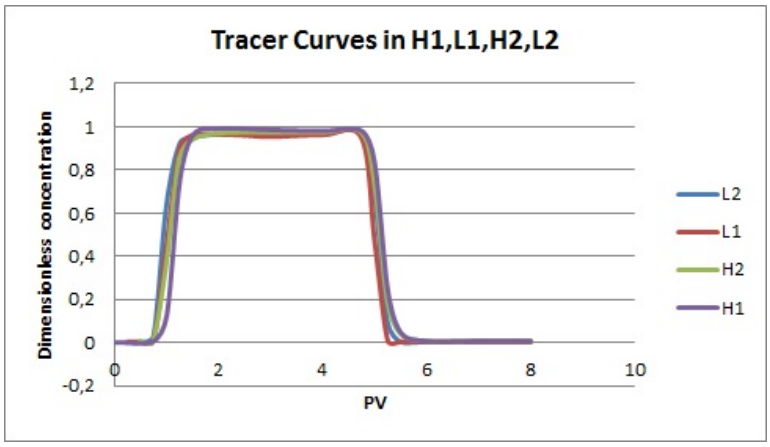

Figure 6.14: Tracer (NaI) curves in low and high permeable sandstone

6.5.2 Core Flooding Scenario #1: A300

Core sample H1 was the first to be injected with nanofluid. The core sample was placed in the core holder, and a sleeve pressure of approximately 20 bar was applied with nitrogen (N_2). The core was flushed with brine at a flow rate of q = 10 ml/min for 3 PVs to displace any residual NaI from the previous tracer flooding experiment. The rate was then lowered to q = 2 ml/min, before switching to accumulator B in the core flooding setup seen in Figure 5.3 to initiate the nanofluid injection. The pressure started increasing immediately when the 0.05 wt% nanofluid came in contact with the core, as seen from the differential pressure recording in Figure 6.15. The pressure increased modestly for 1.5 PV before in-

creasing exponentially until brine flooding was re-injected after 5 PVs of core flooding in total. The differential pressure rose slowly during post-flush with brine before stabilizing at a value of ΔP = 4.2 bar, resulting in an instantaneous permeability of K_{H1} = 6.94 mD. Over an interval of 4 PVs, the differential pressure had a 1 bar increase per PV on average, which is a clear indication of nanoparticle retention. The permeability impairment was calculated with as the ratio of instantaneous and initial permeability, yielding a relative reduction of 98.1 %. The data and calculations for permeability impairment are seen in Appendix A.5.

Core sample L1 was the second core to be flooded, with the same NP concentration as in the flooding of H1. The core was pre-flushed with SSW for 3PVs at a flow rate of q = 10 ml/min before being injected with nanofluid. The differential pressure increased rapidly and close to linearly during the first PV of injection, as seen in Figure 6.15. The curve had an approximate derivative of $\frac{dP}{d(PV)} = 3$ bar/PV. During the next three PVs of nanofluid injection, the differential pressure increased more moderately (still linearly) with an approximate derivative of $\frac{dP}{d(PV)} = 0.67$ bar/PV. The differential pressure over L1 stabilized at ΔP = 5 bar during post-flush with SSW, resulting in an instantaneous permeability of K_{L1} = 5.83 mD. The injection pump had to be refilled with synthetic oil after 7.3 PVs, which is seen from the steep decline of ΔP. Just as for core sample H1, there are clear indications of permeability impairments. The permeability of core L1 was 95.1 % reduced after post-flush, suggesting that the pores are almost completely blocked. Relevant data and calculations are found in Appendix A.5.

The NP concentration was increased to $C_{NP} = 0.15$ wt% for in the two following experiments. Core sample H2 was flooded with 4 PVs of brine as pre-flush at a constant flow rate of q = 2 ml/min, before being injected with the higher concentrated nanofluid. The differential pressure of H2 increased more rapidly than the pressures over H1 and L1. The end-point value during nanofluid injection was ΔP = 14.7 bar, which is approximately 3 and 3.5 times higher than the end-point values of cores L1 and H1 respectively. The differential pressure continued to rise after the post-flush was initiated, before suddenly dropping to value of ΔP = 6 bar. The pressure increased to an end-point value of ΔP = 7.5 bar in the post-flush sequence, which corresponds to an instantaneous permeability of K_{H2} = 3.88 mD. The permeability reduction of H2 was calculated to 98.8 % with the core sample's initial and instantaneous permeability data (Appendix A.5).

Core sample L2 was also pre-flushed with brine at a flow rate of q = 2 ml/min for 4 PVs, before being injected with nanofluid. The pressure drop increased linearly for the first 3 PVs with a similar derivative as H2, before it began to increase exponentially. The nanofluid injection sequence had to be aborted by initiating post-flush after 3.25 PVs, because the increasing pressure would eventually lead to equipment damage. The differential pressure fell immediately during post-flush, and had a fluctuating differential pressure with an average value of ΔP = 10.7 bar. The instantaneous permeability was estimated to K_{L2} = 2.72 mD, resulting in a permeability reduction of 98.5 %. However, the permeability impairment would most likely be higher if the nanofluid injection sequence had not been terminated pre-maturely. Thus, the formation damage data should not be compared to cases where nanofluid was injected for 4 PVs.

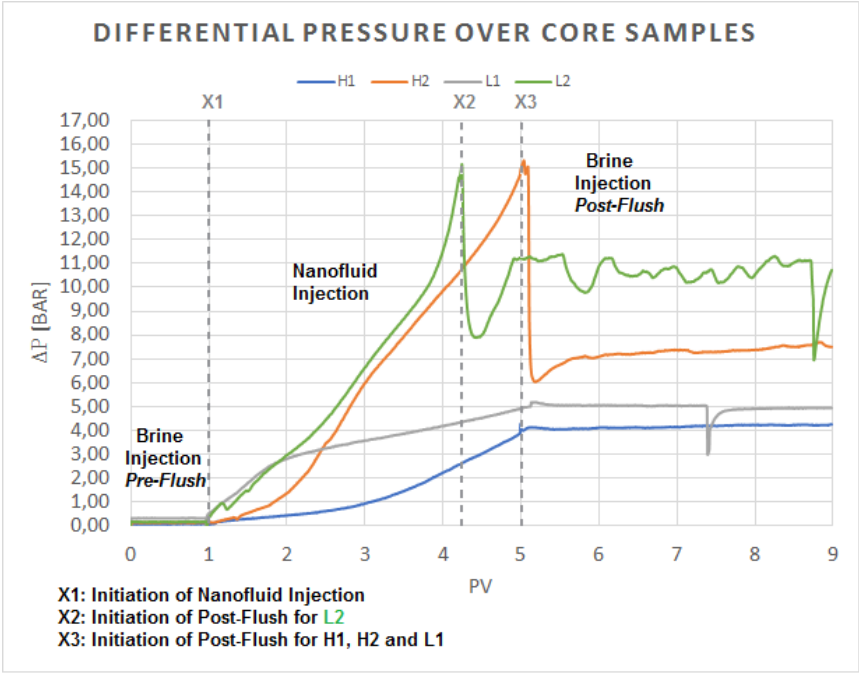

Figure 6.15: Differential pressure over Core Samples during A300 injection (base case)

The nanoparticle adsorption inside core samples H1, H2, L1 and L2 was estimated by measuring the light absorbency of the core flood effluents with the UV-Vis apparatus. Every ¼ PV of effluent was collected with test tubes during the nanofluid injection and post-flush sequences, and every ½ PV was measured with the UV-Vis on average. The measured light absorbency in the effluents was related to a NP concentration by the linear relation in

Figure 6.13, and then converted to dimensionless nanoparticle concentration with equation 5.4. As seen in Figure 6.16, the nanoparticle DCs were significantly lower than the reference tracer DC. This suggests a high degree of adsorption in the core samples, with L2 and H2 showing the highest adsorptions on average. The adsorption curve for core sample H1 had anomalous data which exceeded the the maximum value of DC (DC $\leq$ 1), and was therefore scaled down to 25 % to fit the NP adsorption curves in Figure 6.16. The errors in the measurement of adsorption in core H1 are too large to give any valuable information, and the curve is therefore excluded from the analysis. The adsorption curves of L1, L2 and H2 are displayed in Figure 6.17 for improved appraisal and analysis.

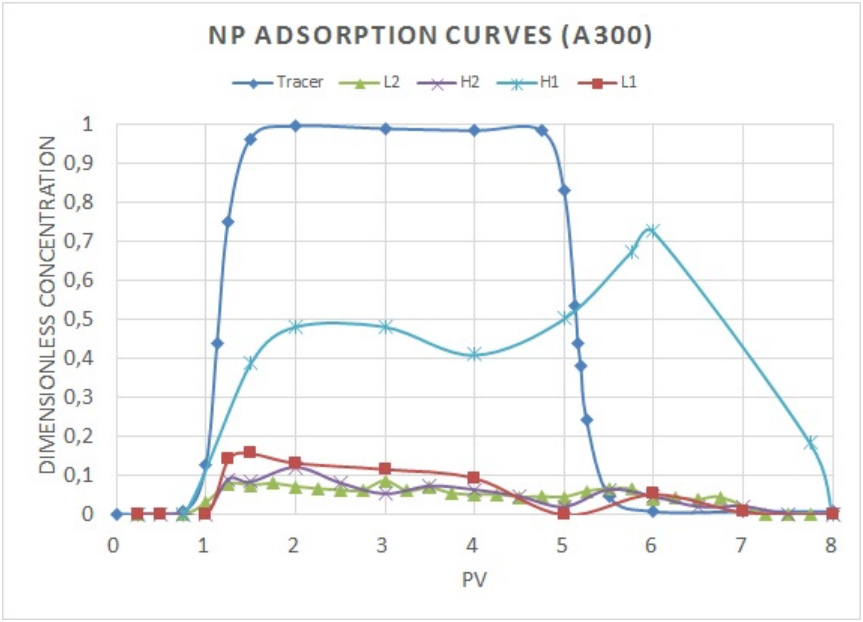

Figure 6.16: Adsorption of nanoparticles from A300 flooding (base case)

It is seen from Figure 6.17 that the DC of NP starts to increase after 1 PV of nanofluid injection for core L1, L2 and H2, which shows that NPs are present in the effluent after the nanofluids have travelled through the cores. The phase shift of the adsorption curves with respect to the tracer curve indicates that particles are retained, and the differential pressure response to the immediate adsorptions can be seen after 1 PV of nanofluid injection in Figure 6.15. The adsorption curves in cores L1, H2 and L3 increase rapidly during first PVs of injection, before decreasing steadily to a value of zero close to the end of the post-flush sequence. The average DC in cores L2 and H2 is $DC_{NP} \approx 0.06$, which implies that 94 % of the injected nanoparticles are adsorbed during flooding. The average DC in core

sample L1 is $DC_{NP} \approx 0.08$, which means that 92 % of the nanoparticles are adsorbed. The DC of NPs in core L1 is almost twice as high as in cores H2 and L2 over the interval of 1-4 PVs of injection, which explains the comparably lower pressure gradient seen after 1 PV of injection in Figure 6.15. According to Figure 6.17, NP desorption occurs in all core samples during the post-flush sequence. This is seen after 5.5 PVs of total injection (1.5 PVs of post-flush), when the adsorption curves are no longer confined by the tracer curve's boundary.

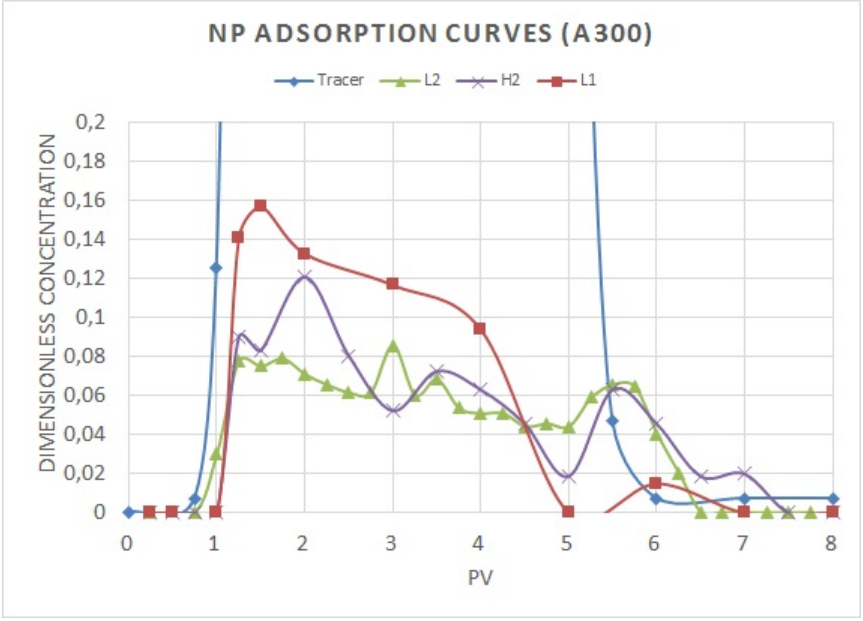

Figure 6.17: Zoomed display of adsorption curves from cores L1, H2, L2

6.5.3 Core Flooding Scenario #2: A300 + HCl

Core samples H3, H4, L3 and L4 were injected with with nanofluids containing HCl, as a means to reduce permeability damage and excessive NP adsorption. All the nanofluids used for injection had a HCl concentration of 0.001 wt%, since was the maximum concentration to satisfy the pH requirement. Core H3 was flooded first, with a NP concentration of 0.05 wt%. The core sample was pre-flushed with 4 PVs of SSW as at q = 2 ml/min before the nanofluid injection sequence was initiated. The differential pressure increased in a linear fashion during injection, and reached a plateau value of ΔP = 1.87 bar when post-flushing with SSW was initiated. The post-flush was terminated after 7 PVs of in-

jection because the accumulator ran out of SSW. The core sample rested inside the core holder for about 30 minutes before flooding was continued, and the pressure leveled at ΔP = 2.3. However, based on the pressure behavior in previous floods it is assumed that the plateau value would have remained constant if there was no interruption of the experiment. Thus, the first plateau value was considered when estimating the permeability impairment of H3. The liquid permeability was reduced by 95.4 %, to an instantaneous permeability of K_{H3} = 15.6 mD (see table A.8 in Appendix A.5).

Core L3 was pre-flushed at a flow rate of q = 3 ml/min, before nanofluid injection was initiated at a flow rate of q = 2 ml/min. The pressure increased with a steep gradient for the first 2 PVs during nanofluid injection, and then more slowly for the last 2 PVs. The pressure drop reached a peak value of ΔP = 6 bar when post-flush was initiated, followed by a steady (linear) decline to ΔP = 5.7 bar after 9 PVs of total injection. The pressure decline was believed to be an indication of nanoparticle desorption, hence the end-point value was used for the estimation of instantaneous permeability and formation damage. A value of K_L3 = 5.10 mD was estimated with Darcy's law, resulting in a permeability reduction of 97.0 %. See Appendix A.5 for details.

Core sample H4 was injected with SSW at a flow rate of q = 2 ml/min, followed by nanofluid injection. The differential pressure increased moderately for the first 2 PVs, before increasing with a gradient of $\frac{dP}{d(PV)} \approx 6$ bar/PV. After 4 PVs of injection, the peak value of ΔP = 14 bar was reached and the pressure dropped due to the starting post-flush with SSW. The differential pressure continued to rise during the post-flush sequence, and had an endpoint-value of ΔP = 10.31 bar. The instantaneous permeability and formation damage were estimated to K_{H4} = 2.83 mD and 99.2 % respectively, which is registered as the most severe case of permeability impairment so far.

Core L4 was pre-flushed with SSW at a flow rate of q = 3 ml/min. The flow rate was then lowered to q = 2 ml/min, followed by nanofluid injection. The nanofluid injection sequence was purposely terminated after 3.25 PVs, for comparison with core sample L2 in Figure 6.20. The pressure drop across the core increased steadily to a peak value of ΔP = 9.5 bar after 3.25 PVs of nanofluid injection, before SSW was injected. The pressure increased slightly before falling and stabilizing at a constant ΔP = 8.7 bar. The instantaneous permeability and formation damage were estimated to K_{L4} = 3.35 mD and 97.6 %, respectively. The permeability impairment data cannot be compared to cases where 4

PVs of nanofluid were injected, but the data is compatible with core L2. A comparison of the differential pressures from flooding scenarios #1 and #2 are shown in Figures 6.19 and 6.20, for low and high NP concentration respectively.

The permeability impairment data in table A.8 of Appendix A.5 shows the instantaneous permeability and relative permeability formation damage of core samples in the A300+HCl and A300 cases. The permeability impairment in cores H3 and L4 is 3% and 1% lower than in cores H1 and L2 respectively, which could suggest that HCl has a positive effect on permeability damage. However, the permeability impairment in cores H4 and L3 is 0.4% and 2% higher than for cores H2 and L1, which suggests the opposite. Thus, additional core floods at the same conditions were conducted for quality control, and can be seen in subsection 6.5.4 of this chapter.

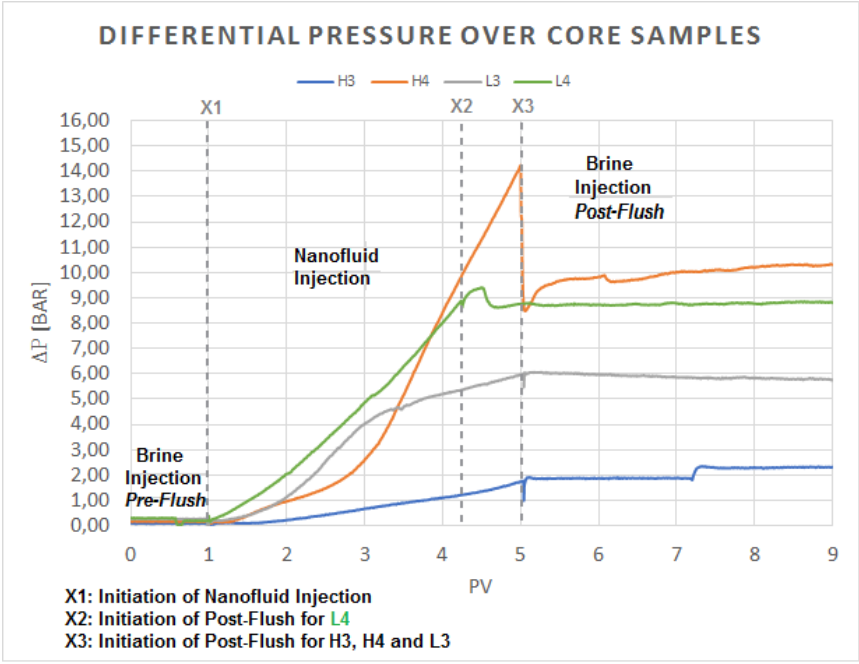

Figure 6.18: Differential pressure over Core Samples during A300 + HCl injection

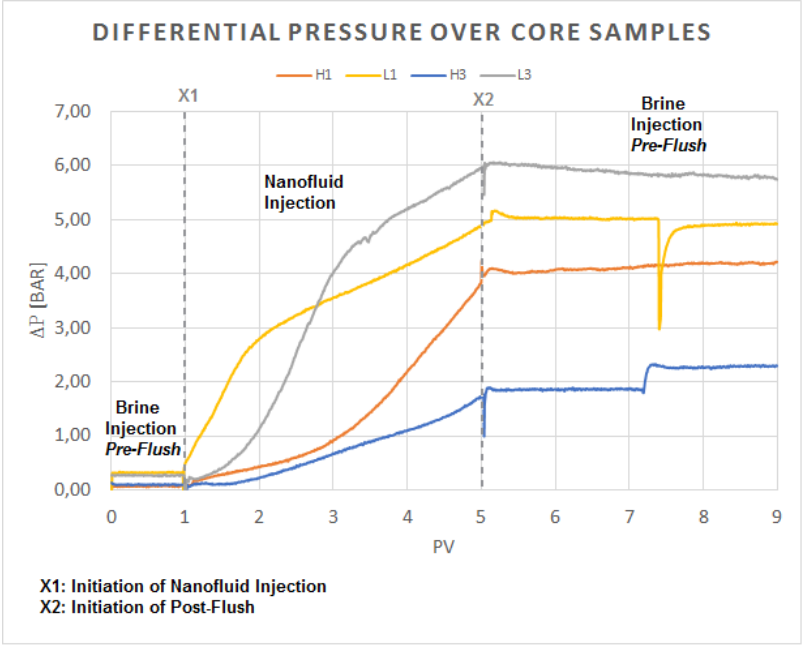

Figure 6.19: Differential pressure over core samples. 0.05 wt% nanofluid

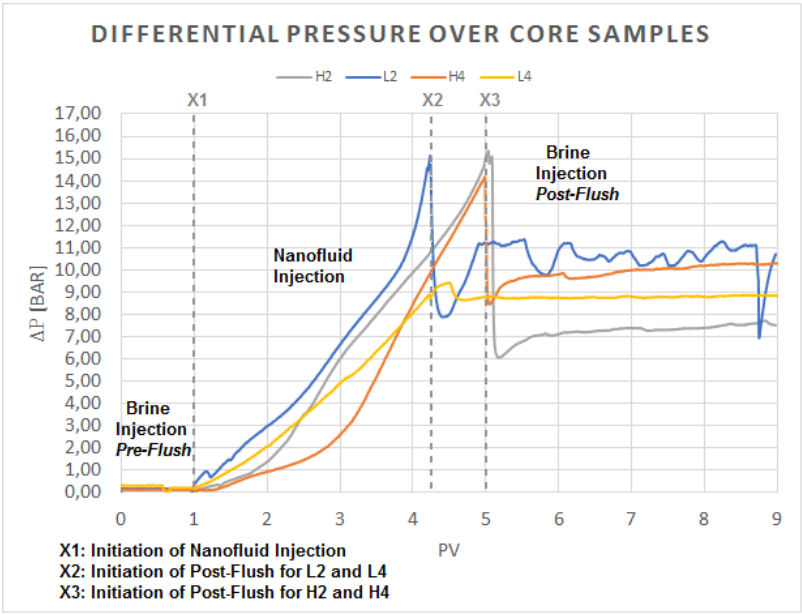

Figure 6.20: Differential pressure over core samples. 0.15 wt% nanofluid

The adsorption of nanoparticles in cores H3, H4, L3 and L4 was measured after the A300+HCl flooding scenario was conducted. The light absorbency was measured for every ½ PV from the respective core floods, resulting in the adsorption curves seen in Figure 6.21. The DC of nanoparticles in the effluent is low for all cores, suggesting an average NP adsorption of 82%, 84%, 95% and 91% for cores H3, L3, H4 and L4 respectively. A comparison between the curves in Figure 6.17 shows that the adsorption when flooded with A300+HCl is reduced in all cores except H4, which had the most severe case of permeability impairment (99.2 %). The adsorption curves from A300+HCl flooding are shown in Figure 6.21, and a closer display is shown in Figure 6.22 for improved appraisal and analysis.

The adsorption in cores H3 and H4 is lower than in cores L3 and L4 in the beginning, seen by the closer tracing of the ideal adsorption curve in cores H3 and H4. The pressure response due to the difference of early adsorption can be seen in Figure 6.18, where the gradients of H3 and H4 are initially lower than those of L3 and L4, respectively. The DC in core sample H4 is surpassed by the DC in core sample L4 after 2 PVs of nanofluid injection, and the lower adsorption in core sample L4 persists from 2 to 6 PVs of nanofluid injection. The lower adsorption leads to a lower absolute permeability impairment after approximately 4 PVs of nanofluid injection, seen by the intersection of the differential pressure curves in Figure 6.20.

Figure 6.22 shows that the NP adsorption in core sample H3 is lower than in the other cores on average during nanofluid injection, which is confirmed by the comparably low differential pressure seen in Figure 6.18.

The increasing DC of core sample L3 throughout the nanofluid injection sequence indicates that the adsorption decreases, which agrees with the shape of differential pressure curve over core sample L3 in Figure 6.18. The adsorption curve of L3 forms two plateaus with an average DC of 37 % on the second plateau, which is more than twice the value of the first plateau. The rapid increase of DC had a positive effect on the pressure gradient as seen in Figure 6.19 after 3 PVs of injection. According to Figure 6.22, some NP desorption occurs after 5.5 PVs of total injection according. The desorption of L3 is higher than in cores H3, H4 and L4, which could explain the 5 % decrease in differential pressure seen during post-flush in Figure 6.19.

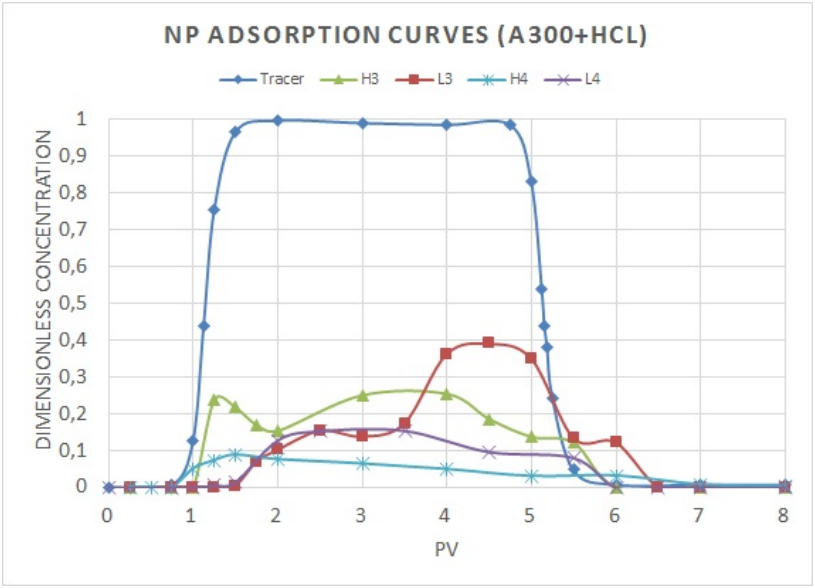

Figure 6.21: Adsorption of nanoparticles from A300+HCl flooding

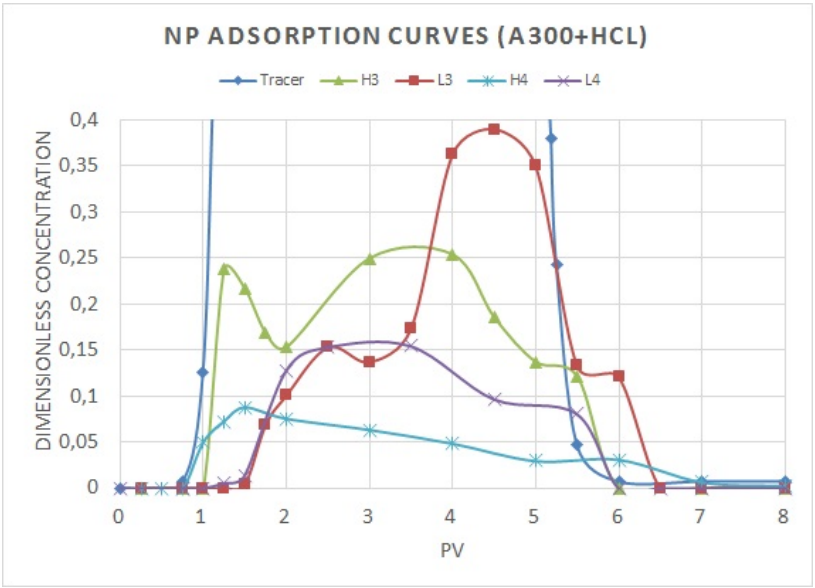

Figure 6.22: Zoomed display of adsorption curves from A300+HCl flooding

6.5.4 Core Flooding Scenario #3: A300 + HCl (R)

The core flooding data from the A300 (base case) and the A300+HCl flooding scenarios did not provide strong evidence of suspension stability enhancement with HCl, due to inconsistency in the results. Thus, further investigation was made to examine the differences between the successful and the unsuccessful core floods.

Accumulator tanks were used for injection in all core floods, with one full tank of A300/A300+HCl for nanofluid injection in two core samples. The core samples which indicated a reduction in formation damage by suspension stabilization (H3 and L4) were injected with half-empty accumulator tanks, it was suggested that a concentration gradient of HCl in nanofluid could exist. The pH of A300+HCl in the initial beaker and the residual accumulator was compared, but showed no difference of pH-value. Two additional core floods were conducted for the purpose of quality control with the same set of variables as in the flooding of cores H3 and L3, respectively.

Core sample H5 was the first to be flooded, with a NP concentration of 0.05 wt% and a HCl concentration of 0.001 wt%. The core sample was pre-flushed with SSW at a flow rate of q_{SSW} = 3 ml/min before nanofluid injection was initiated with a reduced flow rate of q = 2 ml/min. The pressure drop remained constant at ΔP = 0.13 bar during the first PV of injection, which was similar to the recorded pressure drop during brine flooding (see Appendix A.3). As seen in Figure 6.23, the differential pressure increased linearly from 1-4 PVs of nanofluid injection (2-5 PVs in the Figure), with a gradient of $\frac{dP}{d(PV)} = 0.4$ bar/PV. When post-flush was initiated, the differential pressure decreased moderately and stabilized at ΔP = 1.1 bar. The instantaneous permeability and formation damage were estimated to K_{H5} = 26.8 mD and 92.0 %, respectively. Relevant permeability data is presented in table A.8 of Appendix A.5.

The flooding of core sample L5 was a repetition of the L3 core flood, hence a nanofluid with NP concentration of 0.05 wt% and HCl concentration of 0.001 wt%. The core sample was pre-flushed for 4 PVs with a flow rate of q_{SSW} = 3 ml/min, before the flow rate was lowered and the nanofluid injection was initiated. After lowering the flow rate to q_{SSW} = 2 ml/min a pressure drop of ΔP = 0.21 bar was recorded across the core, and stayed constant until 0.4 PVs of nanofluid was injected. The differential pressure then started to increase in a linear fashion until SSW injection was initiated at PV = 5, as seen in Figure 6.23. The pressure gradient was estimated to $\frac{dP}{d(PV)} = 0.5$ bar/PV, which was expected

considering the the low permeability of core L5 compared to H5. The differential pressure stabilized at ΔP = 1.8 bar during post-flush, which suggested a significant improvement of formation damage compared to core sample L3. The nanofluid injection in core sample L5 resulted in an instantaneous permeability of K_{L5} = 15.9 mD and permeability impairment of 89.1 %. This was the lowest estimated permeability impairment in all core samples, as seen from the data in table A.8 of Appendix A.5. The relative formation damage in table A.8 shows that the permeability of cores H5 and L5 is 6% reduced with respect to the base case (H1 and L1), which again indicates that HCl may have a positive effect on formation damage. The discrepancy of the results will be discussed in chapter 7.

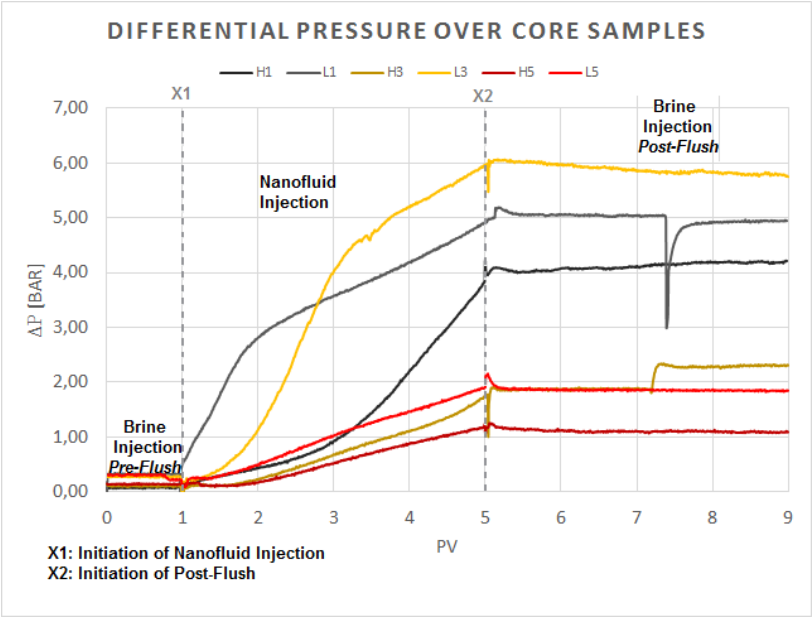

Figure 6.23: Differential pressure over core samples during nanofluid flooding with Low (0.05 wt%) Concentration

Figure 6.24 shows the adsorption curves in core samples H5 and L5, with the adsorption data of H3 and L3 included for reference. Figure 6.25 presents a zoomed display of the same curves. The curves indicate reduced adsorption in the repeated core flooding experiments, with average adsorptions of 67 % and 77 % of cores H5 and L5, respectively. Core sample H3 and L3 had average NP adsorptions of 82 % and 84 %, respectively.

The DC in core sample H5 traced the ideal adsorption curve well in the beginning, but started to deviate after 1.25 PVs of nanofluid injection. At the same time, the differential pressure began to increase slowly as seen in Figure 6.23. The overall high DC in core

sample H5 is in accordance to the restricted differential pressure build-up seen in Figure 6.23. The DC in core sample L5 deviates slightly from the ideal tracer curve in the beginning, which indicates NP adsorption. The early adsorption does not seem to impair the permeability significantly, as seen be the low differential pressure over core L5 in Figure 6.23. The overall lower adsorption of NPs in H5 and L5 compared to H3 and L3 is consistent with the reduced differential pressures over the cores. By comparing the adsorption in cores H3, L3, H5 and L5 to cores H1 and L1, it is evident that HCl has a positive effect on the adsorption.

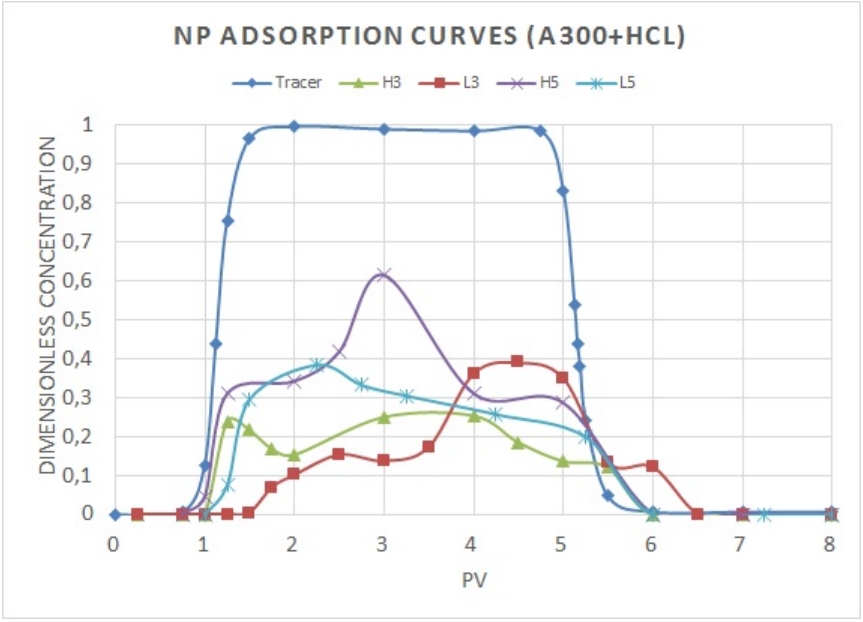

Figure 6.24: Adsorption of nanoparticles from A300+HCl (R) flooding

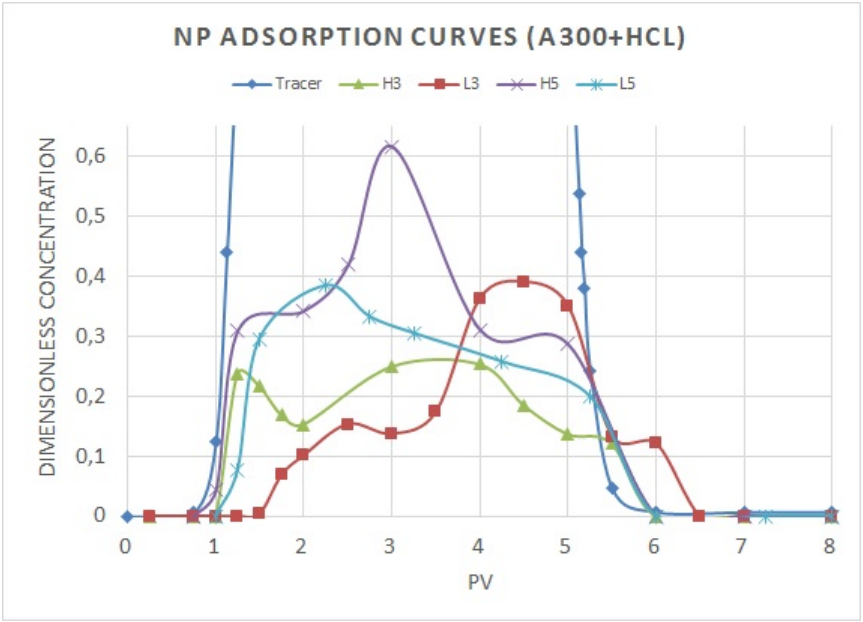

Figure 6.25: Zoomed display of adsorption curves from A300+HCl (R) flooding

6.5.5 Core Flooding Scenario #4: Other

The effects of lowering the nanofluid flow rate and increasing the temperature were investigated in low and high permeable core samples, respectively. The NP and HCl concentrations were kept at C_{NP} = 0.05 wt% and C_{HCl} = 0.001 wt% for optimum nanofluid design in terms of colloidal stability.

Core sample L6 was the first to be flooded, and was pre-flushed with 4PVs of SSW at a flow rate of q_{SSW} = 10 ml/min. The flow rate was then lowered to q_{SSW} = 1 ml/min for 1 PV before nanofluid injection in order to prevent increased aggregation from turbulent flow. When nanofluid injection was initiated, the pressure drop remained close to constant for 0.2 PVs before showing a moderate and linear increase of $\frac{dP}{d(PV)} \approx 2$ bar/PV. As seen in Figure 6.26 the pressure gradient decreased to $\frac{dP}{d(PV)} \approx 0.5$ bar/PV after 1 PV of injection, which is similar to the pressure behavior seen in core L1. After initiation of post-flush at PV = 5, the pressure drop remained constant at ΔP = 3.4 bar. The instantaneous permeability and formation damage were estimated to K_{L6} = 4.3 mD and 97.3 %, respectively, as presented in table A.8 of Appendix A.5.

Core sample H6 was inserted into the high temperature core flooding system shown in Figure B.6 in Appendix B, and the temperature was elevated to T = 70^{o}C over a period of 20 hours. SSW was injected at q_{SSW} = 1 ml/min during the temperature elevation process, and sleeve and back pressures of respectively 40 bar and 10 bar were applied during the process. Nanofluid was injected at q = 1 ml/min in the high temperature flooding to imitate sub-surface conditions as much as possible with respect to time constraint.

The pressure drop increased immediately after nanofluid injection, with an average increase of $\frac{dP}{d(PV)} = 3$ bar/PV during the first PV of injection. As seen in Figure 6.26, the differential pressure began to increase exponentially after 2 PVs of total injection. The core flood had to be terminated after 1.5 PVs of nanofluid injection (PV = 2.5) because the pressure gradient approached infinity, indicating complete pore blockage and hence formation damage of 100 %. Figure 6.26 shows that the differential pressure during high temperature flooding is comparable to flooding in room temperature initially, but the effective aggregation of the nanoparticles at high temperature soon causes pore blockage which leads to an exponentially increasing pressure.

The surface appearance of cores H1, H5 and H6 after nanofluid injection is shown in Figure 6.27, where the effect of high temperature flooding is clearly visible.

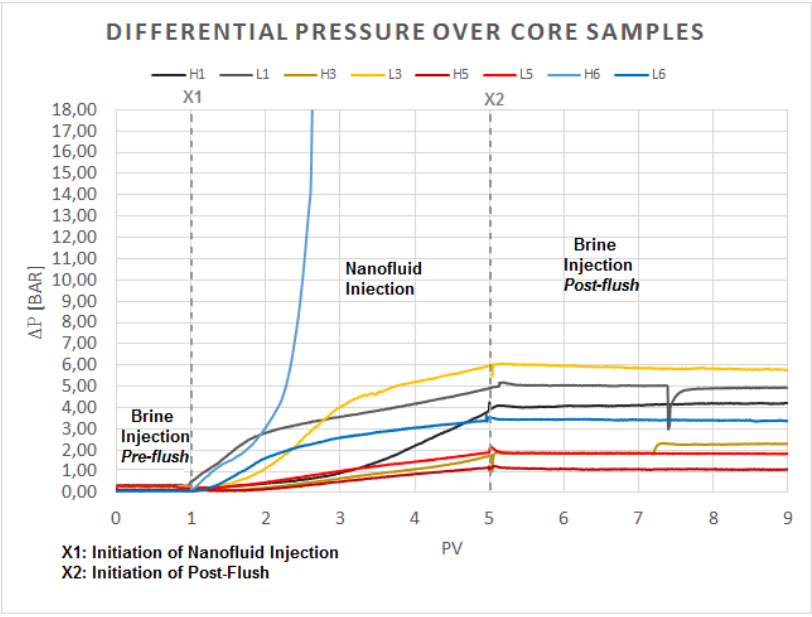

Figure 6.26: Differential pressure over core samples during nanofluid flooding with Low (0.05 wt%) Concentration

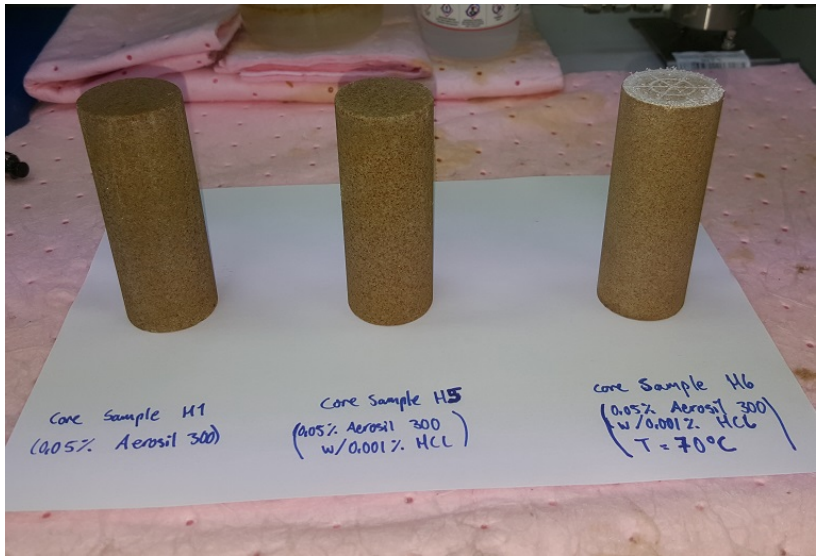

Figure 6.27: Surface appearance of core samples H1, H5 and H6 after nanofluid injection

The adsorption of NPs in core samples H6 and L6 were measured after the core flooding process, and the adsorption curves with regular and close view are presented in Figures 6.28 and 6.29 respectively. The adsorption curves of cores H3 and L3 are included for reference, since the adsorption data of core H1 was unreliable.

Since the injection of core sample H6 had to be aborted after 2 PVs of nanofluid injection, its adsorption curve is incomplete. However, 1.75 PVs of additional effluent (3.75 in total) was produced and collected due to the reduction of back pressure in the core flooding setup. As seen in Figure 6.29, core sample H6 has the characteristic declining adsorption curve as seen in some of the other previously injected cores. The DC of H6 starts to deviate from the ideal adsorption curve after 1 PV of injection, which is when the differential pressure starts to increase exponentially as seen in Figure 6.26.

The DC in core L6 follows the tracer curve during the first ¼ PV of effluent, which agrees with the low pressure drop recorded right after nanofluid injection in Figure 6.26. The late peak of DC in core sample L3 does not occur in core sample L6, as seen in Figure 6.29. It was believed that this peak could be related to the sudden reduction of pressure gradient seen in all low permeable core samples except L5, but the declining adsorption curves in cores L1 and L6 reject this theory.

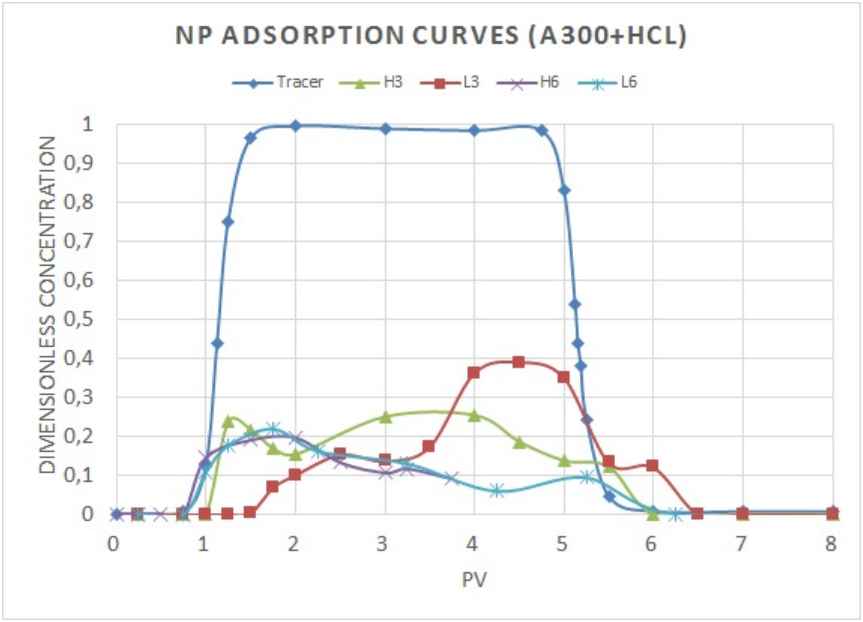

Figure 6.28: Adsorption of nanoparticles from A300+HCl flooding at various q and T

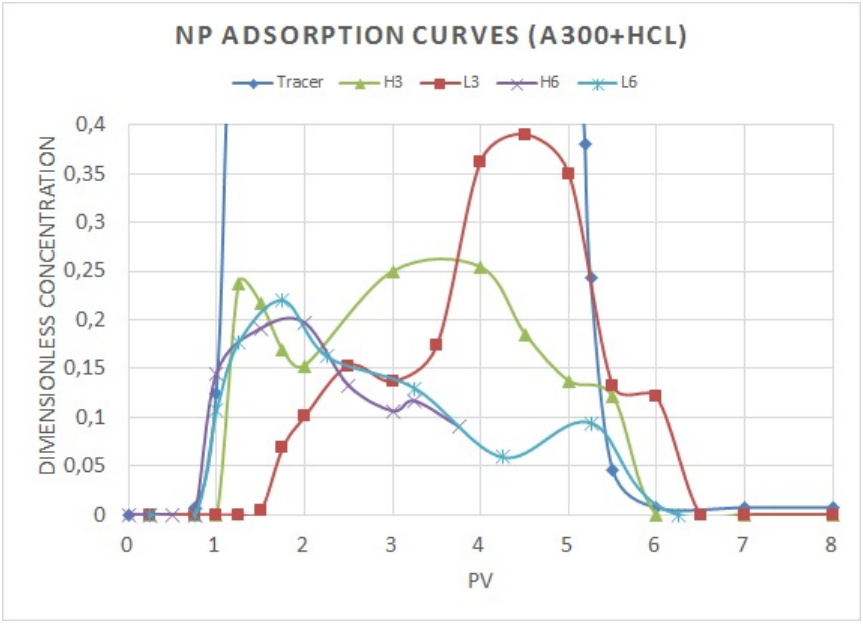

Figure 6.29: Zoomed display of adsorption curves from A300+HCl flooding

6.5.6 SEM-analysis

The nanoparticle adsorption was analyzed with a scanning electron microscope (SEM) in one of the core samples (L2) to see the forming structure of nanoparticles on the rock surface. Core sample L2 was considered appropriate for the analysis, because it was injected with highly concentrated nanofluid and because this core experienced the highest formation damage. The core sample was crushed for the analysis, and SEM images of the internal rock surfaces are shown in Figure 6.30. The small fragments seen on the sand grains in Figure 6.30c are nanoparticles, which proves that adsorption has occurred. The analysis also showed that the surface coverage of nanoparticles in the sandstone was incomplete, as seen in Figure 6.30d.

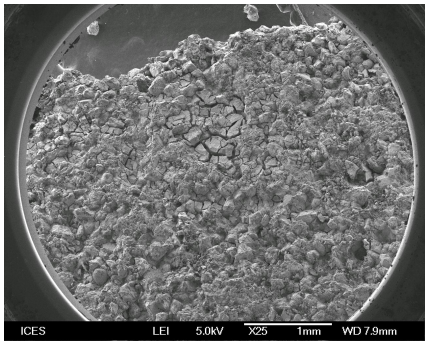

(a) SEM-image of sand grains at x25 magnitude

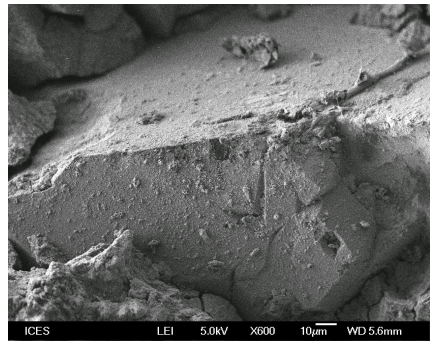

(b) SEM-image of core surface with x600 magnitude

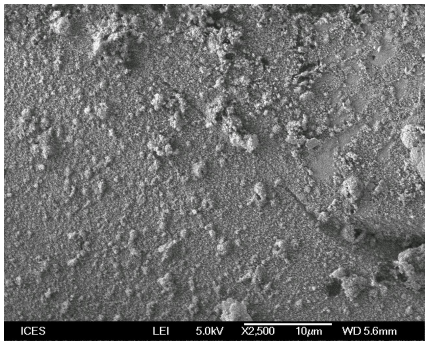

(c) SEM-image of core surface with x2500 magnitude

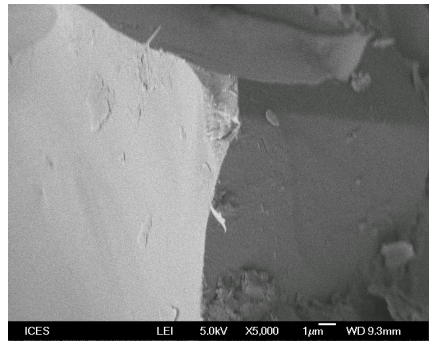

(d) SEM-image of unflooded quartz with x5000 magnitude

Figure 6.30: SEM-images of core sample L2

7 Discussion

7.1 Literature Review

Nanoparticles have many beneficial applications due to their large surface area, and altered characteristics compared to their bulk materials. The application of nanotechnology can benefit the upstream sector of the petroleum industry in areas such as: enhanced drilling stability, increased accuracy in hydrocarbon exploration and EOR. The use of nanoparticles for EOR is especially promising, as some of them (nanosilica) are environmentally friendly while still producing a significant amount of incremental oil. Compared to other chemicals used for EOR, silica nanoparticles are cheap and can be modified (e.g. polymer coating) to handle harsh reservoir environment with high salinity and temperature.

The majority of the published research on nanoparticles for EOR uses monovalent brine as dispersant, and the experiments are conducted in room temperature. As shown by Metin et al. (2011), sub-surface conditions and divalent brine heavily degrade the stability of silica nanoparticle suspensions. Thus, further investigation and improvement of nanoparticle propagation and EOR potential at sub-surface conditions must be conducted before large field applications can be carried out.

7.2 Ageing of Core Samples

The increased mass of the core samples after aging with SurfaSil was not uniform in neither the high or the low permeable core samples. The variations within each permeability group were not considered, but suggests that the wettability was not altered equally for all core samples. In hindsight, this could have been investigated by using the empirical equations 4.5 and 4.6, presented by Ju et al. (2002), to estimate the surface coverage of SurfaSil in each core sample. The adsorbed volume could be obtained by density conversion of the

adsorbed mass SurfaSil.

The average mass adsorption in test cores (T1 and T2) and in the other nine high permeable core samples is consistent. This indicates that SurfaSil adsorption is rather spontaneous, and that complete adsorption was achieved after 4 hours of saturation. Due to consistency, the nine high permeable cores are assumed to be intermediate wet despite being aged for a shorter period of time. The low permeable cores are also assumed to be intermediate wet, since the cores were submerged in the same solution and for an equal amount of time as the high permeable cores. The permeability of a rock is an increasing function of porosity and grain size (Torsæter and Abtahi, 2003), suggesting that low permeable core samples have a lower porosity and smaller grain sizes (i.e. smaller pores) than high permeable rocks. The smaller pores could explain the lower adsorption of SurfaSil, since the surface area of a pore throat depends on its volume.

7.3 Porosity Measurement

The porosities of the core samples, separated by permeability, are consistent. During the vacuum saturation, the pressure in the exicator was reduced to zero millibar, which allowed the SSW to occupy the interconnected pores completely when introduced. Since cores H8 and H9 were not completely submerged in SSW after some hours of saturation, they did not achieve the same mass increase as the other cores. It was believed that air got trapped in the pores when the core samples were exposed to air, since further saturation with SSW did not increase the mass of the cores. High pressure flooding recovered full saturation of H8. It was believed that the MMP of air was surpassed, causing the air to be transported out with the injected SSW.

7.4 Permeability Measurement

The core samples were initially predicted to be high or low permeable, based on the appearance of the cross-sectional area of the cores. A coarse surface indicated that the sand grains were large, which again is related to high permeability. The opposite applies for low permeable formations. The permeability data presented in Figure 6.3, confirms the visual prediction and shows that the low permeable cores are less than half as permeable as the high permeable core samples on average.

It is seen from Figure 6.3 that the permeability estimation of core sample H6 is significantly lower than for the other high permeable cores. Core sample H6 was flooded

with SSW in the setup seen in Appendix B.2, since the whole core flooding experiment was conducted at high temperature (T = 70^{o}C). Kestin et al. (1981) studied the viscosity of NaCl solutions at various temperatures, and found that the viscosity may decrease up to 50 % when the solution temperature is increased to 70^{o}C from room temperature. This was not considered when the permeability was estimated, and according to equation 5.2 this leads to an overestimated permeability. This would suggest that core sample H6 in fact was low permeable, which contradicts the porosity and SurfaSil adsorption data in Figures 6.2 and 6.1 respectively. However, when saltwater comes in contact with Berea sandstone during flooding, the clay between the quartz may swell up which causes the *effective size* of the sandstone pores to decrease. This will lead to an increased differential pressure across the core to, which results in an underestimated permeability by equation 5.2. According to Hansen et al. (2012), the repetition distance between clay layers increase from 1.5 nm to almost 18 nm when the temperature is increased from 300K (27^{o}C) to 350K (77^{o}C). By assuming that core sample H6 is high permeable, it can be concluded that the underestimation of the permeability due to clay swelling dominates the overestimation due to a decrease in SSW viscosity.

7.5 Preparation and Stability of Nanofluids

Ultra-sonication of the nanofluids after synthesis provided good suspension stability for a short period, but the particles began to destabilize after 4-7 days when dispersed in 3.8 wt% SSW with divalent ions. The destabilization time of these nanofluids are much shorter than for typical silica nanoparticles dispersed in 3 % NaCl solutions, proving that the presence of divalent ions increases the nanoparticle aggregation significantly. Based on visual analysis, the addition of HCl and CH_3COOH to the nanofluids restrict nanoparticle aggregation significantly and delay the suspension destabilization. The comparison of suspensions with and without HCl as stabilizer in Figure 6.7 shows that the nanofluid stability is improved, but the suspensions destabilize within 28 days of synthesis. This suggests that more acid should have been added for further stability improvement, but this would unfortunately have breached the pH requirement of the core flooding setup. In the study by Ortega et al. (2016), more than twice the amount of HCl was used to stabilize the nanofluids at sub-surface conditions. Thus, it is still believed that silica nanoparticle suspensions can be stabilized if the correct amount of HCl is added.

The PSDs of the nanofluids in Figures 6.8, 6.9 and 6.10 indicate overall good dispersibility, seen by the smooth curves. Figure 6.9 shows that the size distributions are shifted to the left in all nanofluids when the temperature is increased to 70^o. This results in an average detected particle size of $Z_{avg} \approx 100$ nm at high temperature, which is half of what is detected at 25^oC. The deviation in particle size is believed to be caused by wrong input parameters for high temperature measurement, and not enhancement of colloidal stability as it would contradict the DLVO theory.

The presence of micron sized particles in the 0.05 wt% nanofluid without stabilizer indicates that some of the nanoparticles had agglomerated, and the amount of agglomerate increased when the temperature was elevated to T = 70^oC. This is consistent with the DLVO theory of colloidal stability. The PSDs of 0.05 wt% nanofluid with HCl demonstrate the stabilizer's efficiency at limiting particle aggregation at both low and high temperature. In fact, no agglomerate was detected in nanofluids with HCl, regardless of the solution's temperature. The PSDs of the 0.15 wt% nanofluids with and without HCl were almost identical at low temperature, but deviated when the temperature was elevated to T = 70^oC, as seen in Figure 6.9b. The PSD of the 0.15 wt% nanofluid without stabilizer increased with temperature, while the PSD of the nanofluid with HCl remained unchanged. The 0.05 wt% nanofluids with and without stabilizer in Figure 6.8b did not show any change of PSD with a changing temperature. This suggests that: 1): nanofluids with lower NP concentrations are more stable (at high temperature), and 2): particle growth at high temperature is limited when HCl is added to the suspension.

The PSDs in Figure 6.10 show that $CH3_3COOH$ has a negative effect on nanoparticle aggregation, despite having a smaller PSD than the other two nanofluids at low temperature (Figure 6.10a). The presence of micron sized particles in the nanofluid with $CH3_3COOH$ was surprising, since particles of this size were not detected in the nanofluid without stabilizer. It is believed that the DLS may have detected micron sized contaminants, since the secondary peak of the PSD did not increase with temperature as seen in Figure 6.10b. The addition of $CH3_3COOH$ in the nanofluid limited overall particle growth at high temperature, which is similar to the effect observed when adding HCl.

The PSD measurements in Figures 6.8, 6.9 and 6.10 should be repeated to make sure that the effects of increasing the temperature or adding HCl to the nanoparticle suspensions are not random. The effect of $CH3_3COOH$ on the suspension stability needs to be further investigated, since the results are inconsistent with the visual observations.

The zeta potential measurements showed that the nanoparticles were not stabilized by electrostatic repulsion when HCl was introduced to the suspension. Instead it is believed that the HCl interferes with the interaction between the nanoparticles and some of the divalent ions in the suspension (Ca^{2+} and Mg^{2+}), which makes the aggregation behavior more similar to the behavior in monovalent brine.

7.6 Core Flooding Process

The core flooding setup in Figure 5.3 was used for all core sample except for core H6, which was flooded in the high temperature setup seen in Figure B.6 of Appendix B.2. The sonication of fluids and evacuation of air in the tubes before injection made sure that no air was present in the system during flooding, which provided stable pressure recordings and supposedly laminar flow.

7.6.1 Tracer Flooding

The measurements of adsorption from tracer injection were very consistent, and gave close to ideal adsorption curves in all the four injected cores. The light absorbency data in Figure A.3 shows that the curves peak at the same wavelength (225 nm) in all measurements, suggesting that the light absorbency is measured for the same compound (NaI) in all cases. The measurement of NaI was isolated by using pre-flushed SSW as reference, as it was assumed that this liquid would have the same composition as the tracer effluent, except for NaI. The high consistency of the measurements confirmed this assumption.

7.6.2 Permeability Impairment

The permeability impairment of core samples injected with nanofluids was severe, with a minimum impairment of 89.1 % in core sample L5 and a maximum impairment of 100 % in core sample H6. The highest permeability impairment was generally seen in cores injected with 0.15 wt% nanofluid, which is consistent with the observations of Hendraningrat et al. (2013a) and Zhang et al. (2013). The low permeable cores yielded characteristic differential pressure curves when injected with 0.05 wt% nanofluid, as seen in Figure 6.26. In these core samples, the differential pressure increased rapidly for 1-2 PVs before the gradient decreased and the differential pressure started to increase more slowly until post-flush was initiated. The early rapid rise of differential pressure is believed to be caused by blockage of smaller pores, and the lower pressure gradient i.e. slower rate of blockage is

believed to be caused by nanoparticle adsorption inside the bigger pores.

The differential pressure over high permeable core samples injected with 0.05 wt% nanofluid did also have a characteristic appearance. The differential pressures were initially low and started to increase after approximately 0.5 PVs of nanofluid injection. Afterwards, the curves increased either exponentially or linearly until post-flush was initiated. The initially slow rise of differential pressure is believed to be caused by moderate adsorption of nanoparticles, while the exponential rise is believed to be caused by multi-layer adsorption. This phenomenon has been observed in intermediate wet sandstone previously (Li, 2015), and is in accordance with the theory of nanoparticle retention presented by Ju et al. (2002) in Chapter 4 of this thesis.

It is seen in Figure 6.20 that the differential pressure over cores injected with 0.15 wt% nanofluid drops when post-flush is initiated, which suggests that some of the nanoparticles responsible for the pore blockage are removed. The pulse which is created by the transition from nanofluid to SSW injection seems to mobilize the initially trapped nanoparticles at the inlet of the core, which causes the nanoparticles to be transported further into the core or even out of the core sample.

The differential pressure was lowered in most core samples flooded with 0.05 wt% nanofluid and 0.001 wt% HCl, and a reduction of up to 75 % of the post-flush pressure was seen for the most successful core floods in Figure 6.26. However, the post-flush differential pressures were usually more than one magnitude larger than the pressure drop during pre-flush, which always resulted in permeability impairments above 89 %. A higher HCl concentration could probably be more effective at reducing permeability impairment, but this was unfortunately considered acceptable for the core flooding setup in Figure B.5. The core flooding experiments of H5 and L5 resulted in a lower post-flush differential pressures and formation damage than in cores H3 and L3, despite being flooded under seemingly similar conditions. Since each pair of cores (H3/L3 and H5/L5) were flooded with **one** accumulator, it is believed that core samples H5 and L5 were actually exposed to a higher HCl concentration than H3 and L3. This is believed to be caused by errors of measurement when HCl was dispersed in nanofluid. For a HCl concentration of 0.001 wt%, only 0.4g of 1 wt% HCl solution is to be introduced in 400g of nanofluid. Such a small mass of HCl has a large relative uncertainty when measured on the laboratory scale, and even 10 % (0.04g) deviation may affect the core flooding experiment. This theory assumes that the formation damage decreases with an increasing concentration.

Figure 6.20 shows that the addition of HCl had little effect on both the pressure decrease and the permeability impairment. Since the nanofluids used in cores H2, H4, L2 and L4 had a NP concentration of 0.15 wt%, it is believed that the small addition of 0.001 wt% HCl was insufficient for the enhancement of the suspension stability. The visual stability analysis in Figure 6.7d confirms that the 0.15 wt% nanofluid could not be completely stabilized by the small addition of HCl.

The core samples in the study of Hendraningrat et al. (2013a) generally showed much lower impairment, but the injection volumes of nanofluid were also lower in most cases. The core sample which was injected with 3 PVs of nanofluid in the study showed a permeability impairment of 88 %, which is comparable to the least severe impairments (cores H5 and L5) in this study. This indicates that small amounts of HCl can be added to silica nanoparticles dispersed in SSW to counter the undesired effects of divalent ions on the suspension stability.

7.6.3 Adsorption Measurements

The information retrieved from the NP adsorption curves was in many cases in accordance with the differential pressures recorded over the core samples, but not always. Identical information from the two experiments is not expected, since the nanoparticles can adsorb in single-layers that do not affect fluid flow through the pores. This is believed to be the case in core sample L6, which has a significantly lower pressure drop than core sample H5 in the early phase of nanofluid injection, despite having quite similar adsorption curves. See Figures 6.26 and 6.29 for details. Despite the indications of single-layer adsorption, the overall high nanoparticle retention in the core samples of this study suggest that pore blockage will eventually occur. The increasing differential pressure as a result of increased NP retention confirms this theory, and the pressure response is often recorded 1 PV before the reduction of NP concentration is registered in the effluent. This phenomenon is observed when nanoparticles get trapped close to the core inlet, as the residual mobile nanoparticles at this position needs to travel through the whole core sample (1 PV) before the reduced NP concentration can be recorded in the effluent.

Several shapes of adsorption curves were observed in this study, with some having a characteristic appearance. Eight of the twelve core samples injected with nanofluid had declining adsorption curves which peaked after 1-2 PVs of injection and reached zero after approximately 6 PVs of total injection. Li (2015) measured similar curves when

investigating NP adsorption in intermediate wet sandstone, and stated that the decline in DC indicates "self-adsorption" of nanoparticles on the pore walls, i.e. the nanoparticles adhere to the pore surfaces in multiple layers. According to the adsorption curves in Figures 6.17, 6.22, 6.25 and 6.29, nanoparticle desorption was also evident in several core samples. However, the low resolution data from 5.5-6.5 PVs leads to high uncertainty, and it is therefore not safe to conclude that nanoparticle desorption occurred. In some core samples (H2, L2, L3 and H4) there were several data points that indicated nanoparticle desorption, which were in accordance with the recorded pressure drops in Figures 6.19 and 6.20. Thus, desorption can be concluded with a higher certainty in these cases.

The results from the NP adsorption measurements were surprising, as there was no obvious correlation between the set of the variables in a core flood and the resulting shape of the core sample's NP adsorption curve. However, total nanoparticle adsorption proved to be dependent of the NP concentration in the nanofluid, with lower adsorption in cores injected with 0.05 wt% nanofluid than those injected with 0.15 wt% nanofluid. According to Sheng (2011), the behavior of increased adsorption with increased concentration is also seen when injecting other EOR chemicals such as surfactants and polymers. The NP adsorption was also reduced on average in core samples injected with nanofluid and HCl at regular flow rate (q = 2 ml/min) and in room temperature, as seen in Figures 6.17, 6.22 and 6.25. Since reduction of adsorption did not always lead to reduced formation damage in these experiments, it is suggested that the acid may have reduced pore blockage caused by particle aggregation, but perhaps not the pore blockage caused by excessive adsorption (multi-layer) inside the pores.

The adsorption data was in many cases inconsistent with the recorded differential pressures, which was believed to be caused by the high sensitivity for contaminants in the UV-Vis apparatus. For an accurate adsorption measurement, the UV-Vis required the reference fluid to have the exact same composition as the sample fluid, except for the presence of NPs, in order to yield a realistic measurement. This was not an easy task since the effluent became altered/contaminated during transportation through the core, and the SSW effluent used as reference did not always have the same mineral composition.

It was also suggested that the nanoparticles in the suspension could scatter light when measured by the UV-Vis, which would cause the measurements to be inaccurate. This theory agrees with the different appearance of the light absorbency curves for tracer and NP effluent, as seen in Figures A.3 and A.4 respectively. However, there was no distortion

when the light absorbency of NPs in uncontaminated/clean SSW was measured as seen in Figure A.2. This suggests that contamination was the main cause of anomalous measurement data. Since nanofluids are colloidal suspensions and not solutions, it was suggested that the errors in the measurements could be caused by light scattering from the particles. However, the measurements in Figure A.2 suggest that contamination was the main issue.

8 Conclusion

The interest for nanotechnology has grown over the last decade, and its industrial implementations are believed to occur more frequently in the near future. The application of nanoparticles in the petroleum industry has proved to be beneficial, as they can facilitate and improve exploration, drilling and production processes. Silica nanoparticles hold a special promise for future EOR applications, but it requires high stability at sub-surface conditions.

The laboratory experiments have shown that silica nanoparticles are unstable in saltwater with divalent ions, and that the suspension stability may be enhanced by adding small amounts of HCl. Propagation of untreated nanoparticles in intermediate wet sandstone cause formation damage and almost make the rock impermeable after 4 PVs of injection. The permeability impairment is lessened when HCl is added to the nanofluid, but the effect of adding 0.001 wt% (10 ppm) of HCl is too small for a technically feasible field scale implementation of this nanofluid formulation. An increase of temperature to 70^{o}C and/or decrease of injection rate to q = 1 ml/min makes the formation damage worse than at initial conditions. Thus, further investigation is needed on the stability of silica nanofluids at sub-surface conditions. Based on the stability improvements seen in the nanofluids by adding HCl, the effect of using a higher concentration should be investigated. Ortega et al. (2016) used a HCl concentration of 230 ppm to stabilize their 0.05 wt% silica nanofluids at sub-surface conditions.

The adsorption of silica nanoparticles was high and actually excessive in intermediate wet sandstone. The nanoparticles did in many cases adsorb in multi-layers, which was in accordance with the large differential pressures recorded over the core samples. The nanoparticle retention may be significantly reduced if stability is achieved, since the repulsion between the propagating and the surface adhered nanoparticles will be increased.

9 Recommendation

An extensive investigation of nanosilica propagation in intermediate wet sandstone has been made in this master's thesis. The laboratory experiments have addressed the effects of varying the formation's permeability and temperature, as well as varying the NP concentration of the nanofluid. The use of a nanofluid stabilizer (HCl) to reduce adsorption and pore blockage was also demonstrated.

More research in general should be done on nanofluid stability at sub-surface conditions, as this is a key challenge for field scale applications. An increase of the acid concentration and using different acids should be further investigated, since the effect of using 10 ppm HCl was evident but only lead to small stability improvements. The use of polymer coating for steric stabilization should also be further studied, as this technique could provide stability of nanosilica in harsh reservoir environments (Ranka et al., 2015). However, the cost of this stabilization method must be considered since it is an important limiting factor of economically feasible EOR projects.

In future experiments, the wettability of the core samples should be re-evaluated after the nanofluids have been injected. Previous studies have shown that nanosilica injection leads to rock wettability alteration (Li and Torsaeter, 2015; El-Diasty, 2015), but it is not certain whether these properties sustain after HCl has been dispersed in the suspensions. Furthermore, the adsorption of nanoparticles should be compared in intermediate wet sandstone aged with oil and with SurfaSil, to ensure that there are no unexpected physicochemical interactions between the SurfaSil layer and the silica nanoparticles.

References

[1] Abdelfatah, Elsayed, Pournik, Maysam, Shiau, Bor Jier Ben, et al. 2017. Mathematical Modeling and Simulation of Formation Damage Associated with Nanoparticles Transport in Porous Media. Presented at the SPE Latin America and Caribbean Mature Fields Symposium. Salvador, Bahia, Brazil, 15–16 March. SPE-184894-MS. DOI: https://doi.org/10.2118/184894-MS.

[2] Afrapoli, M. Shabani, Crescente, C., Alipour, S., et al. 2009. The effect of bacterial solution on the wettability index and residual oil saturation in sandstone. *Journal of Petroleum Science and Engineering* **69** (3): 255-260. ISSN: 0920-4105. DOI: http://dx.doi.org/10.1016/j.petrol.2009.09.002.

[3] Agrawal, D. K., Kuznetsov, O. V., Suresh, R., et al. 2016. Environment-Friendly Colloidal Nanoparticles for Stabilizing Clays Within Subterranean Formations. Presented at the SPE Annual Technical Conference and Exhibition. Dubai, UAE, 26–28 September. SPE-181641-MS. DOI: https://doi.org/10.2118/181641-MS.

[4] Amanullah, Md, AlArfaj, Mohammed K., and Al-abdullatif, Ziad Abdullrahman. 2011. Preliminary Test Results of Nano-based Drilling Fluids for Oil and Gas Field Application. Presented at the SPE/IADC Drilling Conference and Exhibition. Amsterdam, The Netherlands, 1–3 March. SPE-139534-MS. DOI: https://doi.org/10.2118/139534-MS.

[5] Austad, Tor. 2013. Water-Based EOR in Carbonates and Sandstones: New Chemical Understanding of the EOR Potential Using "Smart Water" - Sheng, James J. *Enhanced Oil Recovery Field Case Studies*. Boston: Gulf Professional Publishing, pp. 301–335. ISBN: 978-0-12-386545-8. DOI: https://doi.org/10.1016/B978-0-12-386545-8.00013-0.

[6] Bazazi, Parisa, Gates, Ian D., Sanati Nezhad, Amir, et al. 2017. Silica-Based Nanofluid Heavy Oil Recovery A Microfluidic Approach. Presented at the SPE Canada Heavy Oil Technical Conference. Calgary, Alberta, Canada, 15–16 February. SPE-185008-MS. DOI: https://doi.org/10.2118/185008-MS.

[7] Bennetzen, Martin Vad and Mogensen, Kristian. 2014. Novel Applications of Nanoparticles for Future Enhanced Oil Recovery. Presented at the International Petroleum Technology Conference. Kuala Lumpur, Malaysia, 10–12 December. IPTC-17857-MS. DOI: https://doi.org/10.2523/IPTC-17857-MS.

[8] Brydson, Rik M. and Hammond, Chris. 2005. Generic Methodologies for Nanotechnology: Classification and Fabrication. *Nanoscale Science and Technology*. Chichester, UK: John Wiley Sons, Ltd, pp. 1–55. ISBN: 9780470020876. DOI: http://dx.doi.org/10.1002/0470020873.ch1.

[9] Chang, Harry L., Sui, Xingguang, Xiao, Long, et al. 2004. Successful Field Pilot of In-Depth Colloidal Dispersion Gel (CDG) Technology in Daqing Oil Field. Presented at the SPE/DOE Symposium on Improved Oil Recovery. Tulsa, Oklahoma, 17–21 April. SPE-89460-MS. DOI: https://doi.org/10.2118/89460-MS.

[10] Contreras, Oscar, Hareland, Geir, Husein, Maen, et al. 2014. Experimental Investigation on Wellbore Strengthening In Shales by Means of Nanoparticle-Based Drilling Fluids. Presented at the SPE Annual Technical Conference and Exhibition. Amsterdam, The Netherlands, 27–29 October. SPE-170589-MS. DOI: https://doi.org/10.2118/170589-MS.

[11] Cosentino, Luca. 2001. Basic Reservoir Engineering. *Integrated Reservoir Studies*. Paris: Editions Technip, p. 212. ISBN: 978-27108-0797-1.

[12] Dake, L. P. 1998. Fundamentals of Reservoir Engineering. seventeenth impression. Amsterdam: Elsevier. ISBN: 0-444-41830-X.

[13] Damsleth, Eivind and Holden, Lars. 1994. Mixed Reservoir Characterization Methods. Presented at the University of Tulsa Centennial Petroleum Engineering Symposium. Tulsa, Oklahoma, 29–31 August. SPE-27969-MS. DOI: https://doi.org/10.2118/27969-MS.

[14] El-Diasty, Abdelrahman Ibrahim. 2015. The Potential of Nanoparticles to Improve Oil Recovery in Bahariya Formation, Egypt: An Experimental Study. Presented at

the SPE Asia Pacific Enhanced Oil Recovery Conference. Kuala Lumpur, Malaysia, 11–13 August. SPE-174599-MS. DOI: https://doi.org/10.2118/174599-MS.

[15] Donaldson, Erle C. and Alam, Waqi. 2008. *Wettability*. Houston, Texas: Gulf Publishing Company. ISBN: 978-1-933762-29-6.

[16] Evonik. 2015. AEROSIL Fumed Silica: Technical Overview.

[17] Folttmann, H. and Quadir, A. 2008. Polyvinylpyrrolidone (PVP) - One of the Most Widely Used Excipients in Pharmaceuticals: An Overview. *Drug Delivery Technology* **8** (6): 22-27.

[18] Friedheim, James E., Young, Steven, De Stefano, Guido, et al. 2012. Nanotechnology for Oilfield Applications - Hype or Reality? Presented at the SPE International Oilfield Nanotechnology Conference and Exhibition. Noordwijk, The Netherlands, 12–14 June. SPE-157032-MS. DOI: https://doi.org/10.2118/157032-MS.

[19] Gao, C. 2007. Factors Affecting Particle Retention in Porous Media. *Emirates Journal for Engineering Research* **12** (3): 1-7.

[20] Ghadimi, A., Saidur, R., and Metselaar, H. S. C. 2011. A review of nanofluid stability properties and characterization in stationary conditions. *International Journal of Heat and Mass Transfer* **54** (17): 4051-4068. ISSN: 0017-9310. DOI: http://dx.doi.org/10.1016/j.ijheatmasstransfer.2011.04.014.

[21] Gilliland, H. E. and Conley, F. R. 1975. PD 14(2) Surfactant Waterflooding. Presented at the 9th World Petroleum Congress. Tokyo, Japan, 11–16 May. WPC-16327.

[22] Habibi, Youssef, Lucia, Lucian A., and Rojas, Orlando J. 2010. Cellulose Nanocrystals: Chemistry, Self-Assembly, and Applications. *Chemical Reviews* **110** (6): 3479-3500. ISSN: 0009-2665. DOI: http://dx.doi.org/10.1021/cr900339w.

[23] Hansen, E. L., Hemmen, H., Fonseca, D. M., et al. 2012. Swelling transition of a clay induced by heating. **2** 618. DOI: http://dx.doi.org/10.1038/srep00618.

[24] Healy, Robert N. and Reed, Ronald L. 1974. Physicochemical Aspects of Microemulsion Flooding. *SPE Journal* **14** (05): 491 - 501. SPE-4583-PA. DOI: http://dx.doi.org/10.2118/4583-PA.

[25] Hendraningrat, Luky, Engeset, Bjørnar, Suwarno, Suwarno, et al. 2012. Improved Oil Recovery by Nanofluids Flooding: An Experimental Study. Presented at the SPE Kuwait International Petroleum Conference and Exhibition. Kuwait City, Kuwait, 10–12 December. SPE-163335-MS. DOI: https://doi.org/10.2118/163335-MS.

[26] Hendraningrat, Luky, Engeset, Bjørnar, Suwarno, Suwarno, et al. 2013a. Laboratory investigation of porosity and permeability impairment in Berea sandstones due to hydrophilic nanoparticle retention. Presented at the

[27] Hendraningrat, Luky, Li, Shidong, and Torsaeter, Ole. 2013b. Enhancing Oil Recovery of Low-Permeability Berea Sandstone through Optimised Nanofluids Concentration. Presented at the SPE Enhanced Oil Recovery Conference. Kuala Lumpur, Malaysia, 2–4 July. SPE-165283-MS. DOI: https://doi.org/10.2118/165283-MS.

[28] Hendraningrat, Luky and Torsæter, O. 2014. Understanding Fluid-Fluid and Fluid-Rock Interactions in the Presence of Hydrophilic Nanoparticles at Various Conditions. Presented at the SPE Asia Pacific Oil Gas Conference and Exhibition. Adelaide, Australia, 14–16 October. SPE-171407-MS. DOI: https://doi.org/10.2118/171407-MS.

[29] Hirasaki, George, Miller, Clarence A., and Puerto, Maura. 2011. Recent Advances in Surfactant EOR. *SPE Journal* **16** (04): 889 - 907. SPE-115386-PA. DOI: http://dx.doi.org/10.2118/115386-PA.

[30] Horikoshi, Satoshi and Serpone, Nick. 2013. *Microwaves in Nanoparticle Synthesis*. First ed. Weinheim: Wiley-VCH Verlag GmbH Co. KGaA. DOI: http://dx.doi.org/10.1002/9783527648122.ch1.

[31] Hwang, Y., Lee, J. K., Lee, C. H., et al. 2007. Stability and thermal conductivity characteristics of nanofluids. *Thermochimica Acta* **455** (1): 70-74. ISSN: 0040-6031. DOI: http://dx.doi.org/10.1016/j.tca.2006.11.036.

[32] IEA and OECD. 2016. Key World Energy Statistics 2016. first edition. Paris: IEA/AIE.

[33] Jacobs, Trent. 2017. Industry and Academia Continue Working on Big Ideas for Nanotechnology. *Journal of Petroleum Technology* **69** (01): 34-38. SPE-0117-0034-JPT. DOI: https://doi.org/10.2118/0117-0034-JPT.

[34] Jacobs, Trent, Whitfield, Stephen, and Rassenfoss, Stephen. 2016. EP Notes (November 2016). *Journal of Petroleum Technology* **68** (11): 22 - 27. SPE-1116-0022-JPT. DOI: https://doi.org/10.2118/1116-0022-JPT.

[35] Jessen, F. W. and Mungan, Necmettin. 1959. The Effect of Particle Size Distribution and Exchange Cation on Gel Properties of Fractionated Bentonite Suspensions. Generic. SPE-1215-G.

[36] Johns, Russell T. and Dindoruk, Birol. 2013. Chapter 1 - Gas Flooding - Sheng, James J. *Enhanced Oil Recovery Field Case Studies*. Boston: Gulf Professional Publishing, pp. 1–22. ISBN: 978-0-12-386545-8. DOI: https://doi.org/10.1016/B978-0-12-386545-8.00001-4.

[37] Ju, Binshan, Dai, Shugao, Luan, Zhian, et al. 2002. A Study of Wettability and Permeability Change Caused by Adsorption of Nanometer Structured Polysilicon on the Surface of Porous Media. Presented at the SPE Asia Pacific Oil, Gas Conference, and Exhibition. Melbourne, Australia, 8–10 October. SPE-77938-MS. DOI: https://doi.org/10.2118/77938-MS.

[38] Kelsall, Robert W., Hamley, Ian W., and Geoghegan, Mark. 2005. Generic methodologies for nanotechnology: classification and fabrication. *Nanoscale science and technology*. Chichester, England; Hoboken, NJ: John Wiley, pp. 1–54. ISBN: 0470850868 9780470850862.

[39] Kestell, Aiden E. and DeLorey, Gabriel T. 2010. *Nanoparticles: Properties, Classification, Characterization, and Fabrication*. New York: Nova Science Publishers Inc. ISBN: 9781616683443 9781617618062.

[40] Kestin, Joseph, Khalifa, H. Ezzat, and Correia, Robert J. 1981. Tables of the dynamic and kinematic viscosity of aqueous NaCl solutions in the temperature range 20-150 C and the pressure range 0.1-35 MPa. *Journal of Physical and Chemical Reference Data* **10** (1): 71-88. DOI: https://doi.org/10.1063/1.555641.

[41] Kong, Xiangling and Ohadi, Michael. 2010. Applications of Micro and Nano Technologies in the Oil and Gas Industry - Overview of the Recent Progress. Presented

at the Abu Dhabi International Petroleum Exhibition and Conference. Abu Dhabi, UAE, 1–4 November. SPE-138241-MS. DOI: https://doi.org/10.2118/138241-MS.

[42] Kosynkin, Dmitry and Kanj, Mazen. 2011. Reservoir Nanoagents: Tools of In-Situ Sensing and Intervention. Presented at the 20th World Petroleum Congress. Doha, Qatar, 4–8 December. WPC-20-3338.

[43] Krishnamoorti, Ramanan. 2006. Extracting the Benefits of Nanotechnology for the Oil Industry. *Journal of Petroleum Technology* **58** (11): 24-26. SPE-1106-0024-JPT. DOI: http://dx.doi.org/10.2118/1106-0024-JPT.

[44] Lake, Larry W. 1989. *Enhanced Oil Recovery*. first edition. New Jersey: Prentice Hall. ISBN: 0-13-281601-6.

[45] Lau, Hon Chung, Yu, Meng, and Nguyen, Quoc P. 2016. Nanotechnology for Oilfield Applications: Challenges and Impact. Presented at the Abu Dhabi International Petroleum Exhibition Conference. Abu Dhabi, UAE, 7–10 November. SPE-183301-MS. DOI: http://dx.doi.org/10.2118/183301-MS.

[46] Lee, S. and Kam, S. I. 2013. Enhanced Oil Recovery by Using CO2 Foams: Fundamentals and Field Applications - Sheng, James J. *Enhanced Oil Recovery Field Case Studies*. Boston: Gulf Professional Publishing, pp. 23–61. ISBN: 978-0-12-386545-8. DOI: https://doi.org/10.1016/B978-0-12-386545-8.00002-6.

[47] Li, Robert Feng, Le Bleu, Robin B., Liu, Shunhua, et al. 2008. Foam Mobility Control for Surfactant EOR. Presented at the SPE Symposium on Improved Oil Recovery. Tulsa, Oklahoma, USA, 20–23 April. SPE-113910-MS. DOI: http://dx.doi.org/10.2118/113910-MS.

[48] Li, Shidong. 2015. An Experimental Investigation of Enhanced Oil Recovery Mechanisms in Nanofluid Injection Process. PhD dissertation. Norwegian University of Science and Technology (NTNU), Trondheim, Norway.

[49] Li, Shidong, Hendraningrat, Luky, and Torsaeter, Ole. 2013. Improved Oil Recovery by Hydrophilic Silica Nanoparticles Suspension: 2-Phase Flow Experimental Studies. Presented at the International Petroleum Technology Conference. Beijing, China, 26–28 March. IPTC-16707-MS. DOI: https://doi.org/10.2523/IPTC-16707-MS.

[50] Li, Shidong and Torsaeter, Ole. 2015. The Impact of Nanoparticles Adsorption and Transport on Wettability Alteration of Intermediate Wet Berea Sandstone. Presented at the SPE Middle East Unconventional Resources Conference and Exhibition. Muscat, Oman, 26–28 January. SPE-172943-MS. DOI: https://doi.org/10.2118/172943-MS.

[51] Liu, Xinghui and Civan, Faruk. 1993. Characterization and Prediction of Formation Damage in Two-Phase Flow Systems. Presented at the SPE Production Operations Symposium. Oklahoma City, Oklahoma, 21–23 March. SPE-25429-MS. DOI: https://doi.org/10.2118/25429-MS.

[52] McElfresh, Paul M., Holcomb, David Lee, and Ector, Daniel. 2012. Application of Nanofluid Technology to Improve Recovery in Oil and Gas Wells. Presented at the SPE International Oilfield Nanotechnology Conference and Exhibition. Noordwijk, The Netherlands, 12–14 June. SPE-154827-MS. DOI: https://doi.org/10.2118/154827-MS.

[53] Meehan, Nathan. 2011. Baker Hughes Reservoir Blog. URL: http://blogs.bakerhughes.com/reservoir/2011/04/09/formation-testing-part-ii-of-iii/ (visited on June 2, 2017).

[54] Metin, Cigdem O., Lake, Larry W., Miranda, Caetano R., et al. 2011. Stability of aqueous silica nanoparticle dispersions. *Journal of Nanoparticle Research* **13** (2): 839-850. ISSN: 1572-896X. DOI: http://dx.doi.org/10.1007/s11051-010-0085-1.

[55] Nanoscience Instruments. 2017. Scanning Electron Microscopy. Web Page. URL: http://www.nanoscience.com/technology/sem-technology/.

[56] Nikolov, Alex, Kondiparty, Kirti, and Wasan, Darsh. 2010. Nanoparticle Self-Structuring in a Nanofluid Film Spreading on a Solid Surface. *Langmuir* **26** (11): 7665-7670. ISSN: 0743-7463. DOI: http://dx.doi.org/10.1021/la100928t.

[57] Ogolo, N. A., Olafuyi, O. A., and Onyekonwu, M. O. 2012. Enhanced Oil Recovery Using Nanoparticles. Presented at the SPE Saudi Arabia Section Technical Symposium and Exhibition. Al-Khobar, Saudi Arabia, 8–11 April. SPE-160847-MS. DOI: http://dx.doi.org/10.2118/160847-MS.

[58] Ortega, Daniel J. Sivira, Kim, Han Byal, James, Lesley A., et al. 2016. The Effectiveness of Silicon Dioxide SiO2 Nanoparticle as an Enhanced Oil Recovery Agent

in Ben Nevis Formation, Hebron Field, Offshore Eastern Canada. Presented at the Abu Dhabi International Petroleum Exhibition Conference. Abu Dhabi, UAE, 7–10 November. SPE-183546-MS. URL: https://doi.org/10.2118/183546-MS.

[59] Patel, Akshit, Nihalani, Dipesh, Mankad, Dhaivat, et al. 2017. Evaluating Feasibility of Hydrophilic Silica Nanoparticles for In-Situ Emulsion Formation in Presence of Co-Surfactant: An Experimental Study. Presented at the SPE Kingdom of Saudi Arabia Annual Technical Symposium and Exhibition. Dammam, Saudi Arabia, 24–27 April. SPE-188141-MS. DOI: https://doi.org/10.2118/188141-MS.

[60] Pearce, J. C. and Megginson, E. A. 1991. Current Status Of The Duri Steamflood Project Sumatra, Indonesia. Presented at the SPE International Thermal Operations Symposium. Bakersfield, California, 7–8 February. SPE-21527-MS. DOI: https://doi.org/10.2118/21527-MS.

[61] Petosa, Adamo R., Jaisi, Deb P., Quevedo, Ivan R., et al. 2010. Aggregation and Deposition of Engineered Nanomaterials in Aquatic Environments: Role of Physicochemical Interactions. *Environmental Science & Technology* **44** (17): 6532-6549. DOI: http://dx.doi.org/10.1021/es100598h.

[62] Pitkethly, Michael J. 2004. Nanomaterials: the driving force. *Materials Today* **7** (12): 20-29. DOI: http://dx.doi.org/10.1016/S1369-7021(04)00627-3.

[63] Rahmani, Amir Reza, Bryant, Steven, Huh, Chun, et al. 2015. Crosswell Magnetic Sensing of Superparamagnetic Nanoparticles for Subsurface Applications. *SPE Journal* **20** (05): 1067-1082. SPE-166140-PA. DOI: https://doi.org/10.2118/166140-PA.

[64] Ramsden, Jeremy J. 2011. Nanomaterials and their production. 1st edition. Oxford: William Andrew Publishing, pp. 103–104. ISBN: 978-0-08-096447-8. DOI: http://dx.doi.org/10.1016/B978-0-08-096447-8.00012-0.

[65] Ranka, Mikhil, Brown, Paul, and Hatton, T. Alan. 2015. Responsive Stabilization of Nanoparticles for Extreme Salinity and High-Temperature Reservoir Applications. *ACS Applied Materials Interfaces* **7** (35): 19651-19658. ISSN: 1944-8244. DOI: http://dx.doi.org/10.1021/acsami.5b04200.

[66] Sastry, Murali. 2003. Phase transfer protocols in nanoparticle synthesis. *Current Science* **85** (12): 1735-1745. ISSN: 00113891.

[67] Savins, J. G. 1969. Non-Newtonian Flow Through Porous Media. *Industrial Engineering Chemistry* **61** (10): 18-47. ISSN: 0019-7866. DOI: http://dx.doi.org/10.1021/ie50718a005.

[68] SCCP. 2007. *Safety of Nanomaterials in Cosmetic Products*. Brussels: Health and Consumer Directorate-General.

[69] Schlumberger. 1998a. Schlumberger Oilfield Glossary: Bentonite. URL: http://www.glossary.oilfield.slb.com/Terms/b/bentonite.aspx (visited on March 15, 2017).

[70] Schlumberger. 1998b. Schlumberger Oilfield Glossary: Permeability. URL: http://www.glossary.oilfield.slb.com/Terms/p/permeability.aspx (visited on March 21, 2017).

[71] Schlumberger. 1998c. Schlumberger Oilfield Glossary: Primary Recovery. URL: http://www.glossary.oilfield.slb.com/Terms/p/primary_recovery.aspx (visited on April 18, 2017).

[72] Schlumberger. 1998d. Schlumberger Oilfield Glossary: Secondary Recovery. URL: http://www.glossary.oilfield.slb.com/Terms/p/secondary_recovery.aspx (visited on November 11, 2016).

[73] Shaw, Ryan. 2016. Achieving Reliable Nanoparticle Sizing. *Dynamic Light Scattering Training*. Australia: ATA Scientific. URL: www.atascientific.com.au.

[74] Shen, Chonghui. 2013. SAGD for Heavy Oil Recovery - Sheng, James J. *Enhanced Oil Recovery Field Case Studies*. Boston: Gulf Professional Publishing, pp. 413–445. ISBN: 978-0-12-386545-8. DOI: https://doi.org/10.1016/B978-0-12-386545-8.00017-8.

[75] Sheng, James J. 2011. *Modern Chemical Enhanced Oil Recovery - Theory and Practice*. first edition. Burlington, MA: Elsevier. ISBN: 978-1-85617-745-0.

[76] Sheng, James J. 2013a. ASP Fundamentals and Field Cases Outside China. *Enhanced Oil Recovery Field Case Studies*. Boston: Gulf Professional Publishing, pp. 189–201. ISBN: 978-0-12-386545-8. DOI: https://doi.org/10.1016/B978-0-12-386545-8.00009-9.

[77] Sheng, James J. 2013b. Steam Flooding. *Enhanced Oil Recovery Field Case Studies*. Boston: Gulf Professional Publishing, pp. 361–388. ISBN: 978-0-12-386545-8. DOI: https://doi.org/10.1016/B978-0-12-386545-8.00015-4.

[78] Skauge, Tormod, Spildo, Kristine, and Skauge, Arne. 2010. Nano-sized Particles For EOR. Presented at the SPE Improved Oil Recovery Symposium. Tulsa, Oklahoma, 24–28 April. SPE-129933-MS. DOI: https://doi.org/10.2118/129933-MS.

[79] Srivastava, Mayank, Zhang, Jieyuan, Nguyen, Quoc Phuc, et al. 2009. A Systematic Study of Alkali Surfactant Gas Injection as an Enhanced Oil Recovery Technique. Presented at the SPE Annual Technical Conference and Exhibition. New Orleans, Louisiana, 4–7 October. SPE-124752-MS. DOI: http://dx.doi.org/10.2118/124752-MS.

[80] Taber, J. J. 1990. Environmental Improvements and Better Economics in EOR Operations. *In Situ* **14** (4): 345.

[81] The Royal Society & The Royal Academy of Engineering. 2004. *Nanoscience and nanotechnologies: opportunities and uncertainties*. London: The Royal Society.

[82] Torres-Verdin, Carlos and Tarek, M. Habashy. 1993. An Approach to Nonlinear Inversion With Applications to Cross-Well EM Tomography. Presented at the 1993 SEG Annual Meeting. Washington, DC, 26–30 September. SEG-1993-0351.

[83] Torsæter, O and Abtahi, M. 2003. *Experimental reservoir engineering laboratory workbook*. Second edition. Trondheim: Department of Petroleum Engineering and Applied Geophysics, NTNU.

[84] Turta, Alex. 2013. In Situ Combustion - Sheng, James J. *Enhanced Oil Recovery Field Case Studies*. Boston: Gulf Professional Publishing, pp. 447–541. ISBN: 978-0-12-386545-8. DOI: https://doi.org/10.1016/B978-0-12-386545-8.00018-X.

[85] U.S. National Nanotechnology Initiative. 2010. What's So Special about the Nanoscale? URL: http://www.nano.gov/nanotech-101/special (visited on June 7, 2017).

[86] Wasan, Darsh, Nikolov, Alex, and Kondiparty, Kirti. 2011. The wetting and spreading of nanofluids on solids: Role of the structural disjoining pressure. *Current Opin-*

ion in Colloid Interface Science **16** (4): 344-349. ISSN: 1359-0294. DOI: http://dx.doi.org/10.1016/j.cocis.2011.02.001.

[87] White, Frank M. 1991. Viscous fluid flow. Second edition. McGraw-Hill series in mechanical engineering. New York: McGraw-Hill, p. 614.

[88] Wilt, Michael, Lee, Ki Ha, Becker, Alex, et al. 1996. Crosshole EM In Steel-cased Boreholes. Presented at the 1996 SEG Annual Meeting. Denver, Colorado, 10–15 November. SEG-1996-0230.

[89] Xu, Feng, Guo, Xiao, Wang, Wanbin, et al. 2011. Case Study: Numerical Simulation Of Surfactant Flooding In Low Permeability Oil Filed. Presented at the SPE Enhanced Oil Recovery Conference. Kuala Lumpur, Malaysia, 19–21 July. SPE-145036-MS. DOI: http://dx.doi.org/10.2118/145036-MS.

[90] Yu, Wei and Xie, Huaqing. 2012. A Review on Nanofluids: Preparation, Stability Mechanisms, and Applications. *Journal of Nanomaterials* **2012** 17. DOI: http://dx.doi.org/10.1155/2012/435873.

[91] Zhang, Tiantian, Murphy, Michael, Yu, Haiyang, et al. 2013. Investigation of Nanoparticle Adsorption During Transport in Porous Media. Presented at the SPE Annual Technical Conference and Exhibition. New Orleans, Louisiana, USA. SPE-166346-MS. DOI: https://doi.org/10.2118/166346-MS.

A Results and Calculations

A.1 Ageing of Core Samples

High Permeable Cores											
Dry State	**H1**	**H2**	**H3**	**H4**	**H5**	**H6**	**H7**	**H8**	**H9**	**T1**	**T2**
m [g]	233,72	234,64	233,62	234,29	232,67	234,67	233,04	232,8	234,29	234,12	233,81
Aged State	**H1**	**H2**	**H3**	**H4**	**H5**	**H6**	**H7**	**H8**	**H9**	**T1**	**T2**
m [g]	235,66	236,68	235,42	235,98	234,48	236,68	234,63	234,94	236,45	235,78	235,83
Δ m [g]	*1,94*	*2,04*	*1,8*	*1,69*	*1,81*	*2,01*	*1,59*	*2,14*	*2,16*	*1,66*	*2,02*
Low Permeable Cores											
Dry State	**L1**	**L2**	**L3**	**L4**	**L5**	**L6**	**L7**	**L8**	**L9**		
m [g]	240,55	236,9	238,25	240,3	239,28	234,78	236,86	241,28	235,78		
Aged State	**L1**	**L2**	**L3**	**L4**	**L5**	**L6**	**L7**	**L8**	**L9**		
m [g]	241,72	238,09	239,43	241,36	240,54	236,12	237,97	242,43	236,82		
Δ m [g]	*1,17*	*1,19*	*1,18*	*1,06*	*1,26*	*1,34*	*1,11*	*1,15*	*1,04*		

Table A.1: Core data before/after ageing

A.2 Porosity Data

High Permeable Cores									
Dry State	**H1**	**H2**	**H3**	**H4**	**H5**	**H6**	**H7**	**H8**	**H9**
m [g]	233,72	234,64	233,62	234,29	232,67	234,67	233,04	232,8	234,29
Saturated State	**H1**	**H2**	**H3**	**H4**	**H5**	**H6**	**H7**	**H8**	**H9**
m [g]	258,67	259,63	258,97	259,64	258	259,77	258,81	258,29	252,29
Δ m [g]	*24,95*	*24,99*	*25,35*	*25,35*	*25,33*	*25,1*	*25,77*	*25,49*	*18*
PV [ml]	*24,33*	*24,37*	*24,72*	*24,72*	*24,70*	*24,48*	*25,13*	*24,86*	*17,55*
Core Dimensions	**H1**	**H2**	**H3**	**H4**	**H5**	**H6**	**H7**	**H8**	**H9**
L [mm]	99,64	99,64	99,64	99,64	99,64	99,64	99,64	99,64	99,64
D [mm]	38,1	38,1	38,1	38,1	38,1	38,1	38,1	38,1	38,1
A [cm^2]	11,40	11,40	11,40	11,40	11,40	11,40	11,40	11,40	11,40
V(bulk) [ml]	*114*	*114*	*114*	*114*	*114*	*114*	*114*	*114*	*114*
ϕ	21,4%	21,5%	21,8%	21,8%	21,7%	21,5%	22,1%	21,9%	15,5%
Low Permeable Cores									
Dry State	**L1**	**L2**	**L3**	**L4**	**L5**	**L6**	**L7**	**L8**	**L9**
m [g]	240,55	236,9	238,25	240,3	239,28	234,78	236,86	241,28	235,78
Saturated State	**L1**	**L2**	**L3**	**L4**	**L5**	**L6**	**L7**	**L8**	**L9**
m [g]	262,52	259,25	260,41	262,3	261,7	257,05	258,58	262,79	258,05
Δ m [g]	*21,97*	*22,35*	*22,16*	*22*	*22,42*	*22,27*	*21,72*	*21,51*	*22,27*
PV [ml]	21,42	21,79	21,61	21,45	21,86	21,72	21,18	20,98	21,72
Core Dimensions	**L1**	**L2**	**L3**	**L4**	**L5**	**L6**	**L7**	**L8**	**L9**
L [mm]	99,64	99,64	99,64	99,64	99,64	99,64	99,64	99,64	99,64
D [mm]	38,1	38,1	38,1	38,1	38,1	38,1	38,1	38,1	38,1
A [cm^2]	11,4	11,4	11,4	11,4	11,4	11,4	11,4	11,4	11,4
V(bulk) [ml]	114	114	114	114	114	114	114	114	114
ϕ	18,9%	19,2%	19,0%	18,9%	19,2%	19,1%	18,6%	18,5%	19,1%
ρ(brine) [g/ml]	1,02549								

Table A.2: Core data and porosity calculations

A.3 Permeability Data

High Permeable Cores						
	H1	**H2**	**H3**	**H4**	**H5**	**H6**
ΔP [bar]	0,08	0,135	0,13	0,13	0,13	0,06
q [ml/min]	2,00	3,00	3,00	3,00	3,00	1,00
k(abs) [mD]	364	324	336	336	336	243
Low Permeable Cores						
	L1	**L2**	**L3**	**L4**	**L5**	**L6**
ΔP [bar]	0,37	0,16	0,27	0,21	0,30	0,09
q [ml/min]	3,00	2,00	3,00	2,00	3,00	1,00
k(abs) [mD]	118	182	162	139	146	162

Constants	
μ(SSW) [cP]	1
L [mm]	99,64
A [cm^2]	11,4009

Table A.3: Permeability calculations

A.4 Nanofluid properties

				Nanoparticle Concentration			
		Concentration		0,05%	0,10%	0,15%	0,20%
A300	No Acid	x	pH	5,0	5,0	5,0	5,0
A300	HCl	0,001%	pH	4,0	4,0	4,0	4,0
A300	HCl	0,010%	pH	4,0	3,0	2,0	2,0
A300	HCl	0,050%	pH	1,5	1,5	1,5	1,0
A300	HCl	0,100%	pH	1,0	1,0	1,0	1,0
A300	HCl	0,500%	pH	0,5	0,5	0,5	0,5
A300	CH3COOH	0,005%	pH	4,5	3,5	4,5	4,5
A300	CH3COOH	0,010%	pH	4,0	3,5	3,5	3,0
A300	CH3COOH	0,050%	pH	3,0	3,0	3,0	2,5
A300	CH3COOH	0,100%	pH	2,5	2,5	2,0	2,0
A300	CH3COOH	0,500%	pH	1,0	1,0	0,5	0,5

Table A.4: Preliminary pH indications

				Nanoparticle Concentration			
		Measurement		0,05%	0,10%	0,15%	0,20%
NP	A300	pH	1	5,80	5,45	5,24	5,02
Stabilizer	None	pH	2	5,50	5,41	5,32	5,26
Concentration	0	pH	Avg	5,65	5,43	5,28	5,14
		Std.Dev	-	3%	0%	1%	2%
NP	A300	pH	1	4,01	4,13	4,06	3,99
Stabilizer	HCl	pH	2	3,71	3,56	3,54	3,51
Concentration	0,001%	pH	Avg	3,86	3,85	3,80	3,75
		Std.Dev	-	4%	7%	7%	6%
NP	A300	pH	1	3,95	4,01	3,99	3,97
Stabilizer	CH3COOH	pH	2	3,74	3,64	3,60	3,55
Concentration	0,005%	pH	Avg	3,85	3,83	3,80	3,76
		Std.Dev	-	3%	5%	5%	6%

Table A.5: pH values from pH meter

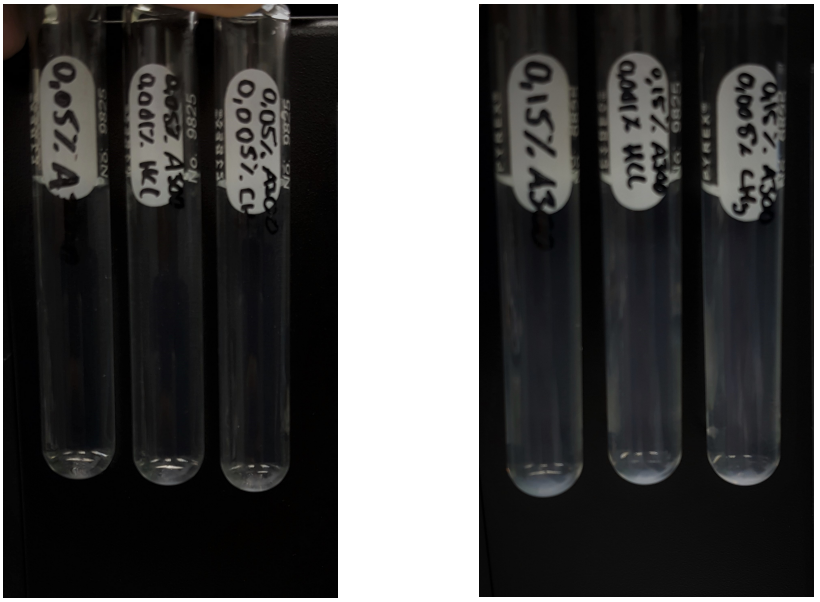

(a) 0.05 wt% NP concentration **(b)** 0.15 wt% NP concentration

Figure A.1: Stability analysis of A300, A300+HCl, A300+CH3COOH

A.5 Core Flooding Data

Concentration NaI [ppm]	Light Absorbency [AU]
5	0,455
10	0,9
15	1,349
20	1,751
25	2,373
30	2,69

Table A.6: Absorbance of various Tracer solution concentrations

NP Concentration [wt%]	Wavelength [nm]	Light Absorbency [AU]
0,025	210	0,164
0,05	210	0,311
0,075	210	0,435
0,1	210	0,549
0,125	210	0,672
0,15	210	0,797
0,175	208	0,914
0,2	208	1,051

Table A.7: Absorbance of various NP suspension concentrations

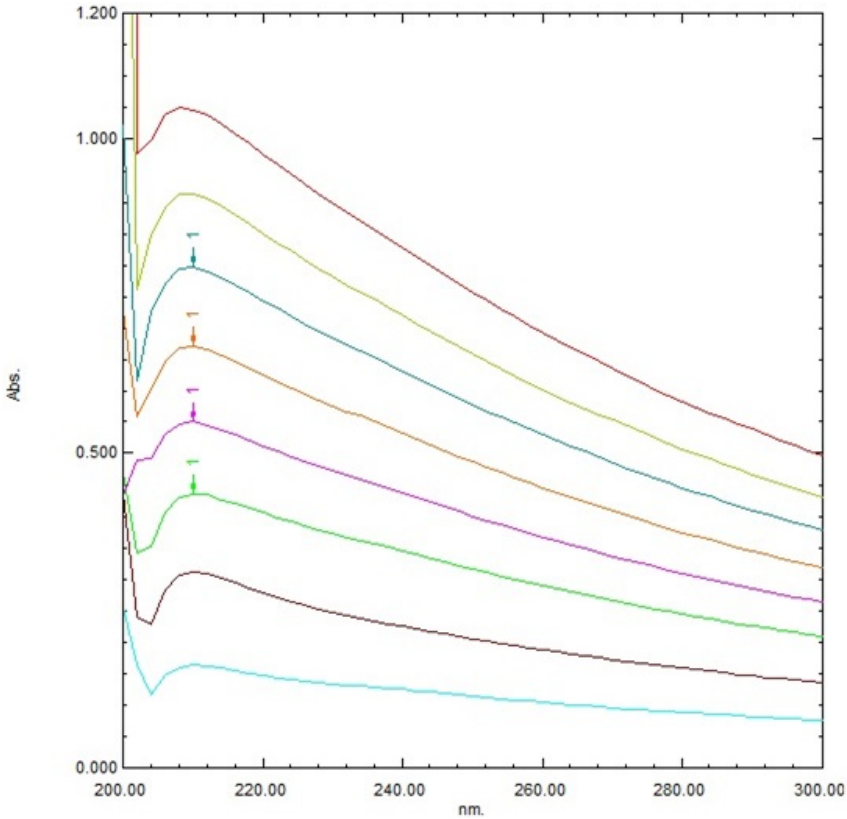

Figure A.2: NP absorbency in "clean" SSW

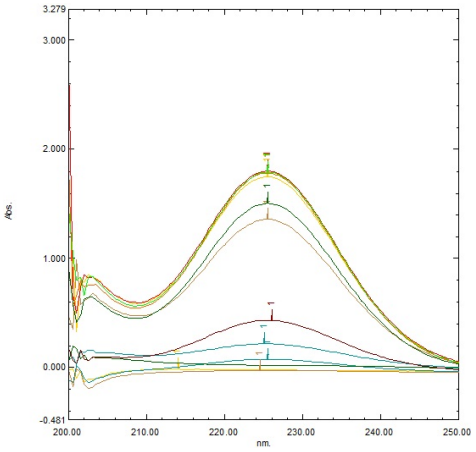

(a) Absorbency of tracer effluent in H1 (y-axis is scaled differently)

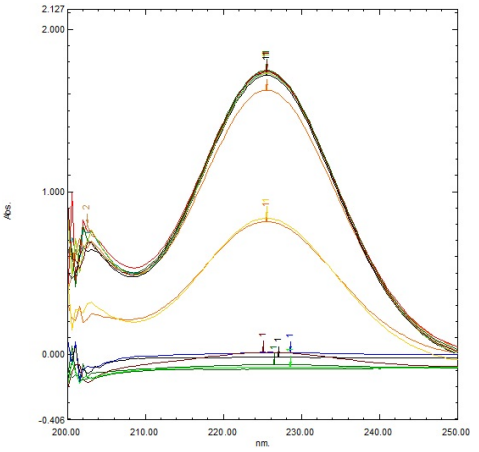

(b) Absorbency of tracer effluent in L1

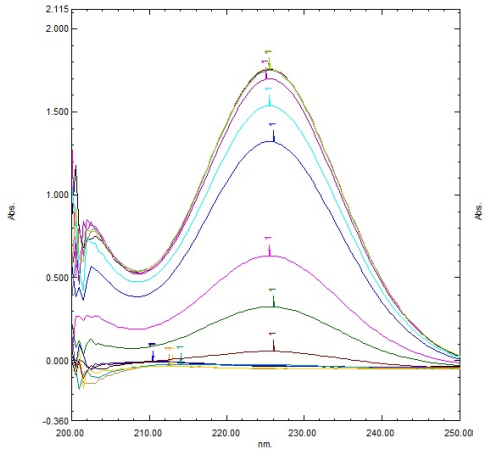

(c) Absorbency of tracer effluent in H2

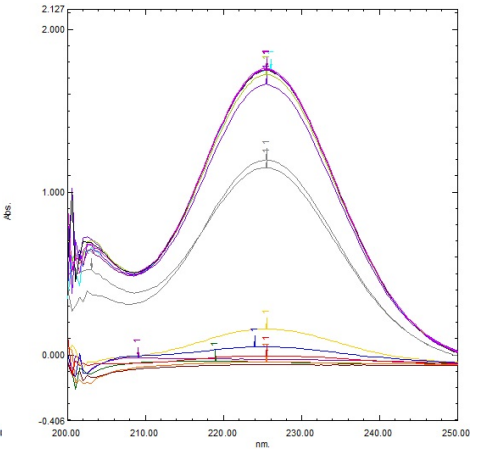

(d) Absorbency of tracer effluent in L2

Figure A.3: Light absorbency of Tracer effluents

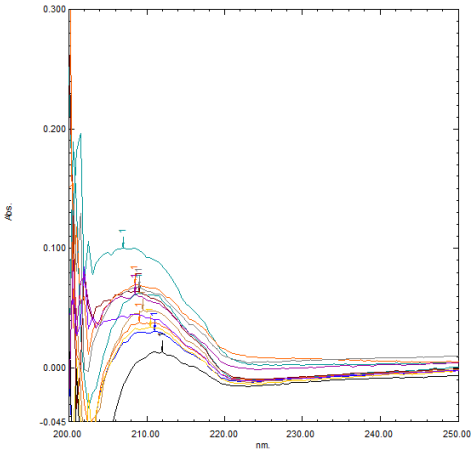

(a) Absorbency of NP effluent in H3

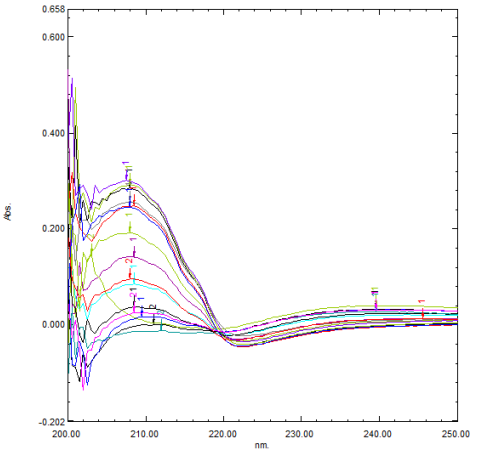

(b) Absorbency of NP effluent in L3

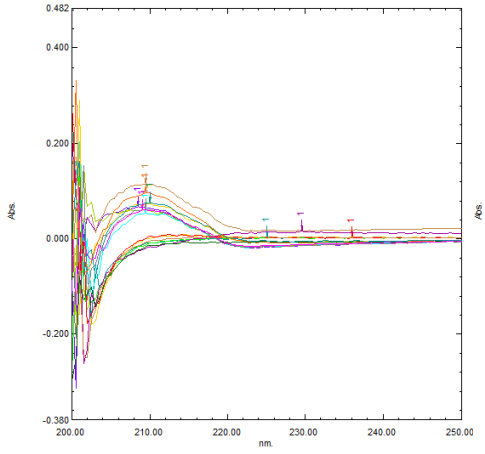

(c) Absorbency of NP effluent in H4

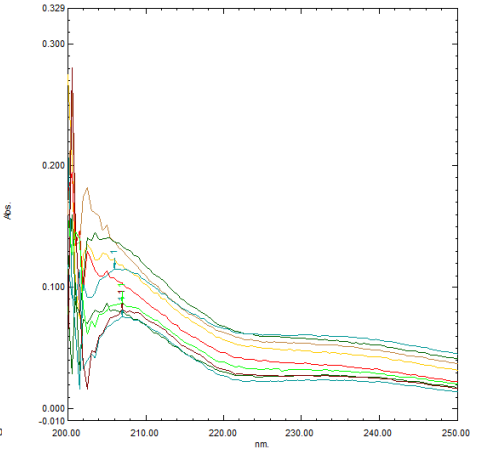

(d) Absorbency of NP effluent in L4

Figure A.4: Light absorbency of NP effluents

Nanofluid comp	Core	Vp	Nanofluid	q (SSW)	ΔP (Pre)	K0 (init. perm)	T	q (nanofluid)	ΔP (Post)	K (inst. perm)	k (reduced)	Core	Relative PI
		[ml]	wt%	[ml/min]	[bar]	[mD]	[°c]	[ml/min]	[bar]	[mD]	[mD]		[-]
A300	H1	24,3	0,05	2,00	0,08	364	25	2	4,2	6,94	-98,1%	H1/H1	-
A300	L1	21,4	0,05	3,00	0,37	118	25	2	5,0	5,83	-95,1%	L1/L1	-
A300	H2	24,4	0,15	3,00	0,14	324	25	2	7,5	3,88	-98,8%	H2/H2	-
A300	L2	21,8	0,15	2,00	0,16	182	25	2	11	2,72	-98,5%	L2/L2	-
A300 + HCl	H3	24,7	0,05	3,00	0,13	336	25	2	1,9	15,6	-95,4%	H3/H1	-3%
A300 + HCl	L3	21,6	0,05	2,00	0,17	171	25	2	5,7	5,11	-97,0%	L3/L1	2%
A300 + HCl	H4	24,7	0,15	3,00	0,13	336	25	2	10	2,83	-99,2%	H4/H2	0%
A300 + HCl	L4	21,5	0,15	2,00	0,21	139	25	2	8,7	3,35	-97,6%	L4/L2	-1%
A300 + HCl	H5	24,7	0,05	3,00	0,13	336	25	2	1,1	26,8	-92,0%	H5/H1	-6%
A300 + HCl	L5	21,9	0,05	3,00	0,3	146	25	2	1,8	15,9	-89,1%	L5/L1	-6%
A300 + HCl	H6	24,5	0,05	1,00	0,06	243	**70**	**1**	inf	0,0	-100,0%	H6/H1	2%
A300 + HCl	L6	21,7	0,05	1,00	0,09	162	25	**1**	3,4	4,3	-97,3%	L6/L1	2%

Table A.8: Instantaneous permeability and formation damage

B Laboratory equipment

B.1 Preparation of Cores and Fluids

Figure B.1: Digital densimeter

Figure B.2: Mettler Toledo SevenCompact pH meter

Figure B.3: SurfaSil saturation of core sample T1 and T2

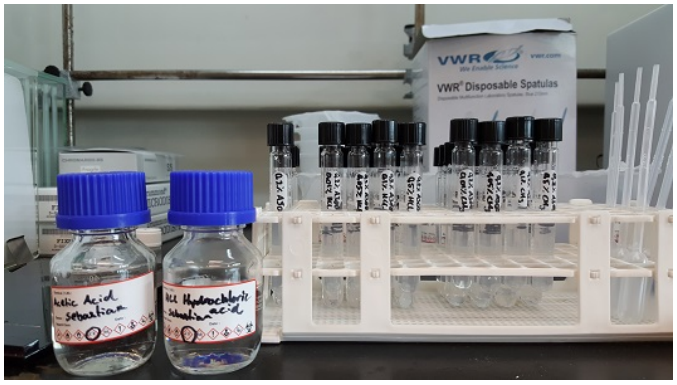

Figure B.4: Stability tests of various NP/acid concentrations

B.2 Core Flooding

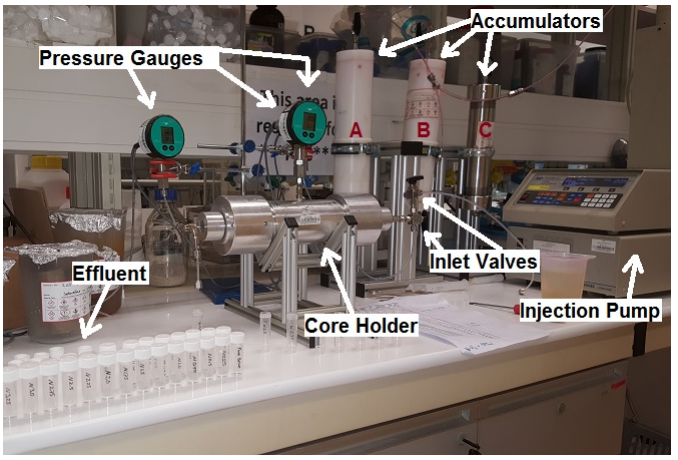

Figure B.5: Low temperature core flooding

Figure B.6: High temperature core flooding

Figure B.7: UV-Vis apparatus